Title
Bone Stress Whitening Is a Fundamental Molecular Mechanism of Collagen I

Author
Gloekler, Lauren

Publication Date
2022

Peer reviewed|Thesis/dissertation

Bone Stress Whitening Is a Fundamental Molecular Mechanism of Collagen I

By

LAUREN GLOEKLER
THESIS

Submitted in partial satisfaction of the requirements for the degree of

MASTER OF SCIENCE

in

Biomedical Engineering

in the

OFFICE OF GRADUATE STUDIES

of the

UNIVERSITY OF CALIFORNIA

DAVIS

Approved:

David P. Fyhrie, Chair

Randy P. Carney

Susan M. Stover

Committee in Charge

2022

Acknowledgements

This thesis is the culmination of support from three laboratories, of which I have the honor to be a member. Firstly, I would like to thank my major advisor, Dr. David Fyhrie, for his guidance throughout this project. Amid a global pandemic, his mentorship and encouragement proved vital to keeping up the project's momentum. I can greatly attribute my growth as a researcher to his mentorship. I would also like to sincerely thank my co-mentors, Dr. Randy Carney and Dr. Susan Stover, for their interest and enthusiasm in this project. Each have been unwaveringly generous with their time and expertise.

There are countless other lab members who deserve recognition. Sarah Shaffer helped me with all the statistics for this research project and created some of the figures in this thesis. Sarah is a great mentor and friend, and I am extremely grateful for all her help! Additionally, Tanya Garcia-Nolen and Justine Irvin each worked overtime to keep the lab running smoothly and offered me endless support. I also owe a great deal of thanks to my fellow graduate students who kept my spirits high with Dungeons and Dragons sessions and great food!

Further, I am extremely grateful for all my friends and family who supported me and helped make this research possible. My brother Ryan has inspired me to become a better researcher. I could not be prouder of him for accepting a position as a graduate student at UC Davis and keeping the Aggie tradition alive in our family! Moreover, my partner Matthew consistently exemplifies the value of hard work and resourcefulness. He motivated me when I needed inspiration. He has loved and supported me though the highs and lows of this research project, and for that I cannot thank him enough.

Finally, a tremendous thank you to my parents Susan and Toby, who empowered me to become an engineer. They are the reason I pushed myself to pursue a graduate degree, and the reason I was able to succeed in the challenge. I would not be the woman I am without their love and support. Thanks Mom and Dad; this one's for you!

Abstract

Bone tissue “stress-whitens” (changes from translucent to opaque) immediately prior to fracture, yet the underlying mechanisms governing this phenomenon are unclear. Bone is comprised of three major constituents: a mineral phase (mostly hydroxyapatite), an organic phase (mostly collagen type I), and water. Past research has demonstrated that stress-whitening is a property of the collagen component, rather than the mineral component of bone [1]. The hypothesis of the thesis is that stress-whitening is caused by a mechanically-driven change in the microstructure of the collagen component of bone. Label-free Raman microspectroscopy was used to measure changes in the chemical components of demineralized bone before and after tension. We demonstrate that mechanically caused stress-whitening in equine bone is associated with changes in the Raman spectrum. More specifically, the results of the Raman spectral data demonstrate that there is an effect of mechanical loading on the protein structure of bone, specifically as demonstrated by changes in the amide III (1280 cm^{-1}), CH_2 (1467 cm^{-1}) and amide I (1671 cm^{-1}) peak intensities. Interpreting these peak changes as related to collagen hydrogen bonding and bone toughness [2] is consistent with an increased crystallization of collagen under mechanical load, which Janet Clark hypothesized as a toughening mechanism of collagenous tissues [3]. The results of this research augment the understanding of the structural mechanisms of bone mechanics and have the potential to supplement the understanding of bone diseases associated with changes in molecular mechanics and disruption of intermolecular hydrogen bonding, such as osteogenesis imperfecta [4].

References

[1] M. R. Hardisty, T. C. Garcia, S. Choy, J. Dahmubed, S. M. Stover, and D. P. Fyhrie, "Stress-whitening occurs in demineralized bone," *Bone*, vol. 57, no. 2, pp. 367–374, Dec. 2013, doi: 10.1016/j.bone.2013.08.029.

[2] M. Unal, H. Jung, and O. Akkus, "Novel Raman Spectroscopic Biomarkers Indicate That Postyield Damage Denatures Bone's Collagen," *Journal of Bone and Mineral Research*, vol. 31, no. 5, pp. 1015–1025, May 2016, doi: 10.1002/jbmr.2768.

[3] Janet H. Clark, "Reversible Crystallization In Tendons and Its Functional Significance," 1926. doi: 10.1073/pnas.14.7.526.

[4] A. Gautieri, S. Vesentini, A. Redaelli, and M. J. Buehler, "Osteogenesis imperfecta mutations lead to local tropocollagen unfolding and disruption of H-bond network," *RSC Advances*, vol. 2, no. 9, pp. 3890–3896, Apr. 2012, doi: 10.1039/c2ra01047j.

Table of Contents

Chapter 1: Introduction

1.1 Background

The purpose of the human skeletal system is to support mechanical loading of the body over long periods of time. During cyclic loading, the effects of this stress accumulate and cause the formation of microcracks within the bone. Should the microcracks propagate, they can become larger macrocracks and eventually result in complete bone fracture. Microcracks are typically healed during bone remodeling, however fatigue failure may occur if the damage accumulates faster than the bone can remodel [1].

In the long term, crack growth in bone is largely controlled by tissue renewal (i.e., bone remodeling). However, in the shorter term, bone experiences many toughening mechanisms that slow crack propagation independent of the biological mechanisms that actively remove damaged tissue [1]. Crack toughening mechanisms are generally classified into two types: intrinsic and extrinsic. Intrinsic toughening mechanisms occur ahead of the crack tip whereas extrinsic toughening mechanisms occur behind the crack tip [2]. Intrinsic toughening mechanisms limit microdamage, for example by dissipating energy in front of the crack tip thereby reducing local stresses experienced by the bone [1], [3]. The current thesis will investigate what we believe to be a visual indicator of a novel intrinsic toughening mechanism in the organic matrix of bone.

1.1.1 Water Compartments in the Bone Matrix

Bone is modeled as a fiber-reinforced composite material that consists of three phases: an organic phase (mostly collagen type I), a mineral phase (mostly hydroxyapatite), and extracellular fluid (mostly water) [1], [3]. Each phase plays a different role in the mechanical properties of bone. The organic phase is primarily responsible for toughness and strength while

the mineral phase is responsible for stiffness [2], [3]. Water serves as a plasticizer by breaking protein-protein and protein-mineral hydrogen bonds, and contributes very strongly to fracture toughness, Young's modulus, and post-yield material properties. Water is integrated into three different compartments of the bone matrix, each with its own structural roles (Figure 1.1) [4]. Nuclear magnetic resonance (NMR) studies have shown that water exists as **unbound** water (i.e., mobile, or free water) in the intra-cortical porosity, as loosely or tightly **bound** water at or within the surfaces of the mineral and organic phases, and as **structural** water within the collagen and mineral [5]–[8]. Strength and toughness increase with the amount of bound water whereas modulus of elasticity decreases with the amount of unbound water [5], [8]. As an aside, decrease in elastic modulus with the unbound water content is likely related to the fact that unbound water is largely in the bone's pores, meaning more unbound water is indicative of more porous bone. Moreover, it has been reported that the effect of water on the ultrastructural mechanical behavior of bone is loading-mode dependent, corresponding to strain-hardening in tension and strain-softening in compression, on the bulk tissue level [9]. As these mechanical properties are attributed to specific constituents of the bone matrix, they may fluctuate over time as those constituents age.

It is important to have a strong understanding of the structure of bone prior to delving deeper into the research. The role of water in bone is of particular significance to this thesis. In later sections, unbound and bound water will be discussed as they relate to the phenomenon of bone stress-whitening.

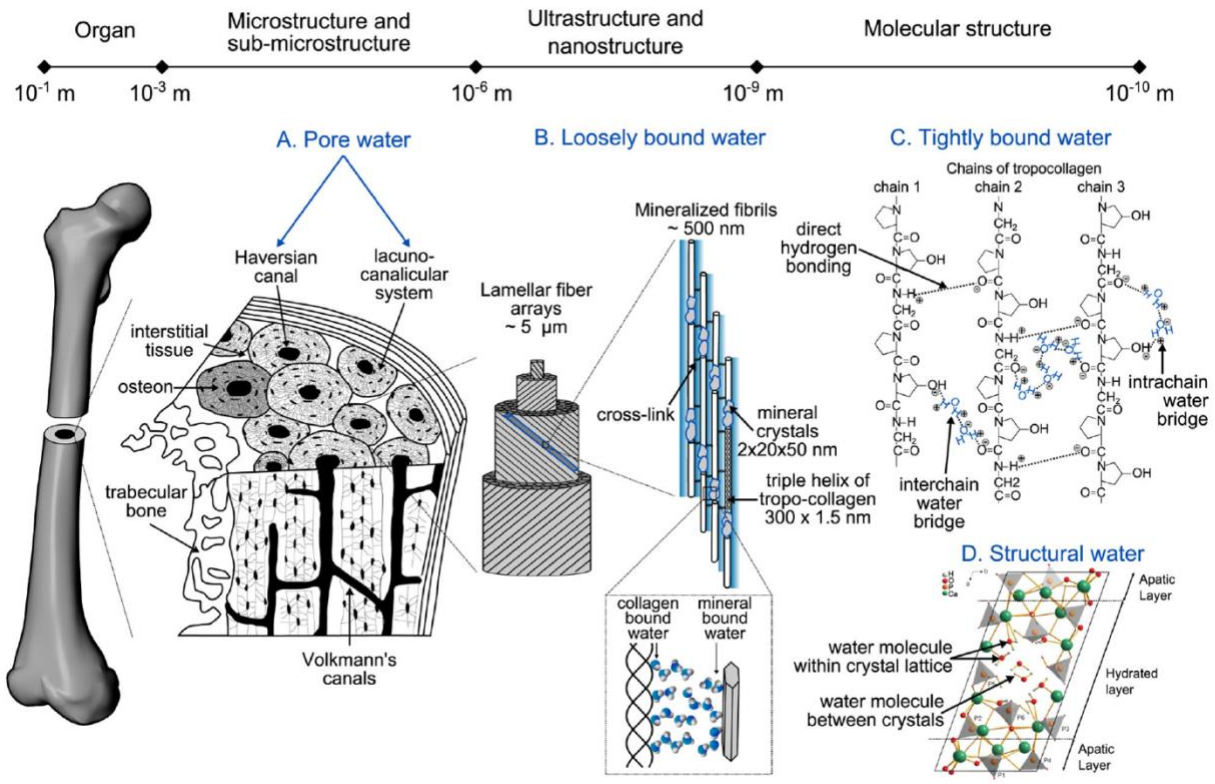

Figure 1.1: Location of water in the hierarchical structure of bone. (A) Microscale with pore water. (B) Loosely bound water. (C) Tightly bound water within the collagen fibrils. (D) Structural water within the core of the apatite [Reprinted by permission from Springer Nature: Springer Nature, Calcified Tissue International, "The Role of Water Compartments in the Material Properties of Cortical Bone," by Mathilde Granke et. al., Copyright (2015)]

1.1.2 Collagen and Other Proteins in the Bone Matrix

Collagen is the most abundant protein in mammals and can be identified by its recognizable triple helical structure [10]. Most simply, the fibrillar collagen molecule (tropocollagen) is a protein which consists of three polypeptide chains arranged in a triple helix that is capped at each end with non-helical carboxyl and amino terminals (Figure 1.2). The polypeptide chains are characterized by the repeating amino acid sequence Gly-X-Y, where X and Y are any amino acid residues other than glycine (frequently, the X and Y positions are proline and hydroxyproline, respectively). A single collagen molecule is approximately 300 nm long and has a diameter of 1.5 nm. The triple helical configuration is stabilized by direct chemical bonds including hydrogen bonds (mainly between the amide protons of the glycine

moieties and the carbonyl oxygen of the X moieties of the adjacent molecule) and water-bridged crosslinks. Collagen tissues are often referred to as “hierarchical,” as the individual collagen molecules assemble into microfibrils, which together form the collagen fiber [10], [11]. The specific form of collagen found in the organic matrix of bone is collagen type I, which is a heterotrimer consisting of two identical α1(I) chains and a third distinct α2(I) chain [10]. Due to the nature of our research involving bone matrix, collagen type I will be referred to simply as collagen as it appears in this thesis.

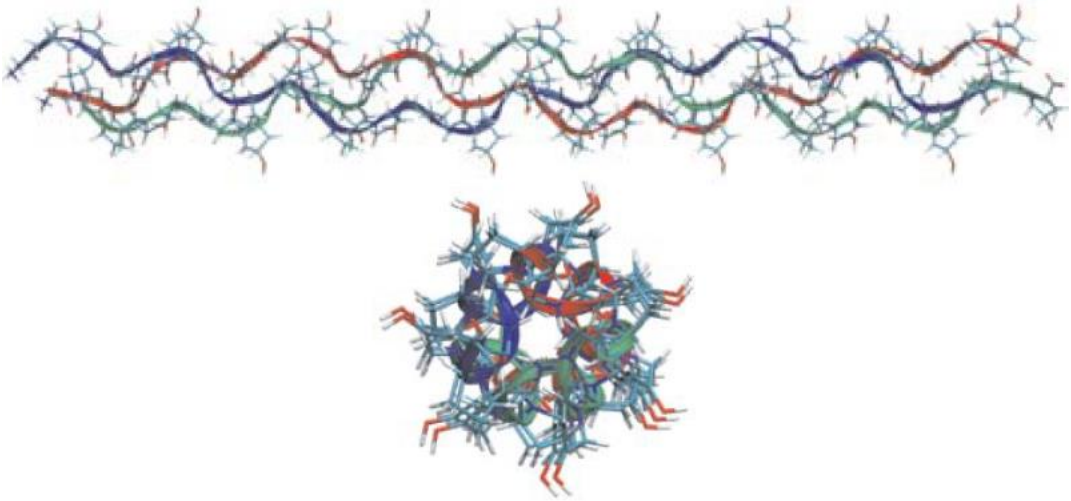

Figure 1.2: Side-view and end-view of a single tropocollagen triple helix. (Reproduced from Ritchie, Robert O., Markus J. Buehler, and Paul Hansma. "Plasticity and toughness in bone." (2009), with the permission of the American Institute of Physics.)

In addition to type I collagen, the organic phase of bone contains non-collagenous proteins such as proteoglycans (PGs) and glycosaminoglycans (GAGs). These non-collagenous proteins compose only about 1-2% of bone but have significant effect on the mechanical properties of hard tissues [1]. Through enzyme-mediated removal of small leucine rich proteoglycans (SLRPs) from crown and root dentin, it had been demonstrated that PGs significantly contribute to the fracture toughness of root dentin [12]. There was no difference in fracture toughness for crown dentin, upon removal of either PGs or GAGs. It was postulated that

this difference in the effects of SLRPs on mechanical properties of root or crown dentin may be attributed to their relative collagen content. It is posited that the higher tear energy of root dentin is perhaps attributed to the enhanced collagen content and collagen cross-linking of root dentin compared to crown dentin.

The protein in bone, most importantly collagen type I, plays an important role in the properties of the material. Later, the significance of collagen will be discussed as it relates to the observation of the bone stress-whitening phenomenon.

1.1.3 The Effects of Aging on Bone Material Properties

As bone ages, each of its three phases undergo changes that affect the overall bone quality. Measurements of fracture toughness in aging human cortical bone report a 40% decrease in crack-initiation toughness, and effectively an elimination of the crack-growth toughness (specimen age ranged from 34 to 99 years old) [13]. Over time there is little change in the mean degree of mineralization of bone [14]. However, aging of the organic phase leads to deterioration of the collagen fibrils which enable bone to dissipate energy under mechanical deformation, causing bone to lose its elasticity and become less tough [2]. It is generally accepted that aging increases nonenzymatic glycation crosslinking of the collagen in bone [10]. Increased crosslinking density detracts from the bone's ability to dissipate energy, thus greatly increasing the susceptibility to fracture [2].

Aging has been reported to influence the amount of water within bone, and subsequently its material properties. Some researchers have used solid-state NMR to correlate the age-dependent amount of bound and mobile water within bone to its mechanical properties [5]. The researchers reported that the amount of bound water in the bone decreases as a function of aging and demonstrated that the bound water is associated with strength and work to fracture. They

found no change in NMR-measured unbound water with age and found that mobile water is associated with modulus of elasticity. This was the first study to quantify distribution of water in bone for different age groups.

The effects of aging on the water content of bone and its mechanical properties aids in the understanding of how the material properties of bone may change as it experiences stress-whitening. The next section defines stress-whitening and its significance to this thesis.

1.1.4 Stress-whitening Phenomenon Observed in Bone

John D. Currey reported a visual whitening of bone mechanically loaded into the yield region when illuminated from the front, particularly near large stress concentrations [3]. This "stress-whitening" phenomenon is also observed ahead of propagating crack tips, like an intrinsic toughening mechanism [15]. Anecdotal observations indicated that stress-whitening is less discernible in bone that is dry, aged, mineralized, or that has a compromised organic phase, which has led to the belief that stress-whitening is consistent with normal bone toughness [3].

The molecular mechanism of visual whitening in bone immediately prior to mechanical failure has not yet been determined. Past researchers attributed stress-whitening to microdamage accumulation [16]. Specifically, stress-whitening was previously thought to be caused by cracking of the mineral phase. Research from our laboratory disproved this hypothesis by demonstrating that stress-whitening is a property of decalcified (i.e., demineralized) bone tissue [15].

Stress-whitening is not unique to bone, however. Optical whitening is commonly observed in polymers exhibiting crazing while undergoing mechanical deformation [17]. An alternate hypothesis for the cause of stress whitening is crazing of the collagen matrix [15], [18].

Crazes in polymers occur in highly stressed material and are typically situated perpendicular to the axis of tensile loading [19]. Unlike cracks, crazes can support loading [19]. Crazing is a known toughening mechanism of polymer materials [20]. Previous research in our laboratory however has demonstrated that stress-whitening occurs in a repeatable and reversible manner, and therefore it is not polymer crazing of the collagenous matrix in bone [15], [18].

As stress-whitening occurs ahead of the tip of a propagating bone crack, it follows that stress-whitening could be a visual indicator of an intrinsic toughening mechanism. The current research will use demineralized bone to further investigate the molecular mechanism of the stress-whitening observation.

1.1.5 Stress-whitening Is an Optical and Mechanical Phenomenon

Light scattering will occur in a material with a heterogeneous refractive index, such as when the material contains small particles. Mathematical theories have been developed to predict light scattering for different wavelengths of incident light. Rayleigh scattering models the interaction of light with particles that are much smaller than the wavelength. Mie scattering, however, explains the interaction of light with scattering particles that are approximately equal to the wavelength. Biological tissues mainly scatter visible light because their components, such as collagen fibrils, are of comparable size to the wavelength of visible light. Therefore, light scattering in collagenous tissues has been ascribed to collagen fibrils acting as Mie scattering particles [21].

Mie scattering theory predicts the reduced scattering cross section (σ_s') of a single scattering particle to be a function of the radius and refractive index of a scattering particle, the refractive index of the surrounding medium, and the wavelength of light in a vacuum. Furthermore, for a dense distribution of scattering particles, light scattering can be quantified

using the reduced scattering coefficient, μ_s'. The reduced light scattering coefficient is related to the reduced scattering cross section (σ_s'), the volume fraction of the scattering particles (ϕ), and the volume of a single scattering particle (V) by a heuristic model [21]:

$$\mu_s' = \frac{\phi(1-\phi)}{V} * \sigma_s'. \qquad (1)$$

This equation illustrates a parabolic relationship between μ_s' and the volume fraction of the scattering particles, ϕ (Figure 1.3). This means that at both extremes of volume fraction values, null (infinite space between scattering particles) and unity (no space between scattering particles), there is essentially no light scattering due to homogeneity of the refractive indices of the material.

The Mie scattering equation can be adapted to quantify the reduced light scattering for a biphasic (water and collagen) matrix [22]:

$$\mu_s' = \phi_{fibril}\left(1-\phi_{fibril}\right) * \left(\frac{n_{fibril}}{n_{sol}} - 1\right)^{2.09} * \left(\frac{3.28a^2\left(\frac{2\pi a n_{sol}}{\lambda}\right)^{0.37}}{V_{fibril}}\right). \qquad (2)$$

The amount of light scattering μ_s' is a function of the volume fraction of the collagen fibrils (ϕ_{fibril}), the ratio of the refractive index of the collagen fibrils (n_{fibril}) to the refractive index of the surrounding solution (n_{sol}), the volume and radius of the collagen fibrils (V_{fibril} and a, respectively), and the wavelength of incident light (λ).

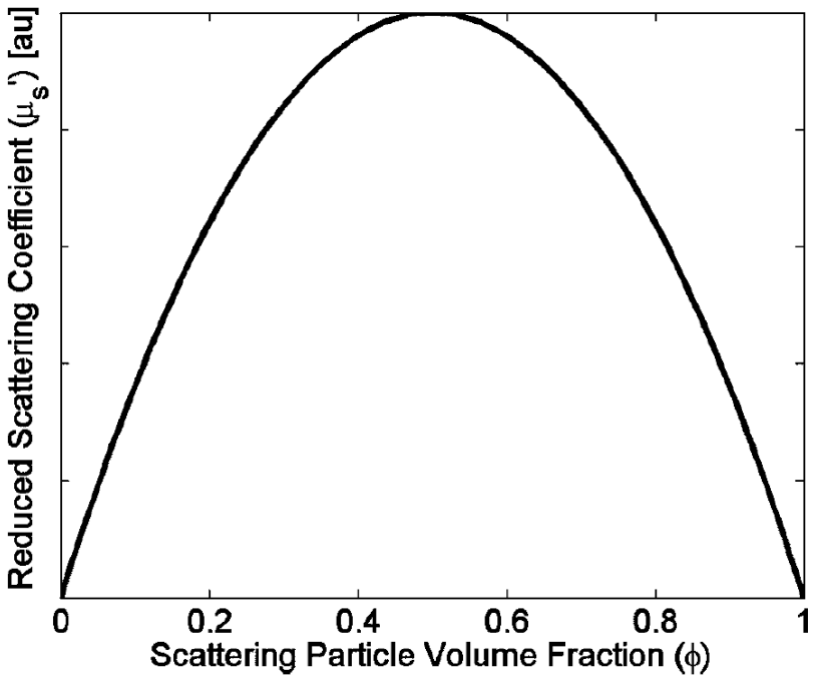

Figure 1.3: Relationship between reduced scattering coefficient and scattering particle volume fraction, provided all other variables are held constant. (Reused with permission from Christopher G. Rylander, Oliver F. Stumpp, Thomas E. Milner, Nathaniel Joseph Kemp, John M. Mendenhall, Kenneth R. Diller, Ashley J. Welch, "Dehydration mechanism of optical clearing in tissue," J. Biomed. Opt. 11(4) 041117 (1 July 2006) https://doi.org/10.1117/1.2343208)

Changing the amount of light scattering leads to visual changes in the material. For example, optical clearing (reduction of scattering) can be seen in tissues that have been treated with chemical agents such as glycerol or dimethyl sulfoxide [21]. Studies have shown that optical clearing is caused by dehydration of collagen on the fiber-level [21]. On the other hand, whitening is an increase in light scattering that may be caused by the same molecular mechanisms that are manipulated to clear collagenous tissues [18]. It follows that tissue optical clearing and optical whitening are potentially inverse mechanisms of each other.

But how can the amount of light scattering in a material be manipulated? This may be answered by referring to the empirical equation for light scattering in a collagenous matrix, Equation (2). Light scattering (μ_s') changes as a function of the volume fraction (ϕ_{fibril}) of the scattering particles and the heterogeneity of the refractive index of the region of interest ($\frac{n_{fibril}}{n_{sol}}$)

(Figure 1.4) [22]. The refractive index is used to characterize the interaction of light with a material, and heterogeneity of the refractive indices within a multiphase material change the intensity of light scattering.

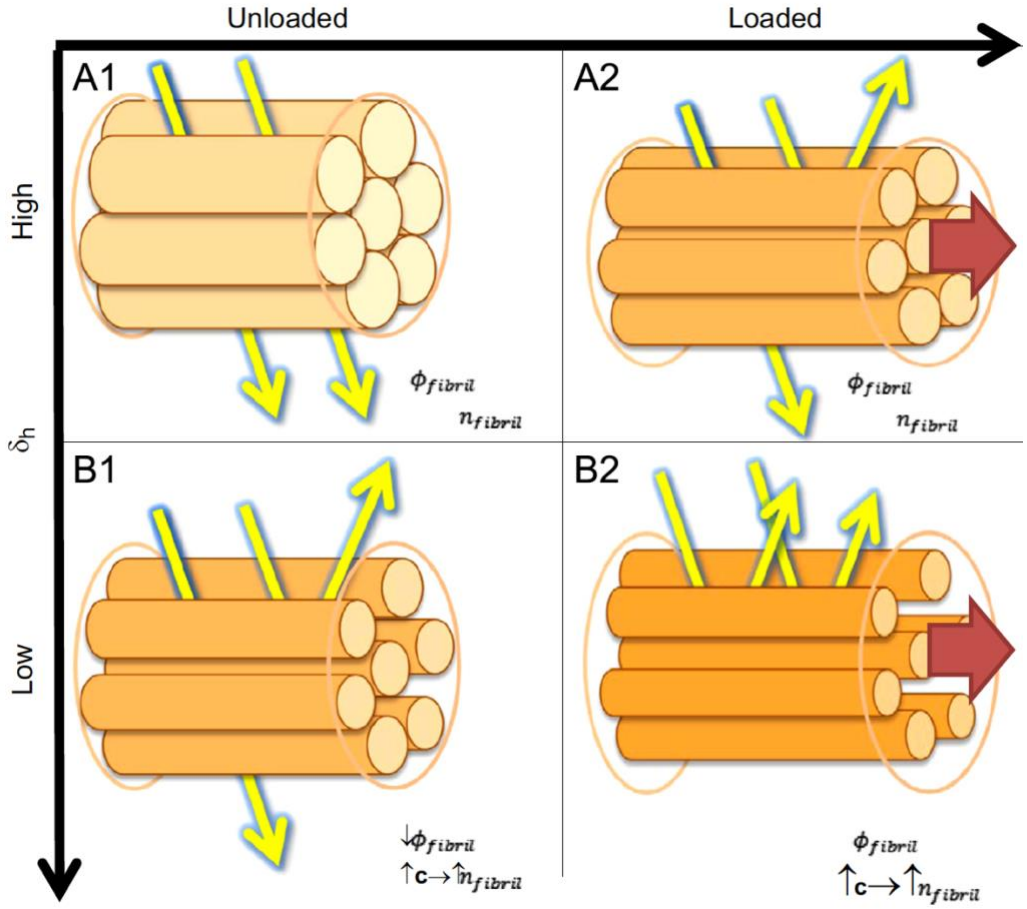

Figure 1.4: Model of collagen fibrils causing an increase in light scattering under various conditions (Reprinted from Journal of Biomechanics, Vol. 46, M.R. Hardisty, M.A. Soicher, T.C. Garcia, S.M. Stover, and D.P. Fyhrie, "Do stress-whitening and optical clearing of collagenous tissue occur by the same mechanism?" Pages No. 2411-2418, Copyright (2013) with permission from Elsevier.)

Our group has demonstrated that mechanical compression of demineralized bone increases the refractive index in a deformation-dependent manner [22]. Experiments were performed on demineralized bone specimens that had been immersed in deionized water or ethanol. Compared to the deionized water-treated specimens, the refractive index values of the ethanol-treated specimens were lower and less sensitive to deformation. As ethanol has a smaller

hydrogen bonding potential than water (see Section 1.1.6), it does not solvate collagen as well as water, which causes a decrease in the volume fraction of collagen and may explain the observed discrepancy in refractive indices. Therefore, it is plausible that changes in the distribution of refractive indices of demineralized bone may be a consequence of changes in the density (i.e., volume fraction, ϕ_{fibril}) of the collagenous matrix, consistent with the hypothesis of mechanically induced dehydration of collagen [22].

1.1.6 Hydrogen Bonding and Solvent-whitening

Hydrogen bonding plays an important role in bone material properties. Hydrogen bonds are responsible for holding the collagen triple helix in place prior to covalent crosslinking and are fundamental to forming the triple helix of the collagen type I molecule [23]. We aim to investigate the role of hydrogen bonding between collagen fibrils in the stress-whitening phenomenon. The effect of hydrogen bonding on stress-whitening and mechanical properties of bone has been interrogated by varying the Hansen's hydrogen bonding parameter (δ_h) of the solution, and hence the extent of hydrogen bonding, prior to mechanical testing [18]. Hansen's hydrogen bonding parameter indicates the ability of a solvent to form a hydrogen bond. When demineralized bone is immersed in high δ_h solvents the hydrogen bonds within the organic matrix are broken in favor of the solvent-solute interaction [18]. In lower δ_h solvents, the solvent has a lower affinity and more hydrogen bonds form between the macromolecules of the demineralized matrix. Water is the most common solvent with the largest δ_h, so (in general) modulation of hydrogen bonding by other common solvents results in an increase of intermolecular bonds.

1.1.7 Solvent-whitening Is Similar to Stress-whitening

Like stress-whitening, bone visually whitens when it is exposed to solutions with a lower Hansen's hydrogen bonding parameter than the matrix itself, meaning the solvent's ability to break the hydrogen bonds of the matrix is limited. Experimentally, our lab has found the δ_h value of bone to be between about 26 and 33 $MPa^{1/2}$ [15]. For discussion purposes, let us assume the δ_h value of bone is the average of those values, 29.5 $MPa^{1/2}$. Therefore, immersing bone in a solution with a δ_h value greater than 29.5 $MPa^{1/2}$ will cause the hydrogen bonding between collagen molecules to weaken. Contrastingly, immersing bone in a solution of a δ_h less than 29.5 $MPa^{1/2}$ will cause the matrix to "solidify." When the solvent has a Hansen's hydrogen bonding parameter that is lower than that of the collagen matrix, it is less likely to separate the hydrogen bonds within the collagen fibrils. This interaction effectively "dehydrates" the organic matrix and causes the collagen molecules to bind to each other. This binding of collagen molecules greatly reduces their molecular separation and displaces the water molecules. The change in scattering caused by solvent-induced dehydration of the bone matrix is called "solvent-whitening." We believe that solvent-whitening is caused by solvent-driven densification of the collagen fibers, which pushes out bound water from the collagen fibers, changes the distribution of refractive index, and increases scattering from the matrix, like that seen in stress-whitening [18].

Many have shown that immersing collagenous materials in solvents with low δ_h has a strong effect on the mechanical properties of biological tissue. For example, Pashley et. al. found that placing demineralized dentin in solutions of decreasing δ_h caused a decrease in toughness and an increase in stiffness [24]. On the contrary, Bembey et. al. showed that exposure to high δ_h solvents decreased the moduli of bone tissue [25]. Nalla et. al. found that both intrinsic and

extrinsic toughness are inversely related with δ_h in dentin exposed to polar solvents (including acetone, ethanol, and methanol), which have a lower Hansen's hydrogen bonding parameter than collagen [26].

Furthermore, not only did the study from Nalla's group find an increase in fracture resistance and initiation toughness upon exposure to the polar solvents (acetone, ethanol, and methanol), but this effect was reversible upon rehydration and again induced upon further polar solvent exposure. Finally, Nalla's group reported an increase in the stiffness and ultimate strength in solvent-exposed dentin specimen [26]. Although the results are inconsistent across studies, it is clear from overwhelming evidence that immersing collagenous matrices in solvents of varying Hansen's hydrogen bonding parameter values has major consequences on the material properties of the material.

1.2 Hypothesis

The underlying molecular mechanism of the stress-whitening phenomenon is still unknown. We hypothesize that this stress-whitening observation in demineralized bone is a consequence of a mechanically-driven change in the hydration state of the collagenous matrix, which increases tissue strength and stiffness by altering the intermolecular hydrogen bonding.

1.2.1 Potential Molecular Model for Stress-whitening

Stress-induced crystallization of type I collagen is one molecular mechanism to explain optical whitening. In 1928, Janet H. Clark published a paper in PNAS describing her investigation of reversible crystallization in tendons caused by mechanical loading [27]. Using x-ray diffraction, Clark observed the transition of collagen from a liquid crystal to a solid crystal state under tension. Clark inferred that, in healthy tissue, collagen exists in a liquid crystal state but changes to a solid crystalline state upon tension-induced dehydration due to the partial

depolymerization of the collagen molecules. She postulated that the initiation of crystallization causes a creation of surface energy which may be large for the formation of small crystals. Moreover, this sudden transition from a liquid to solid crystal state may greatly increase cohesion and resistance to extension (i.e., increase strength and stiffness). This mechanism was observed in viscoelastic tissues containing collagen but was absent in non-collagenous elastic tissues (e.g., elastin) [27]. Clark's discovery was described in the scientific terms extant at the time of her work, prior to the development of a greater understanding of macromolecular mechanics in the 1950's to the present. Her hypothesis of mechanically-induced crystallization of collagen type I in tendon is consistent with our hypothesis that mechanical loading alters the water content of bone matrix and induces greater intra-collagenous hydrogen bonding, which would appear in x-ray diffraction as a crystallization transformation. From work directly on collagen from many laboratories, it is known that reduction of the water content of collagenous matrix increases the strength and stiffness, which is consistent with Clark's postulation of increased strength and stiffness caused by mechanically-induced crystallization. We believe that the observations of Clark were the earliest demonstration of a crystallization transition in collagen caused by mechanical deformation.

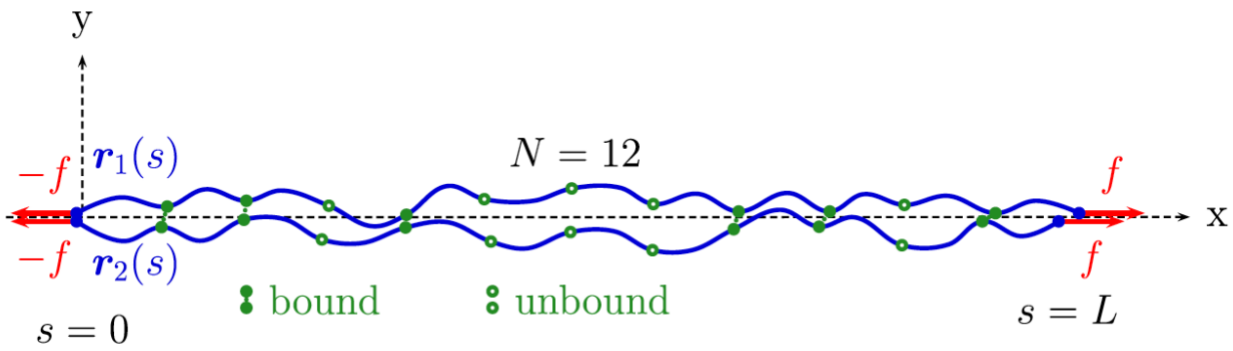

Figure 1.5: Model for 11 reversible interchain crosslinks. (Reprinted from "Tension-induced binding of semiflexible biopolymers" by Panayotis Benetatos et. al., 2014, *New J. Phys.*, **16,** 113037. This work is licensed under the Creative Commons Attribution 3.0 Unported License. To view a copy of this license, visit http://creativecommons.org/licenses/by/3.0/ or send a letter to Creative Commons, PO Box 1866, Mountain View, CA 94042, USA.)

There have been attempts to build a molecular model to illustrate the mechanically-induced crystallization reported in polymers under tensile loading. Benetatos et. al. introduced a model for tension-induced self-binding of semiflexible biopolymers [28]. The model describes a pair of reversibly crosslinked semiflexible polymer filaments undergoing stretch (Figure 1.5). The expected distance between the binding sites of the polymers is determined by the entropic configurations of the molecules. As tension increases, the expected distance between the molecules decreases and hence the total entropy of the system decreases. The molecules are stretched and can explore fewer configurations, and thus the propensity for intermolecular binding increases. In this theory the ability of the solvent to break intermolecular bonds is introduced explicitly, making it possible to predict the effects of "better" and "worse" solvents on simulation results. For a good solvent, this two molecule system results in a discontinuous transition from weakly bound at low tension to strongly bound at high tension at a critical force. Benetatos and colleagues postulated that the jump between weakly and strongly bound states indicated a potential force-stiffening molecular mechanism of biopolymers. Higher tensile loads increase the amount of intermolecular crosslinking, hence increasing the tensile stiffness and

strength of the system. Ultimately the system increases its stiffness and strength in response to the increasing external loading experienced [28]. The work of Benetatos and colleagues offers a potential explanation for the molecular mechanism which leads to stress-whitening in the organic phase of bone: whitening is the optical expression of increased lateral molecular crosslinking induced by tension. Also, though they did not explore it, the ability to model different solvent strengths could also help with understanding solvent-whitening. Overall, the molecular model proposed by Benetatos et. al. is consistent with my hypothesis since increased inter-molecular crosslinking must, necessarily, displace bound water from the matrix causing local "dehydration."

The independent theories by Clark (1928) and Benetatos et. al. (2014) describe a quick change from an unbound to bound (or from liquid to crystalline) state of biopolymers upon tensile loading. We believe these models offer a molecular mechanism for the whitening effect observed in bone that is reported during loading and immediately prior to mechanical failure.

1.2.2 Spinodal Decomposition as a Potential Thermodynamic Model for Stress-whitening

There is another possible model for stress-whitening originating in thermodynamics that does not rely on a specific molecular mechanism. In the polymer science literature, it is well known that spinodal decomposition, or the separation of a solution into polymer-rich and solvent-rich regions, occurs under shear stress and tensile strain [29]. Spinodal decomposition is unique compared to other thermodynamic phase decomposition mechanisms because it initiates when the solution is thermodynamically unstable, meaning there is no nucleation barrier that needs to be overcome to initiate the phase transformation [30]. The Cahn-Hilliard free energy equation is typically used to model the dynamics of spinodal decomposition [30]. For polymer solutions, the spinodal line on a phase diagram separates the stable and unstable regions for

which the polymer will spontaneously separate from the solvent [29]. This phenomenon of strain-induced phase separation in strained polymers is an alternative explanation for the stress-whitening phenomenon observed in bone.

Spinodal decomposition also may explain solvent-whitening, as it is similar to the concept of phase separation caused by discrepancies between δ_h values of a solute and solvent. We believe that mechanical loading may increase the δ_h value of the bone matrix such that it becomes greater than the δ_h of the solution. An increase in δ_h of the bone would cause the matrix to "solidify" and cause a spinodal decomposition from a solvated collagenous matrix to separate and distinct collagen and solvent phases.

1.2.3 The Polymer-in-a-Box Theory for Collagen Molecules

First described by Miles and Ghelashvili, the polymer-in-a-box theory can be used to integrate the aforementioned molecular models into a single hypothesis to explain stress-whitening [31]. The polymer-in-a-box hypothesis can be thought of as analogous to placing the model for tension-induced binding of semiflexible biopolymers from Benetatos et. al. in a tube (Figure 1.6). The polymer-in-a-box theory describes a concept of thermal stabilization of collagen molecules in which the molecule loses configurational entropy via confinement in the fiber lattice. This restrained movement of collagen is likened to being placed in a box which limits its movement, but in this case the "box" consists of the other collagen molecules in the fibril. The width of the box, a_0, can change depending on conditions such as temperature, the hydration state of the collagen, and the level of crosslinking. The more confined the collagen molecules, the greater the reduction in configurational entropy. Limiting the possible configurations of the molecules increases the propensity for intermolecular binding and expels water from between the collagen molecules. Simply, the molecules have less entropic freedom

and are more likely to bind to each other instead of the solvent. This causes the collagen molecule to be more strong, stiff, and thermally stable. We hypothesize that the width of the box also changes during loading (e.g., tension and osmotic pressure). For this reason, we will refer to the polymer-in-a-box theory throughout the thesis and use it as a guiding principle for our experiments.

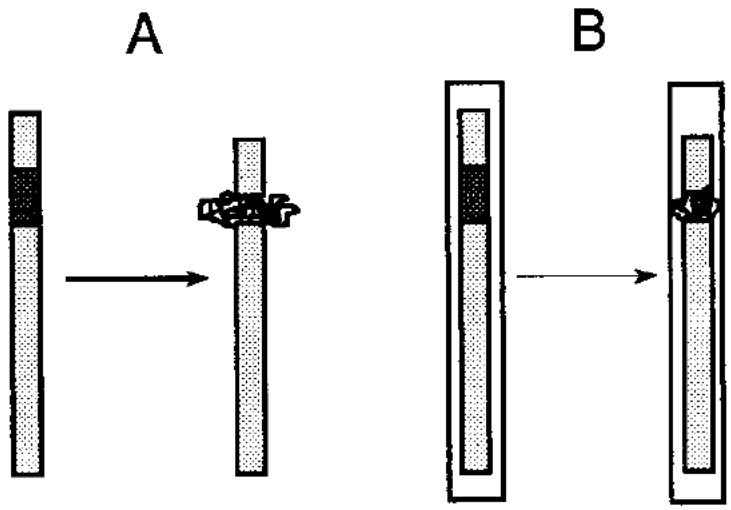

Figure 1.6: Polymer-in-a-box Model sketch. (Reprinted from Biophysical Journal, Vol. 76, Miles et. al., "Polymer-in-a-Box Mechanism for the Thermal Stabilization of Collagen Molecules in Fibers," Pages No. 3243-3252, Copyright (1999), with permission from Elsevier.)

Miles and Ghelashvili conducted experiments to validate their polymer-in-a-box hypothesis. Their methods were based simply on manipulating the lateral spacing of the collagen molecules (aka the width of the box) by altering the volume fraction of water within their dilute collagen samples, and then measuring the thermal stability of these samples upon heating. Specifically, the group measured the temperature of denaturation, enthalpy of denaturation, and width of the endotherm at half-height of fibers at varying levels of hydration using differential scanning calorimetry (DSC). The hydration levels were broken into four regions: high (> 30 molecules of water per Gly-X-Y unit), intermediate (6-30 molecules per unit), low (~1-6 molecules per unit), and very low (< ~1 molecule per unit). It is important to note that this study

specifically analyzed loosely bound water (as opposed to tightly bound or unbound water) and was the first study to investigate low levels of hydration. For high levels of hydration, the authors reported a nearly constant enthalpy of denaturation at about 59 J/g, due to the collagen being saturated with water bonds thus all potential water-bridges having been formed. For low levels of hydration, there was a decrease in enthalpy of denaturation which the authors argue is attributed to the lesser amount of hydrogen bonds to break in order to separate the α-chains of the tropocollagen. Finally for very low levels of hydration, the enthalpy of denaturation remained relatively constant at about 12 J/g, which the authors attribute to the possibility that the water is not involved in forming interchain water bridges. The denaturation temperature steadily increased with dehydration for all levels of hydration apart from the high hydration region (> 30 molecules of water per Gly-X-Y unit), for which denaturation temperature remained constant.

The DSC experiment and data confirmed the derived hyperbolic relationship between the denaturation temperature and volume fraction of water in the fiber, for water volume fractions greater than 0.2. Thus, the data collected in this experiment agrees with the polymer-in-a-box theory, illustrating that confining collagen fibers in a lattice serves to decrease their configurational entropy and therefore thermally stabilize the molecule. All the experiments and analysis of this theory were conducted regarding the denaturation of unrestrained collagen; however, the authors assert that the polymer-in-a-box theory can be generalized to fibers undergoing tension [31].

Most of the literature is consistent with the hypothesis that stress whitening is an optical expression of collagen dehydration, increased lateral hydrogen bonding, and a decreased box-width. However, an alternate mechanism is also possible, based on the findings of Ghanaeian et. al. [32]. Ghanaeian and coworkers used a molecular dynamics simulation of a virtual creep test

to investigate the viscoelastic properties of proline-rich and hydroxyproline-rich collagen structures. They reported that, in response to increased tensile loading, the model showed a decrease in protein-protein hydrogen bonds in hydroxyproline-rich collagens, and an increase in protein-solvent hydrogen bonds. Interestingly, the observed changes in intermolecular and intramolecular hydrogen bonding occurred within the first picosecond of applied pulling force [32].

The simulation results reported by Ghanaeian and colleagues provide an alternative mechanism to explain the stress-whitening phenomenon. Taking these findings into consideration, perhaps increased pulling force causes the collagen triple helix to "deregister," opening the tight regions of the collagen molecule, allowing the molecule to increase in hydration. If this type of mechanism dominates, then whitening would be associated with an increase in bound water instead of a decrease.

Since the amount of bound water in the collagen can only increase, stay the same, or decrease under mechanical loading, we will use Raman spectroscopy (more on Raman in Section 1.2.9) to measure the change in collagen bound water in demineralized bone during stress-whitening. Increased bound water would be consistent with mechanical loading separating hydrogen bonds in the molecule, decreased bound water consistent with a decreased box-width, and no change in water content will be evidence against each mechanism. The preponderance of the literature supports a prediction that bound water will decrease during whitening.

1.2.4 Potential Effects of Temperature on Stress- and Solvent-whitening

Collagen denatures upon heating, meaning that as the temperature increases past the denaturation point, the crystalline structure of the collagen collapses into random gelatinous chains [10]. The denaturation temperature varies depending on the source of the collagen. This

difference has been correlated to the amount of proline and hydroxyproline in the collagen, which interacts with water to stabilize the collagen triple helix [10]. Intermolecular crosslinks also are known to increase the thermal stability of collagen. For example, in industrial settings, extensive dehydration is used to create an insoluble cross-linked collagen with a high denaturation temperature. This increase in thermal stability is associated with the water content of the fibrils [33]. Increased crosslinking reduces the intermolecular space (i.e., makes the "box" width smaller) hence reduces the water content between the collagen molecules. For collagen in bone, the denaturation temperature is relatively high (155°C) because the mineralization reduces the water content. However, in demineralized bone, the collagen denatures at a lower temperature (65°C) [10].

On a molecular level, rising temperature increases the off time and decreases the on time of the hydrogen bonds. Hence, when more thermal energy is put into the system, the hydrogen bonds are more likely to break and cause the collagen to swell into an unbound state (in which water infiltrates between the individual tropocollagen molecules). This unbinding is temporary; the sections of the molecule that were unbound will often rebind unless the structure of the triple helix collapses because of complete melting of the hydrogen bond structure. At increasing temperatures, the likelihood of unbound sections to rebind correctly decreases until the collagen denatures, which essentially means the interfibrillar bonds are permanently disrupted and the collagen becomes gelatin. Dry collagen requires much higher temperatures to denature because there are fewer bonds separated by solvent. When there is less configurational entropy, the individual tropocollagen molecules are more confined by their neighbors in the fibril, delaying bond breaking.

Collagen molecules have thermally labile domains in which there are fewer potential hydrogen bonding sites than in the rest of the molecule. In type I collagen, the thermally labile domain is a 65-residue long, hydroxyproline-free sequence near the C-terminus of the molecule [31]. At any temperature this domain is more likely to melt than other stretches of the molecule, permitting water to infiltrate the molecule. When the temperature is increased, even the more tightly bound regions of the collagen molecule become increasingly unstable due to the increased energy of molecular motion of both water and the collagen itself.

Crosslinking between collagen fibrils induces the loss of water and subsequently increases the denaturation temperature and mechanical strength of the tissue. Dehydration also stiffens the collagen. Taking these together, we believe that stress- and solvent-whitening will impose an increase in the denaturation temperature of the collagen within the demineralized bone samples accompanied by an increase in strength and stiffness.

1.2.5 Potential Effects of Osmotic Pressure on Stress- and Solvent-whitening

Similar to dehydration via mechanical stress, it has been shown that osmotic forces serve to decrease the box-width in the polymer-in-a-box theory, thus dehydrating the tropocollagen and reducing the molecular spacing. Induction of osmotic pressure through immersion of collagen in a concentrated solution of non-penetrating neutral solutes, e.g., polyethylene glycol (PEG) or dextran, will compress the collagen fibrils, pushing out the water molecules and bringing the collagen molecules closer together [34]. This occurs because the solute applies an external force via osmotic pressure which balances with the net repulsive stresses between the collagen helices [34].

The effect of increased osmotic pressure on the mechanical properties of collagen has been studied previously. Andriotis et. al. conducted a study in which they manipulated individual

collagen fibril mechanics by utilizing varying concentrations of large, nonpenetrating PEG to exert osmotic pressure on the macromolecules and change the hydration state of the fibrils by direct compression of the macromolecules [35]. They used atomic force microscopy (AFM) to measure the mechanical properties of the collagen fibrils at physiologically relevant strain values. Andriotis and colleagues reported that for PEG-treated specimens, compared to physiologically relevant saline-treated specimens, they observed up to a 24-fold increase in collagen fibril stiffness for nanoindentation and up to a 6-fold increase for tensile-loaded specimens. The group speculated that this reversible stiffening mechanism may be attributed to the dehydration of fibrils bringing the tropocollagen molecules closer together (decreasing the box-width) and increasing the propensity for interfibrillar binding, thus increasing the necessary force to separate the molecules under tension.

Although it has not been shown (to our knowledge) we expect that increasing the osmotic pressure, hence dehydrating the collagen matrix, will have a similar "stress-whitening" effect as for specimens placed in a dehydrating ethanol solution or under mechanical loading. We suspect PEG mechanical compression is a potential factor to cause stress-whitening and increase bone strength and stiffness.

1.2.6 Potential Effects of Crosslinking on Stress- and Solvent-whitening

There are various methods of collagen crosslinking, including physical and chemical methods [11]. Physical methods include drying, heating, or exposure to radiation. Chemical methods rely on treatment with crosslinking agents such as glutaraldehyde, formaldehyde, polyepoxy compounds, acyl azide, carbodiimides, and haxemethylene diisocynate [11]. Specifically, addition of chemical crosslinking agents stabilizes the tissue by inducing intra- and intermolecular bonding between the collagen molecules decreasing their intermolecular spacing

[11]. This densification of the molecules via crosslinking serves to expel water from within the fibers. Dehydration of the collagen in this way increases the stiffness of the material by decreasing the box-width and confining the collagen fibrils.

Crosslinking collagen to change the material properties of collagenous materials dates back centuries. Tanning, for example, is the process of treating animal skins and hides to produce leather that is durable and impervious to thermal, enzymatic, and microbial attacks [36]. To give the leather its stiffness, the hides are placed in a crosslinking agent such as chromium (III) sulfate, so the collagen molecules bind to each other [37].

Collagen crosslinking has useful applications that surpass leather production. Collagen harvested from an organism immediately begins to degrade; crosslinking serves to prolong the collagen's mechanical integrity and neutralize antigenic properties [11]. This method of preservation is useful because it enables the collagen to be used for medical applications such as bioprostheses.

Moreover, the mechanisms of chemical crosslinking have been investigated thoroughly with the aim of varying the mechanical properties of tissues such as gelatin to make them more suitable for biomedical applications. Glutaraldehyde is the most frequently used crosslinking agent due to its ability to stabilize collagen very efficiently through reaction of the aldehyde group with the free amino group of the lysine or hydroxylysine residues of the collagen chains [38]. One research group specifically interrogated the effects of varying degrees of glutaraldehyde crosslinking on the mechanical and thermal properties of gelatin films [38]. They found that increasing glutaraldehyde crosslinking dramatically increased the stiffness of the gelatin films. Even at low glutaraldehyde concentrations, the extensibility of the samples was reduced by about one order of magnitude compared to the control samples. Using differential

scanning calorimetry, the study also found that glutaraldehyde crosslinking also increased the thermal stability of the gelatin films, shown in the thermogram by an increase in the denaturation temperature and a decrease in the denaturation enthalpy [38]. The authors ascribe the decreasing denaturation enthalpy upon increasing glutaraldehyde crosslinking to a reduction of interfibrillar hydrogen bonding and an increase in covalent crosslinking.

We hypothesize that increased collagen crosslinking decreases the box-width and therefore the box-width will be less sensitive to mechanical loading because it has been pre-strained. We expect this to cause a decrease in the amount of whitening observed during tensile loading because the collagen was “almost white” due to the strain of crosslinking. From prior knowledge, we assert that the box-width confining the collagen decreases due to the dehydration and stiffening of the matrix caused by the collagen crosslinking.

1.2.7 Potential Effects of Electrostatic Interactions on Stress- and Solvent-whitening

The stability of the collagen triple helix depends on electrostatic interactions between the charged moieties of the tropocollagen monomer. Researchers have shown that changing the electrostatic interactions between collagen molecules can change the stability and morphology of the constituent collagen [39]. For example, one study found that the denaturation temperature of collagen increased with increasing values of pH (more basic) in a sigmoidal fashion [40].

More recent studies have explored the effects of electrostatic interactions on the mechanical properties of collagenous materials. Grant et. al. illustrated that the mechanical properties of hydrated collagenous fibrils may be manipulated by changing the electrostatic interactions of the molecules, by way of altering the salt concentration and pH of the solution [41]. They demonstrated an increase in the elastic modulus of collagen molecules as a function of NaCl concentration. They reported a 2.3-fold increase in elastic modulus when 1M NaCl was

added to the collagenous solution. To investigate whether these effects were ion-specific or dependent upon ion strength, the group tested multiple monovalent chloride solutions at 1M concentrations. They reported that at high salt concentrations, the increased elastic modulus was attributed to ionic strength of the solution rather than cation species. In the same study, the researchers assessed the effect of changing pH on the Young's modulus of the specimens. Upon decreasing the pH from 7 to 5 via the addition of 1M KCl, they reported a 7-fold increase in the modulus [41].

In contrast to these results, Leikin et. al. reported a larger separation between tropocollagen molecules upon decreasing the pH of their collagen films [42]. Moreover, the previously mentioned study by Andriotis et. al. found that using 3.5 M PEG to increase the pH of a PBS solution (pH of 7.5 without PEG) to 8.8 caused a 24-fold increase in the indentation modulus of the sample [35]. The research group posited that the increase in indentation modulus, unexpected in comparison to the results of Grant et. al., may be attributed to the compression dehydration caused by the introduction of PEG molecules. Their conclusion is that dehydration effects override pH effects in collagen fibrils [35].

1.2.8 Movement of Water Is the Underlying Theme

All the effects that have been mentioned thus far (i.e., temperature, osmotic pressure, crosslinking, salt concentration, and pH) have been reported to cause changes in the location of water within bone and the hydrogen bonding within the collagenous matrix. Synthesizing these observations, we believe that the movement of water must correspond to stress-whitening and subsequently intrinsic toughening of bone. To investigate this theory, it is necessary to choose a tool that can non-invasively interrogate the location of water at the molecular level. Raman spectroscopy perfectly suits this purpose.

1.2.9 A Brief Introduction to Raman Spectroscopy

Raman spectroscopy is a contact-free optical technique that harnesses the power of electromagnetic radiation to measure the chemical composition of a material [43]. Consider the instance in which a particle of electromagnetic radiation (a photon) is directed at a molecule. The interaction with light causes the molecule to excite to a virtual state (i.e., the photon induces a dipole moment in the chemical bonds of the molecule). When the molecule returns to the ground state, a photon is emitted. The emitted photon will appear in one of two states: elastic (Rayleigh scattered) or inelastic (Raman scattered) [43]. The elastically scattered photons have the same wavelength (frequency) as the incident photon, but the inelastically scattered photons differ in wavelength from the incident photon. The change in the frequency of the Raman scattered light depends on the bond configuration of the scattering molecule.

In Rayleigh scattering, the molecule relaxes back to its original vibrational level once the photon is emitted (Figure 1.7). This type of light scattering does not provide useful information about the chemical components of the material because the wavelength is unchanged [44]. Conversely, when Raman scattering occurs the molecule returns to a vibrational level that is one vibrational quantum lower (Anti-Stokes) or higher (Stokes) than the original level (Figure 1.7) [43]. Therefore, inelastic light provides information about the chemical components. Unfortunately, only 1 in 10^6 photons are inelastically scattered, so sensitive devices are needed for detection.

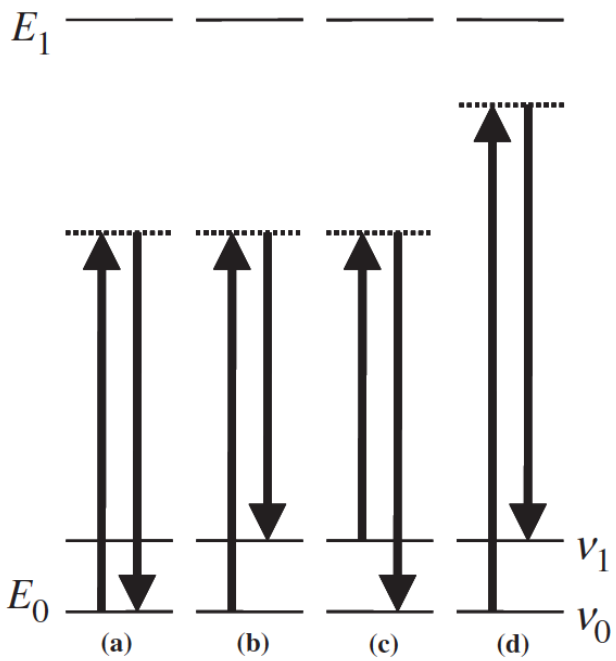

Figure 1.7: Energy level diagram illustrating spontaneous: (A) Rayleigh scattering; (B) Stokes Raman Scattering; (C) anti-Stokes Raman scattering; (D) Stokes Raman scattering using a different excitation wavelength. (Reprinted from *Raman, Infrared, and Near-Infrared Chemical Imaging* Edited by Slobodan Sasic and Yukihiro Ozaki, "1 Spectroscopic Theory for Chemical Imaging" by Pelletier et. al., Page No. 10, Copyright (2010), John Wiley & Sons, Inc.)

Raman scattering can be used to infer the chemical constituents of the material [44]. Analysis of Raman spectra characterizes the chemical composition of the sample. For this reason, it is common to hear Raman spectra referred to as "chemical fingerprints." A Raman spectrum is a plot of intensity of Raman scattering versus the Raman shift (the difference between the frequency of scattered light and the frequency of incident light) [44]. Each peak on a Raman spectrum correlates to a specific molecular bond vibration; its intensity directly relates to the concentration of that analyte in the sample, and how the bond is deformed by external effects such as mechanical stress. The relative concentrations of mixtures can be assessed by comparing the relative peak intensities on the Raman spectrum. Additionally, a Raman spectrum identifies the energy shifts the incoming photon experiences when interacting with each Raman-active

analyte. Raman spectroscopy can measure vibrational energies in the range of 17 to 4,000 cm^{-1} (i.e., from the ultraviolet to the near-infrared region) [43].

The optical setup consists of a light source with a specific wavelength focused on a dichroic filter which reflects light perpendicularly onto the sample. The Raman scattered light is then reflected to the dichroic filter and redirected via mirrors to a monochromator which diffracts the beam into narrow bands of wavelengths using grating. A notch filter is used to remove any unrefracted Rayleigh scattered light. Finally, a detector (typically a charge-coupled device, i.e., CCD detector) is used to measure the photo current from each wavelength and convert it into electric current for further evaluation [44].

Raman spectroscopy can be easily combined with a standard optical microscope, including a confocal microscope for analysis of molecules on the micron-level [45]. When combined with a motorized stage, thousands of Raman spectra of a single sample can be acquired from a variety of positions and angles to provide a comprehensive spectrum of the entire sample [45].

The simplicity and flexibility of Raman spectroscopy makes it well suited for a variety of applications including artwork, pharmaceutics, polymers, and minerals, since almost any sample that contains molecular bonds can be analyzed using this method [45]. Raman spectroscopy can be used to analyze many organic, inorganic, and biological materials.

1.2.10 Measurement of Water Movement In Tissues by Raman Spectroscopy

As Raman spectroscopy is a non-invasive, label-free tool suited for biological specimens, it presents itself as a great tool for the purposes of interrogating water content and location within demineralized bone samples. Specifically, Raman spectroscopy will be used to investigate the

mechanically-driven changes in water location within bone by measuring changes in the integrated Gaussian OH-stretch component intensity ratio, *K*. It has been reported that water within collagen behaves as if it is supercooled when the collagen molecules are close together, whether caused by dehydration or osmotic pressure. To explain this effect, Walrafen et al. characterized *K* for collagen and showed that Raman OH-stretching component intensity ratio

$$K = {}^{I_{3250\ cm^{-1}}}/_{I_{3400\ cm^{-1}}} \qquad (3)$$

is proportional to the ratio of bound to free water in a collagen fibril [46]. Using this ratio, we can measure the effects of different stress-whitening factors (e.g., tension, dehydration, and other methods as discussed above) on the movement of water between compartments within the bone (i.e., the transition between bound water and free water). Based on the current literature and past research in the laboratory, our theory is that mechanical loading causes a decrease in the box-width, which increases the intra- and interfibrillar hydrogen bonding, subsequently reducing the bound and increasing the unbound water. In other words, we expect to see a decrease in the *K* value upon tensile loading, which corresponds to a "dehydration" of the decalcified bone matrix.

To increase the signal-to-noise ratio when measuring *K*, water in a biological specimen is often replaced with deuterium oxide (D_2O, also known as "heavy water"). Deuterium (D) is a stable isotope of hydrogen with mass 2 [47]. Due to the differences in mass, chemical bonds with deuterium will have distinct vibrational frequencies compared to bonds with hydrogen. In fact, deuterium bonds have slight lower frequencies and are more stable than corresponding hydrogen bonds [47].

Hydrogen-deuterium (H/D) exchange has been used to qualitatively assess the amount and location of water in bone by monitoring the decrease in the OH-stretch mode (3000-3800

cm^{-1}) and the increase in the OD mode (2200-2800 cm^{-1}). For example, one study used a sequential dehydration technique to remove free and bound water from control and demineralized bone samples, then immersed the samples in deuterium oxide and longitudinally measured the changes in the Raman OH-band (with time points of 1, 5, 15, 60 minutes, 24 hours, and 7 days) [48]. The aim of their study was to discern the Raman signatures of free and bound water by observing the reduction of the OH-stretch band via hydrogen-deuterium exchange. The rate of H/D exchange provided data on the accessibility and binding affinity of water molecules within control and demineralized bone samples. The group reported that, using this technique, they were able to determine that the OH-stretch band is associated mainly with water molecules bound to the collagenous matrix [48].

Another research group used H/D exchange coupled with Raman spectroscopy to measure hydration changes in porcine pericardium tissue that had been treated with the crosslinking agent glutaraldehyde (GA) [49]. As crosslinking has been reported to dehydrate collagen, part of their analysis included measuring the integrated intensity ratio *K*, and they reported a decrease in *K* for the glutaraldehyde cross-linked samples. The researcher's interpretation is that GA-crosslinking caused an increase in the number of water molecules in the hydration shell surrounding the collagen of the pericardial tissue and an increase in the interaxial distance between collagen triple helices [49].

1. 3 Aims

The primary purpose of this thesis is to determine whether stress-whitening is an effect of molecular level dehydration *caused by any means,* including direct pressure on the tissue by osmotic forces, tension induced crystallization (i.e., the independently developed theories of Clark (1928) and Benetatos et. al. (2014)) or in tension as described by a theory of spinodal

decomposition. The following aim outlines the experiment we designed to investigate the hypothesis that stress-whitening in demineralized bone is a consequence of stress-driven alteration of the box-width confining the collagenous matrix, which increases tissue strength and stiffness by altering the intermolecular hydrogen bonding. We have chosen methods that enable us to investigate whether increased pulling force will **increase** the intermolecular hydrogen bonding (as we strongly believe to be the case) or **decrease** the intermolecular hydrogen bonding (as suggested by Ghanaeian et. al.).

Specific Aim: Measure the effect of tension on the Raman signature of demineralized bone and determine how the Raman signature correlates with stress-whitening. To accomplish this, I will utilize Raman spectroscopy to measure molecular changes in demineralized bone upon loading in tension. I will use an H_2O/D_2O solvent exchange to visualize stress-induced dehydration by comparing the relative intensities of the OD and OH spectral peaks. Moreover, I will measure changes in the *K* ratio to assess the movement of water within demineralized bone during loading. The results will enable me to characterize the relationship between the Raman signature and stress-whitening of demineralized bone tissue. The hypothesis is that tension causes *K* to change in a way that is consistent with dehydration while the demineralized bone undergoes stress-whitening.

1.4 Impact

The findings of this research could have the potential to improve the methods for designing strong polymers by the anti-fracture mechanism of collagen. At a minimum, the investigation will add to our understanding of the ultrastructural mechanisms of bone mechanics. The current research also has the potential to supplement our understanding of bone diseases

associated with changes in molecular mechanics and disruption of intermolecular hydrogen bonding, such as osteogenesis imperfecta [50].

Outside of increasing our knowledge base, there is also a potential clinical application for this research. If stress-whitening is correlated with changes in the Raman spectral parameter *K* in human bone, there is a potential to develop a clinical diagnostic tool which utilizes Raman spectroscopy to measure *K* to predict fracture risk. It is my hope that the results of this research will contribute to the development of new medical technology and empower clinicians to diagnose patients whose bones are at risk of catastrophic failure.

Another clinical application of this research is the potential to understand the mechanism of action of chemical agents that increase bone toughness (e.g., risedronate) by increasing bone hydration. If we are successful in demonstrating that mechanical tension causes dehydration-induced strengthening (i.e., an intrinsic toughening mechanism) then this affect can be utilized to produce therapeutic agents for the prevention of fracture disorders.

References

[1] R. B. Martin, D. B. Burr, N. A. Sharkey, and D. P. Fyhrie, *Skeletal Tissue Mechanics*, 2nd ed. New York: Springer, 2015. doi: 10.1007/978-1-4939-3002-9.

[2] R. O. Ritchie, M. J. Buehler, and P. Hansma, "Plasticity and toughness in bone," *Physics Today*, vol. 62, no. 6, pp. 41–47, 2009, doi: 10.1063/1.3156332.

[3] J. D. Currey, *Bones: Structure and Mechanics*. Princeton University Press, 2002.

[4] E. E. Wilson, A. Awonusi, M. D. Morris, D. H. Kohn, M. M. J. Tecklenburg, and L. W. Beck, "Three structural roles for water in bone observed by solid-state NMR," *Biophysical Journal*, vol. 90, no. 10, pp. 3722–3731, 2006, doi: 10.1529/biophysj.105.070243.

[5] J. S. Nyman, Q. Ni, D. P. Nicolella, and X. Wang, "Measurements of mobile and bound water by nuclear magnetic resonance correlate with mechanical properties of bone," *Bone*, vol. 42, no. 1, pp. 193–199, Jan. 2008, doi: 10.1016/j.bone.2007.09.049.

[6] R. A. Horch, J. S. Nyman, D. F. Gochberg, R. D. Dortch, and M. D. Does, "Characterization of1H NMR signal in human cortical bone for magnetic resonance imaging," *Magnetic Resonance in Medicine*, vol. 64, no. 3, pp. 680–687, Sep. 2010, doi: 10.1002/mrm.22459.

[7] R. A. Horch, D. F. Gochberg, J. S. Nyman, and M. D. Does, "Clinically compatible MRI strategies for discriminating bound and pore water in cortical bone," *Magnetic Resonance in Medicine*, vol. 68, no. 6, pp. 1774–1784, Dec. 2012, doi: 10.1002/mrm.24186.

[8] M. Granke, M. D. Does, and J. S. Nyman, "The Role of Water Compartments in the Material Properties of Cortical Bone," *Calcified Tissue International*, vol. 97, no. 3. Springer New York LLC, pp. 292–307, Sep. 06, 2015. doi: 10.1007/s00223-015-9977-5.

[9] J. Samuel, J. S. Park, J. Almer, and X. Wang, "Effect of water on nanomechanics of bone is different between tension and compression," *Journal of the Mechanical Behavior of Biomedical Materials*, vol. 57, pp. 128–138, Apr. 2016, doi: 10.1016/j.jmbbm.2015.12.001.

[10] P. Fratzl, *Collagen*. Boston, MA: Springer US, 2008. doi: 10.1007/978-0-387-73906-9.

[11] E. Khor, "Methods for the treatment of collagenous tissues for bioprostheses," 1997.

[12] Y. Alania, J. Creighton, L. T. Trevelin, C. A. Zamperini, and A. K. Bedran-Russo, "Regional contribution of proteoglycans to the fracture toughness of the dentin extracellular matrix," *Journal of Biomechanics*, vol. 101, p. 109633, 2020.

[13] R. K. Nalla, J. J. Kruzic, J. H. Kinney, M. Balooch, J. W. Ager, and R. O. Ritchie, "Role of microstructure in the aging-related deterioration of the toughness of human cortical bone," *Materials Science and Engineering C*, vol. 26, no. 8, pp. 1251–1260, Sep. 2006, doi: 10.1016/j.msec.2005.08.021.

[14] G. Boivin and P. J. Meunier, “The degree of mineralization of bone tissue measured by computerized quantitative contact microradiography,” *Calcified Tissue International*, vol. 70, no. 6, pp. 503–511, Jun. 2002, doi: 10.1007/s00223-001-2048-0.

[15] M. R. Hardisty, T. C. Garcia, S. Choy, J. Dahmubed, S. M. Stover, and D. P. Fyhrie, “Stress-whitening occurs in demineralized bone,” *Bone*, vol. 57, no. 2, pp. 367–374, Dec. 2013, doi: 10.1016/j.bone.2013.08.029.

[16] P. J. Thurner *et al.*, “The effect of NaF in vitro on the mechanical and material properties of trabecular and cortical bone,” *Advanced Materials*, vol. 21, no. 4, pp. 451–457, Jan. 2009, doi: 10.1002/adma.200801204.

[17] A. Dasari, J. Rohrmann, and R. D. K. Misra, “Microstructural aspects of surface deformation processes and fracture of tensile strained high isotactic polypropylene,” *Materials Science and Engineering A*, vol. 358, no. 1–2, pp. 372–383, Oct. 2003, doi: 10.1016/S0921-5093(03)00331-9.

[18] M. R. Hardisty, M. A. Soicher, T. C. Garcia, S. M. Stover, and D. P. Fyhrie, “Do stress-whitening and optical clearing of collagenous tissue occur by the same mechanism?,” *Journal of Biomechanics*, vol. 46, no. 14, pp. 2411–2418, Sep. 2013, doi: 10.1016/j.jbiomech.2013.07.026.

[19] J. S. Temenoff and A. G. Mikos, “Polymer Crazing,” in *Biomaterials: The Intersection of Biology and Material Science*, Pearson Education, Inc., 2008, p. 164.

[20] H.-J. Sue and A. F. Yee, “Toughening mechanisms in a multi-phase alloy of nylon 6,6/polyphenylene oxide,” *JOURNAL OF MATERIALS SCIENCE*, vol. 24, pp. 1447–1457, 1989.

[21] C. G. Rylander *et al.*, “Dehydration mechanism of optical clearing in tissue,” *Journal of Biomedical Optics*, vol. 11, no. 4, p. 041117, 2006, doi: 10.1117/1.2343208.

[22] M. R. Hardisty, D. F. Kienle, T. L. Kuhl, S. M. Stover, and D. P. Fyhrie, “Strain-induced optical changes in demineralized bone,” *Journal of Biomedical Optics*, vol. 19, no. 3, p. 035001, Mar. 2014, doi: 10.1117/1.jbo.19.3.035001.

[23] M. D. Shoulders and R. T. Raines, “Collagen Structure and Stability,” *Annual Review of Biochemistry*, vol. 78, no. 1, pp. 929–958, Jun. 2009, doi: 10.1146/annurev.biochem.77.032207.120833.

[24] D. H. Pashley, K. A. Agee, R. M. Carvalho, K.-W. Lee, F. R. Tay, and T. E. Callison, “Effects of water and water-free polar solvents on the tensile properties of demineralized dentin.” [Online]. Available: www.elsevier.com/locate/dental

[25] A. K. Bembey, A. J. Bushby, A. Boyde, V. L. Ferguson, and M. L. Oyen, “Hydration effects on the micro-mechanical properties of bone,” *Journal of Materials Research*, vol. 21, no. 8, pp. 1962–1968, Aug. 2006, doi: 10.1557/jmr.2006.0237.

[26] R. K. Nalla, M. Balooch, J. W. Ager, J. J. Kruzic, J. H. Kinney, and R. O. Ritchie, “Effects of polar solvents on the fracture resistance of dentin: Role of water hydration,” *Acta Biomaterialia*, vol. 1, no. 1, pp. 31–43, Jan. 2005, doi: 10.1016/j.actbio.2004.08.002.

[27] Janet H. Clark, “Reversible Crystallization In Tendons and Its Functional Significance,” 1928. doi: 10.1073/pnas.14.7.526.

[28] P. Benetatos, A. von der Heydt, and A. Zippelius, “Tension-induced binding of semiflexible biopolymers,” *New Journal of Physics*, vol. 16, Nov. 2014, doi: 10.1088/1367-2630/16/11/113037.

[29] A. v. Subbotin and A. N. Semenov, “Phase Separation in Polymer Solutions under Extension,” *Polymer Science - Series C*, vol. 60, pp. 106–117, Dec. 2018, doi: 10.1134/S1811238218020200.

[30] K. Binder, “Theory of first-order phase transitions,” 1987.

[31] C. A. Miles and M. Ghelashvili, “Polymer-in-a-box mechanism for the thermal stabilization of collagen molecules in fibers,” *Biophysical Journal*, vol. 76, no. 6, pp. 3243–3252, 1999, doi: 10.1016/S0006-3495(99)77476-X.

[32] A. Ghanaeian and R. Soheilifard, “Comparative analysis of the viscoelastic properties of collagen-like proteins by virtual creep test,” *Journal of Biomolecular Structure and Dynamics*, 2020, doi: 10.1080/07391102.2020.1753578.

[33] H. Trębacz and K. Wójtowicz, “Thermal stabilization of collagen molecules in bone tissue,” *International Journal of Biological Macromolecules*, vol. 37, no. 5, pp. 257–262, Dec. 2005, doi: 10.1016/j.ijbiomac.2005.04.007.

[34] S. Leikin, V. A. Parsegian, W.-H. Yang, and G. E. Walrafen, “Raman spectral evidence for hydration forces between collagen triple helices,” 1997. [Online]. Available: www.pnas.org.

[35] O. G. Andriotis, S. Desissaire, and P. J. Thurner, “Collagen Fibrils: Nature’s Highly Tunable Nonlinear Springs,” *ACS Nano*, vol. 12, no. 4, pp. 3671–3680, Apr. 2018, doi: 10.1021/acsnano.8b00837.

[36] Y. Song *et al.*, “Visualization of Penetration and Reaction of Aldehyde Tanning Agent in Leather using Fluorescence Technique,” *Journal of the American Leather Chemists Association*, vol. 115, no. 7, pp. 248–254, 2020.

[37] T. Covington, “Mineral Tanning: Chromium(iii),” in *Tanning Chemistry: The Science of Leather*, The Royal Society of Chemistry, 2009, pp. 204–258.

[38] A. Bigi, G. Cojazzi, S. Panzavolta, K. Rubini, and N. Roveri, “Mechanical and thermal properties of gelatin films at different degrees of glutaraldehyde crosslinking,” 2001.

[39] A. Ripamonti, N. Roveri, D. Braga, D. J. S. Hulmes, A. Miller, and P. A. Timmins, “Effects of pH and ionic strength on the structure of collagen fibrils,” *Biopolymers*, vol. 19, no. 5, pp. 965–975, 1980, doi: 10.1002/bip.1980.360190503.

[40] Y. P. Dick and A. Nordwig, “Effect of pH on the stability of the collagen fold,” *Archives of Biochemistry and Biophysics*, vol. 117, pp. 466–468, 1966.

[41] C. A. Grant, D. J. Brockwell, S. E. Radford, and N. H. Thomson, “Tuning the elastic modulus of hydrated collagen fibrils,” *Biophysical Journal*, vol. 97, no. 11, pp. 2985–2992, Dec. 2009, doi: 10.1016/j.bpj.2009.09.010.

[42] S. Leikin, D. C. Rau, and V. A. Parsegian, “Temperature-favoured assembly of collagen is driven by hydrophilic not hydrophobic interactions,” *Structural Biology*, vol. 2, no. 3, pp. 205–210, Jan. 1995, [Online]. Available: http://www.nature.com/nsmb

[43] M. J. Pelletier and C. C. Pelletier, “Spectroscopic Theory for Chemical Imaging,” in *Raman, Infrared, and Near-Infrared Chemical Imaging*, S. Sˇasˇic and Y. Ozaki, Eds. John Wiley & Sons, Inc., 2010, pp. 1–20.

[44] M. Navas-Moreno and J. W. Chan, “Laser tweezers Raman microspectroscopy of single cells and biological particles,” in *Methods in Molecular Biology*, vol. 1745, Humana Press Inc., 2018, pp. 219–257. doi: 10.1007/978-1-4939-7680-5_13.

[45] S. Schlücker, M. D. Schaeberle, S. W. Huffman, and I. W. Levin, “Raman microspectroscopy: A comparison of point, line, and wide-field imaging methodologies,” *Analytical Chemistry*, vol. 75, no. 16, pp. 4312–4318, Aug. 2003, doi: 10.1021/ac034169h.

[46] G. E. Walrafen and Y.-C. Chu, “Nature of collagen-water hydration forces: a problem in water structure,” *Chemical Physics*, vol. 258, no. 2–3, pp. 427–446, 2000, doi: 10.1016/S0301-0104(00)00072-0.

[47] J. J. Katz, “Chemical and Biological Studies with Deuterium,” *American Scientist*, vol. 48, no. 4, pp. 544–580, 1960, [Online]. Available: https://www.jstor.org/stable/27827650

[48] M. Unal, S. Yang, and O. Akkus, “Molecular spectroscopic identification of the water compartments in bone,” *Bone*, vol. 67, pp. 228–236, 2014, doi: 10.1016/j.bone.2014.07.021.

[49] M. Jastrzebska, R. Wrzalik, A. Kocot, J. Zalewska-Rejdak, and B. Cwalina, “Hydration of glutaraldehyde-fixed pericardium tissue: Raman spectroscopic study,” *Journal of Raman Spectroscopy*, vol. 34, no. 6, pp. 424–431, Jun. 2003, doi: 10.1002/jrs.1016.

[50] A. Gautieri, S. Vesentini, A. Redaelli, and M. J. Buehler, “Osteogenesis imperfecta mutations lead to local tropocollagen unfolding and disruption of H-bond network,” *RSC Advances*, vol. 2, no. 9, pp. 3890–3896, Apr. 2012, doi: 10.1039/c2ra01047j.

Chapter 2: Equipment Characterization

2.1 Mechanical Tester

A micromechanical tester was designed to fit on the stage of an inverted confocal scanning upright microscope for simultaneous Raman imaging (Figure 2.1; ADMET, Norwood, MA, USA). The system was also designed to be easily assembled and disassembled for portability (see Appendix A4 for CAD drawings and detailed assembly instructions). The mechanical tester has a maximum load of 1,000 N, a stroke of 12 mm, and a maximum displacement rate of 25 mm/min. The motorized tensile tester utilizes a dual moving crosshead system which keeps the center of the specimen stationary to enable investigation of the region of interest over the entire period of deformation, regardless of strain. The mechanical tester includes a heated fluid bath for temperature-controlled testing in a wet environment. An adjustable optical viewport which sits directly below the specimen allows for simultaneous Raman spectroscopy measurements during mechanical testing. Additionally, the micromechanical tester can be mounted on a stand for use independent from a microscope.

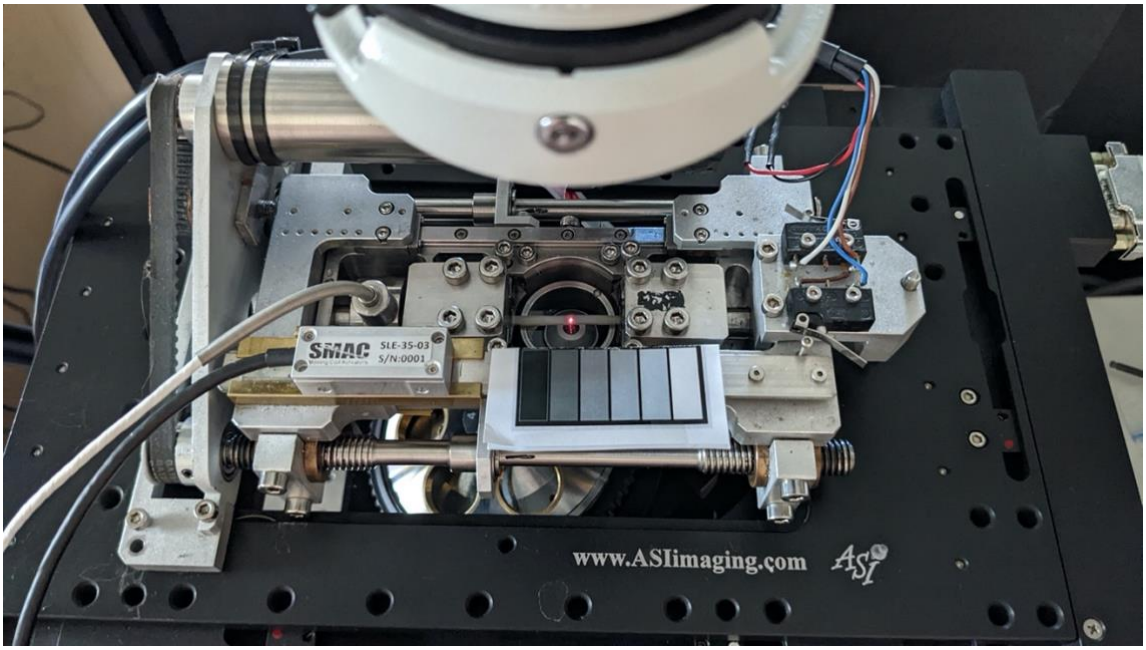

Figure 2.1: The custom micromechanical tester (ADMET, Norwood, MA, USA) mounted on the platform of the inverted confocal Raman microscope.

2.1.1 Setup

The first step of this project was to assemble the micromechanical tester and to characterize its operation. The electronic cables are clearly marked, and the CAD drawings of the device were sufficient for explaining the assembly. Barriers to set-up included an essential cable that was missing from the initial shipment, a weak solder that broke during transport, and a disrupted electrical connection in the position encoder that was tricky to diagnose. Once these barriers were addressed, the system became very simple to operate. Appendix A9 details the troubleshooting that occurred during characterization of the machine and general tips and tricks for future students who plan to use the equipment.

2.1.2 Compatibility with the Raman System

The micromechanical tester interfaces with the custom-built inverted Raman scanning confocal microscope in Dr. Randy Carney's laboratory. To mount the micromechanical tester on the microscope stage, the microscope's condenser must be removed. Additionally, of the two

microscope objectives available for use (20x and 60x), only the 20x objective has a small enough diameter to operate within the optical viewport of the mechanical tester (Sheet 2 of the CAD drawings in Appendix A4 provides a visual of the lens clearance within the optical viewport). Fortunately, the 20x objective facilitated better quality Raman data of demineralized bone than the 60x objective, based on initial measurements of demineralized bone. Therefore, the size limitation of the 60x objective did not hinder the collection of Raman data for this research project. Appendix A8 details the experimental protocol used to facilitate compatibility of the Raman and mechanical test systems for successful experiments.

2.1.3 General Troubleshooting

Once the mechanical tester was assembled, initial training took place, led by the ADMET's technical support member, on the operation of the control software (MTESTQuattro, ADMET, Norwood, MA, USA). The mechanical testing protocol was learned via trial and error. Throughout the process there were multiple protocol errors. For example, "position limit/overrange errors" occurred, which can be corrected by manually adjusting the grip separation to "clear" the position error.

2.1.4 Troubleshooting Strain Errors

Initial mechanical tests on demineralized bone specimens had unexpected trends in the strain data which were inconsistent with typical bone mechanical properties. For example, unrealistic strain creep was evident in the data collected during position-controlled tests. Moreover, the strain values were not being calculated correctly by the MTESTQuattro software, which became apparent when analyzing the strain channel output of position-controlled tests. ADMET's technical support believed the strain-creeping problem could be attributed to backlash in the position system and suggested that tension should be applied to the crossheads in the form

of rubber bands. To confirm if this was the issue, multiple tests were completed with varying amounts of rubber bands on the crossheads. None of these results showed improvement in the system backlash.

Ultimately the strain-creep issue was attributed to poor labeling of output channels in the MTESTQuattro software. Both the “strain” and “position” output channels in the MTESTQuattro software record displacement of the mechanical tester grips. More specifically, the “strain” output recorded by the mechanical tester is a direct measurement of position measured by an optical position transducer, whereas the “position” output is measured indirectly by a rotation encoder on the motor. Therefore, the device has two separate displacement channels, one of which is called “position” and one is called “strain.” Because the “strain” channel is measured by the optical position transducer attached to the moving portion of the loader, it is a more accurate measure of grip displacement than the “position” channel. As a result, the strain channel is more accurate to program a “strain”-controlled mechanical test protocol than a “position”-controlled test. All mechanical test protocols were thus “strain”-controlled (that is, displacement controlled using the channel “strain” as named by the manufacturer), thus ameliorating the strain-creep issue.

2.1.5 Troubleshooting Load Errors

The load output recorded by the MTESTQuattro software was incorrect; the load data was generally very noisy and featured strong load peaks during a zero-load testing procedure (i.e., load-peaks occurred when there was no displacement, and therefore no load applied to the specimen). Initially the severe noise and incorrect load peaks were thought to be electrical noise from the surrounding environment. To test this, the testing system was assembled on a wheeled cart and moved it to six different locations within the laboratory building and repeated the same

zero-load testing procedure. The load errors persisted regardless of environment. Attempts to ground the system with a ground wire also did not solve the issue.

The peaks in the load data during a zero-load procedure were consistent and predictable, and occurred when the temperature of the system was increasing. Therefore, tests were completed to assess if peaks in the load data could be attributed to electrical interference from fluid bath heaters during heating. To fix this, Kapton tape (a polyimide film which acts as a thermally conductive electrical insulator) was applied between the fluid bath heaters and the mechanical tester. This eliminated severe noise in the data, but the peaks in the load data caused by interference between the fluid bath heaters and load cell remained present. The issue remained unsolved, as there was an error of ~0.5 N/^{o}C present in the data after the application of the Kapton tape.

On another note, a few months later it became apparent that the load cell had become loose and was rotating axially, contributing to some of the errors in the load measurements. This issue was easily fixed by tightening the load cell piston screw.

Even after applying the Kapton tape to reduce the noise in the data and tightening the load cell to prevent axial rotation, the load profile from ramp-and-hold "strain"-controlled protocols of demineralized bone did not conform to what was expected based on previous literature reports. In the literature, the force-displacement curves of demineralized bone are characterized by an initial nonlinear toe region followed by a linear behavior at higher displacements [1]–[3]. Instead, the output of the micromechanical tester showed a steep slope in the first ~0.07 mm of displacement followed by a region of low force per displacement until the end of test (Figure 2.2).

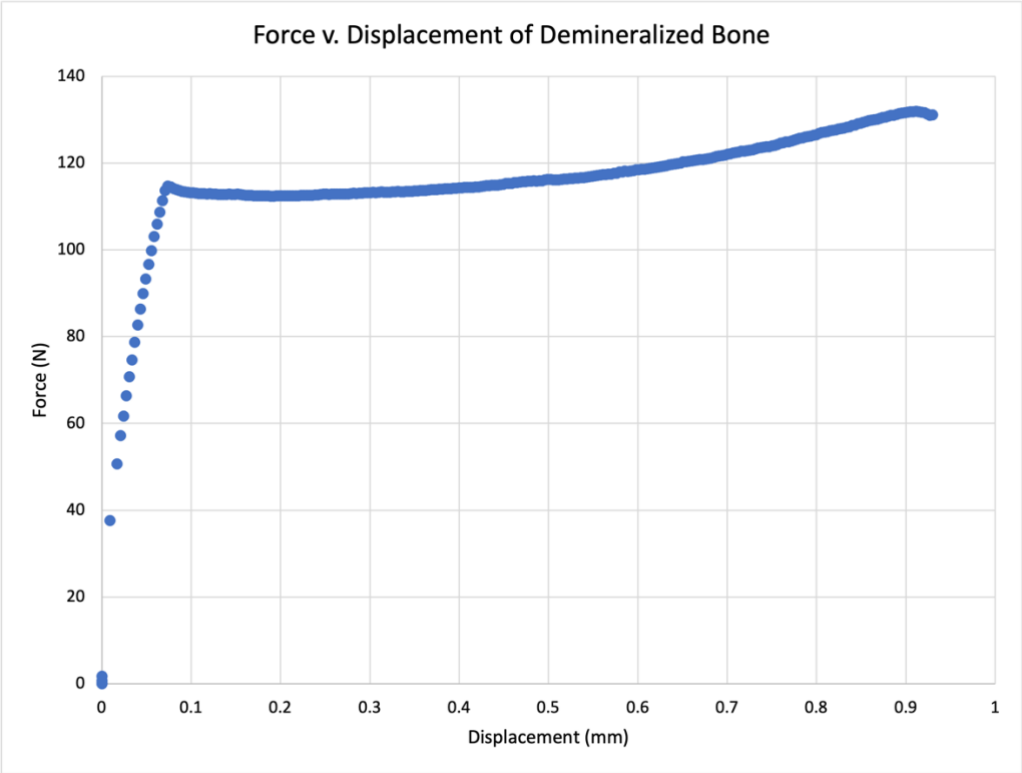

Figure 2.2: Representative force-displacement curve of demineralized equine cortical bone collected by the ADMET micromechanical tester.

To further assess if the load-errors were due to the mechanical testing system, a ramp up – hold – ramp down test was performed with a ball-point pen spring (linear spring) held by the mechanical tester under strain-control. The spring ends set in PMMA to make it easier to grip. The recorded data did not follow a typical linear-spring force-displacement profile. The load data increased linearly at the beginning and then began to plateau before the "hold," indicating that there was some sort of friction force present in the beginning of the test. These results indicated that, due to the design of the mechanical tester, there is frictional interference between the left grip and the load frame, causing the errors in the load measurements. The mechanical tester was designed with a tight fit between the load frame and the grips to keep fluid in the fluid bath between the grips where the specimen is secured. Unfortunately, this design causes issues in the

load data and affected the load measurements recorded in the load channel of the MTESTQuattro software.

Unfortunately, there was not enough time to fix this issue prior to the final data collection. Although load data were collected for all the experiments in this thesis, the load data is not presented due to the issues caused by the design flaw in the mechanical tester. Plans to rectify this issue include removing the grips from the load frame and using a CNC machine to sand down the sides of the grips such that they no longer drag against the inside of the load frame.

2.1.6 Tuning the Temperature Controller

To further reduce the interference between the fluid bath heater and the load channel, two possible courses of action were determined: (1) to tune the temperature controller again, such that it held the setpoint temperature more precisely, or (2) to acquire a new load cell that is less sensitive to changes in temperature. Because temperature controller was reaching a ceiling and unable to heat past 29°C, the next step became to tune the temperature controller, with the aim of fixing both the load-temperature interaction and the temperature ceiling problems.

The goal of tuning was to improve the temperature controller's ability to hold the setpoint temperature more precisely. The temperature controller is a PID (i.e., proportional, integral, derivative) controller, meaning it operates as a control feedback loop to regulate temperature. The controller senses an input from the thermocouples attached to the fluid bath, compares the temperature reading to the setpoint, and provides an output to the heating elements to rectify the difference. The proportional, integral, and derivative values can each be changed to achieve the setpoint in different ways. First, autotuning the temperature controller was attempted using the hardware's internal autotune feature. Unfortunately, the autotune feature was unsuccessful at

correctly tuning the PID values to hold the temperature setpoint with precision. Second, manual tuning the PID's integral values using a trial-and-error approach was attempted. The integral value was selected because it controls the comparison to steady-state error. The manufacturer-set integral value was 2520 (the maximum being 3999). The manual tuning process started by halving the pre-set value (i.e., "I" = 1260) and collecting 90 minutes of both heating and non-heating data (since the controller cannot directly cool the system). This procedure was repeated with different integral values (i.e., 0, 630, 1000, 1260, and 1890) and compared the heating data to see which value produced the optimal temperature response. None of the data showed ideal temperature response so we chose to approach the PID tuning in another manner [4] which is outlined here:

1. Set the Integral and Derivative values to 0.
2. Increase the Proportional value until the output of the loop oscillates.
3. Once the Proportional value provides the desired fast response, increase the Integral value to stop the oscillations and minimize the steady state error.
4. Increase the Derivative value until the loop increases acceptably quickly to the setpoint.

Attempting this method, the temperature controller was still unable to achieve the desired results of the temperature reaching and holding the programmed setpoint. Therefore, autotuning the controller was attempted one last time using the hardware's autotune feature, which ran for almost 48 hours without success before the process was aborted.

ADMET technical support indicated that autotune process should not take so long (>48 hours), indicating that there was potentially something broken within the temperature controller. Since the heating elements were not fully contacting the frame of the mechanical tester, it is

possible that nothing was absorbing the heat created by the heating elements and thus the heating elements “burnt up” and can no longer function. There was not enough time to fix this issue before the final data collection for this thesis. Moreover, much later it became apparent that a ground wire for one of the fluid bath heaters had become completely disconnected. Likely the process of transporting the system between laboratories multiple times caused the electrical connections to loosen. Perhaps the loosened electrical connections caused a short the system and damaged the temperature controller box, resulting in the described issues. Temperature control remains inoperable, and we are working with the company to replace the broken components of the temperature control system.

2.2 Raman Spectroscopy System

After confirming that the mechanical tester was compatible with the Raman microscope in the Carney Lab, the next step was to determine if the Raman spectroscopic system could provide clean spectral data for our bone specimens. The custom-built inverted Raman scanning confocal microscope is an ultra-fast laser-scanning microscope equipped with a detection system based on the Andor Kymera-3281-C spectrophotometer and Newton DU920P-BR-DD CCD camera. The detection system is coupled into an inverted IX73 Olympus microscope designed to have a lateral resolution of 350 nm and an axial resolution of 550 nm (i.e., diffraction-limited spatial resolution) when using a 785 nm excitation laser. The instrument is controlled using custom LabVIEW software (Carney Lab, UC Davis). Spectra were acquired using this Raman microscope with an excitation wavelength of 785 nm and processed using Solis v4.31.30005.0 software. A laser power of 67 mW (measured just prior to the objective) was used for all demineralized bone specimens.

To begin characterizing the Raman microscope for the purposes of these experiments, measurements were taken of the major constituent chemicals of this project including water, deuterium oxide, demineralized bone, and deuterated demineralized bone. The following sections outline the results of experiments which determined the optimal specifications for collecting Raman spectral data of the different constituents.

It is important to note that due to the autofluorescence of glass at infrared wavelengths, a quartz coverslip must be used when collecting Raman data to avoid auto-fluorescent peaks in the data caused by a glass coverslip. Specifically for demineralized bone, the autofluorescence caused by glass will mask the amide I, CH_2, and amide III peaks of the spectrum (1200-1800 cm^{-1}) (Figure 2.3).

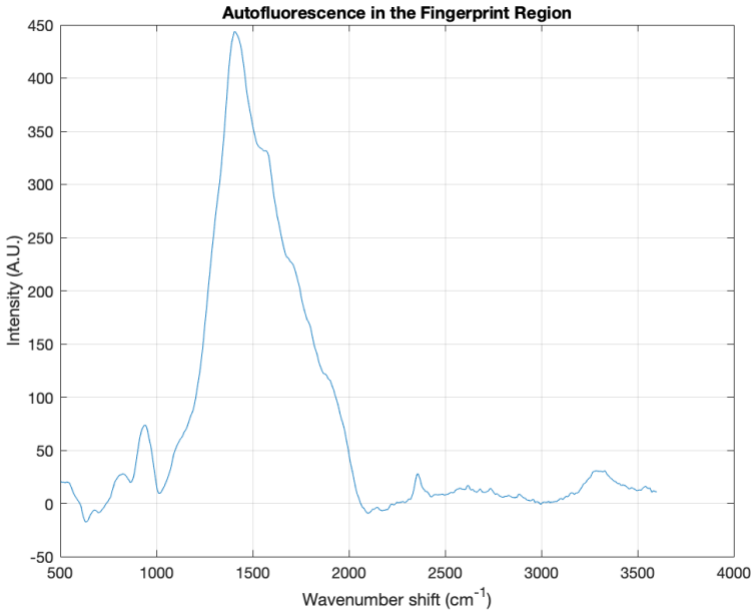

Figure 2.3: Autofluorescence in the fingerprint region of a Raman spectra of demineralized bone, caused by using a typical glass coverslip.

Some technical terms will be used in the following sections which relate to the parameters of Raman data collection. Those terms are defined here to supplement the reader's understanding. *Kinetic series* are Raman spectral measurements that are taken sequentially and

stored as a series within a dataset. *Accumulations* are Raman spectral measurements that are taken sequentially and summed together as one dataset. *Throughput* (i.e., aperture) is the size of the pinhole which controls the amount of Raman signal that passes onto the detector. *Exposure time* is the amount of time that the CCD camera is actively collecting Raman measurements.

2.2.1 Water (H_2O)

Pure water was the first major constituent we measured as a reference standard and was the most difficult chemical to measure with the Raman optical setup. Due to the characteristics of the 785 nm laser, the OH-stretch region of the Raman spectrum (~3000-3600 cm^{-1}) falls in the near infrared region, causing the intensity of the water signal to be extremely low and noisy. Therefore, we worked on increasing the signal-to-noise ratio (SNR) to measure appreciable signal. After maximizing the laser power at 67 mW (which was not found to damage, i.e., burn, the demineralized bone specimens), throughput and exposure time were adjusted to increase the SNR. Raman measurements were collected at varying values and combinations of throughput and exposure time to determine the optimal values for each parameter. Throughput ratios of 50/50, 75/25, and 100/0 were used to collect Raman measurements. Ultimately a value of 100% throughput was chosen, which enabled the most optimized intensity of the broad water peaks in the ~3000-3600 cm^{-1} region (Figure 2.4). Exposure times (10, 30, 60, and 90 sec) were assessed. Each measurement was collected with three accumulations of the exposure time. The results showed that 60-90 seconds was optimal for increased SNR.

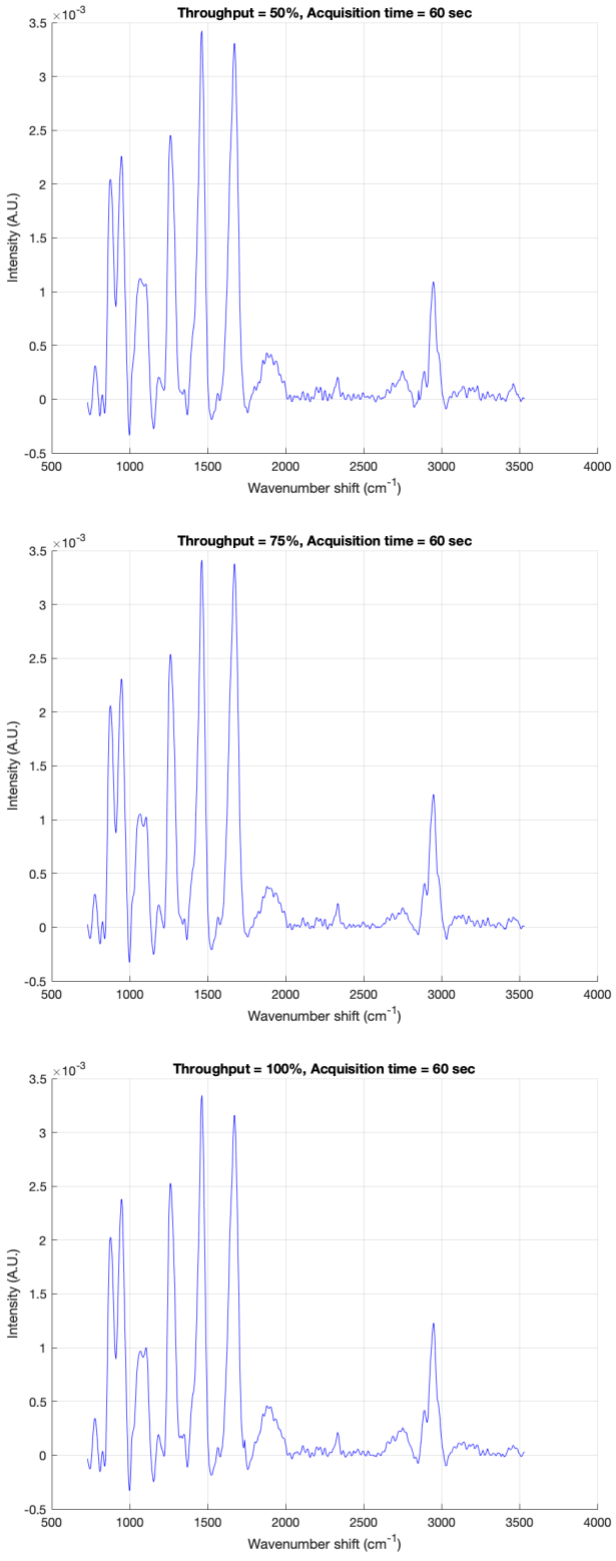

Figure 2.4: Raman spectral results from optimizing the SNR. **Top:** throughput = 50% and exposure = 60 sec. **Middle:** throughput = 75% and exposure = 60 sec. **Bottom:** throughput = 100% and exposure = 60 sec.

2.2.2 Deuterium Oxide (D_2O)

Raman measurements of pure deuterium oxide (D_2O) (99.9% isotopic purity, Sigma-Aldrich, St. Louis, MO, USA) were taken as a reference standard to characterize the Raman OD-band. The goal of collecting this data was to ensure that the system can collect quality measurements of D_2O, which were intended to be used to track the movement of water in the collagenous matrix of demineralized bone under tension. The Raman spectrum of deuterium oxide is characterized by a broad peak at ~2200-2800 cm^{-1} with shoulders at ~2400 cm^{-1} and ~2500 cm^{-1}. Figure 2.5 is a representative picture of the Raman spectrum of deuterium oxide that we collected.

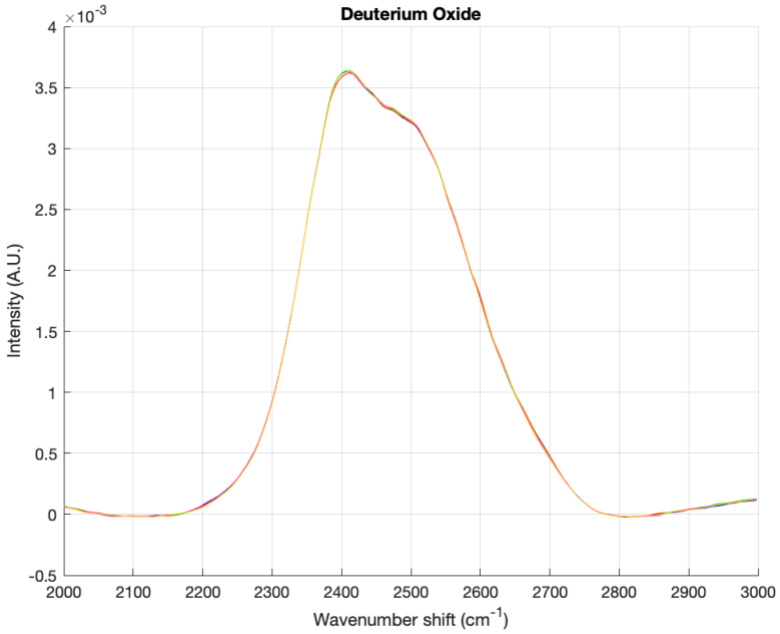

Figure 2.5: Raman spectral data of pure deuterium oxide in the wavenumber range ~2200-2800 cm^{-1} (Acquisition settings: objective = 20x; power = 67 mW; kinetic series length = 5; acquisition time = 10 seconds). The characteristic shoulders are found at ~2410 cm^{-1} and ~2500 cm^{-1}.

Additionally, Raman data was collected to compare the relative intensities of the D_2O and H_2O Raman peaks, including measurements of mixtures of D_2O and H_2O of varying concentrations. The results of this are shown in Figure 2.6.

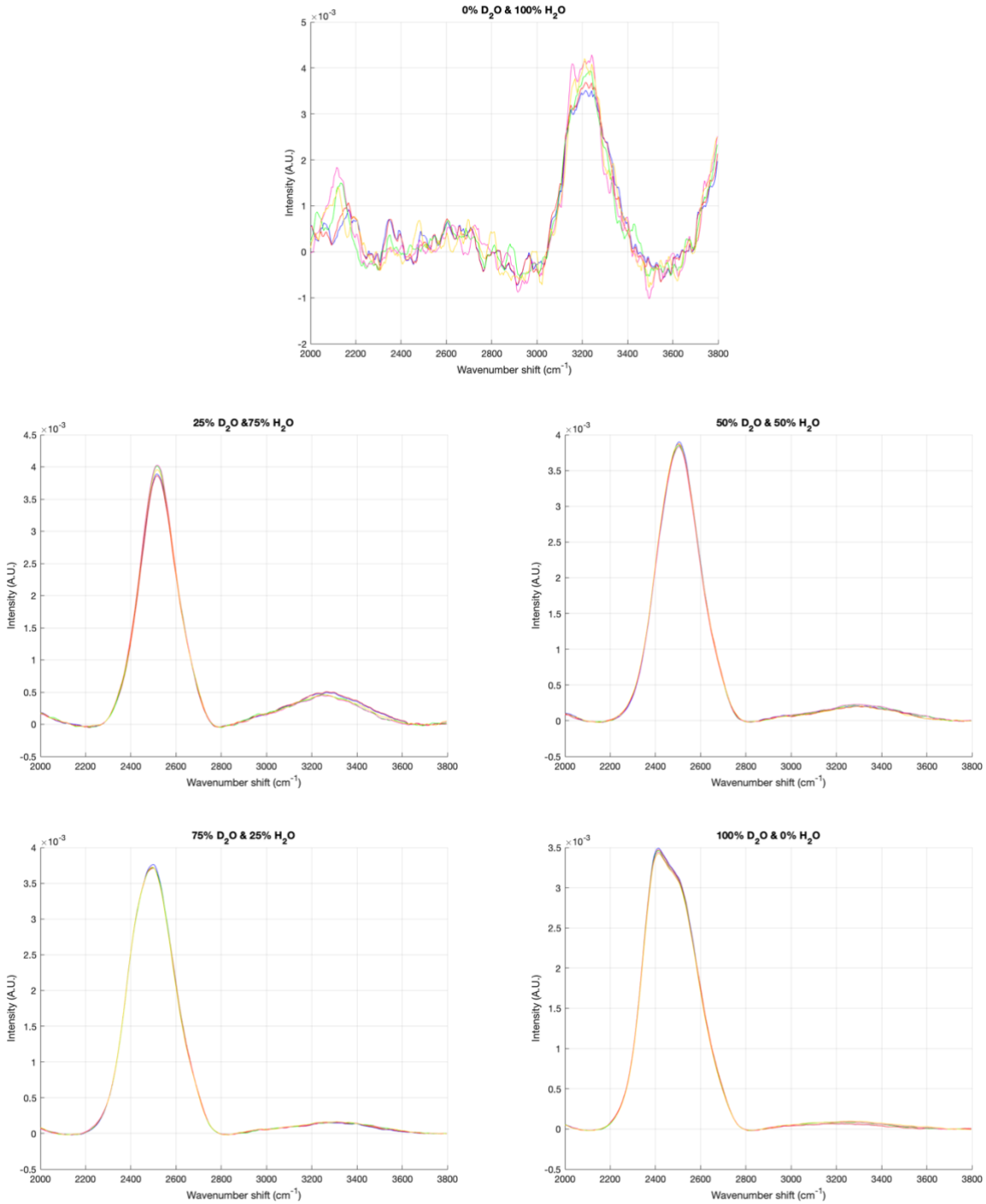

Figure 2.6: Raman spectra of mixtures containing varying concentrations of deuterium oxide and water. **Row 1:** 0% D_2O and 100% H_2O. **Row 2:** 25% D_2O and 75% H_2O (left); 50% D_2O and 50% H_2O (right). **Row 3:** 75% D_2O and 25% H_2O (left); 100% D_2O and 0% H_2O (right).

2.2.3 Demineralized Bone

Ultimately the aim of this project is to quantify changes in the Raman signal of demineralized bone under tension, thus it was important to collect baseline measurements of demineralized bone under no mechanical load. Figure 2.7 is representative of the demineralized bone measurements; the characteristic peaks of demineralized bone are marked on the figure (Table 2.1 includes Raman peak assignments of bone based on a literature review [2-5]).

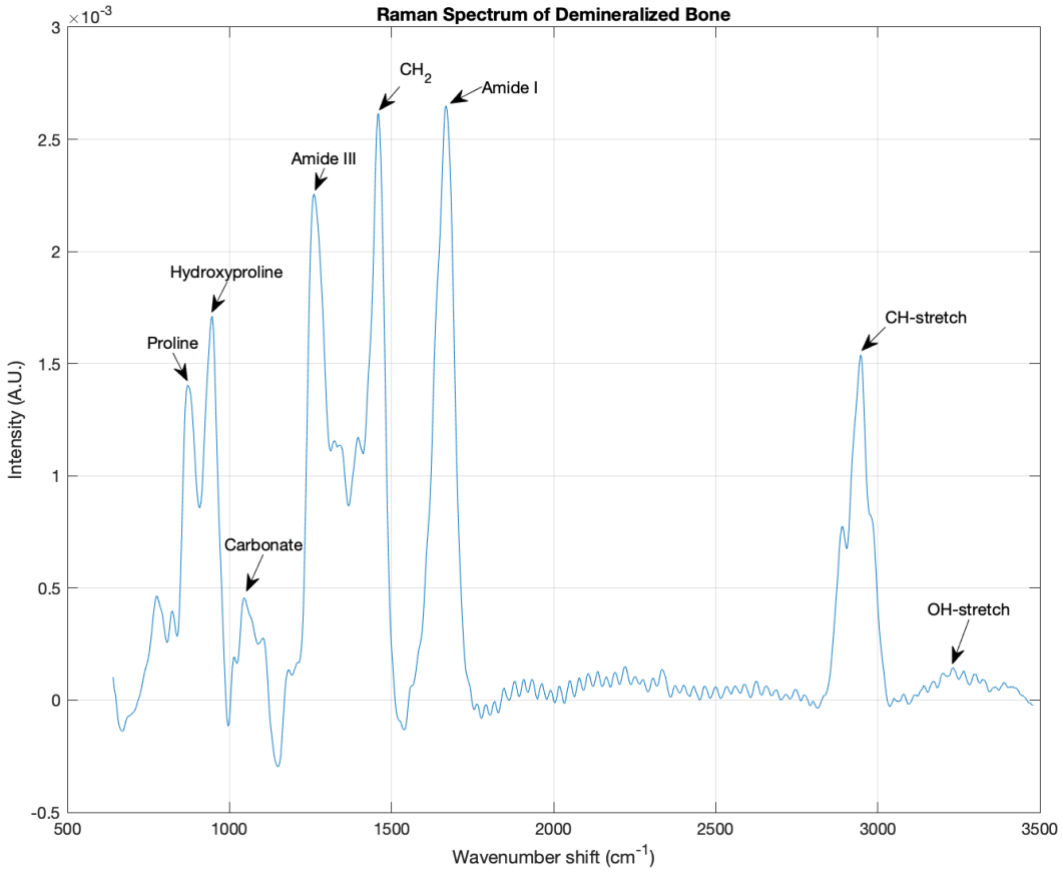

Figure 2.7: Average Raman spectral data of demineralized bone with the major peaks indicated. (Acquisition settings: objective = 20x; power = 67 mW; kinetic series length = 30; acquisition time = 10 seconds).

Table 2.1: Approximate Raman peak assignments of major constituents of bone, based on a literature review.

Wavenumbers reported in the literature (cm^{-1})	**Morris and Mandair (2011)** [5]	**Shah (2020)** [6]	**Timchenko et. al. (2019)** [7]	**Timchenko et. al. (2015)** [8]
Phosphate (secondary)	-	380-410	-	580
Phosphate (primary)	959	957-962	956	-
Proline	921& 855	830 - 890	850	855
Hydroxyproline	876	830 - 890	875	876
Phenylalanine	1002	1004 & 1033	1001 &1026	1001-1003
Carbonate	1070	-	1068-1100	1065-1070
Amide III	1243-1320	-	1230-1280	1245-1270
CH_2	1450	-	-	1445
Amide II	-	-	1555-1585	-
Amide I	1616-1720	-	1655-1675	1665
CH-stretch	2940	2950	-	-

2.2.4 Deuterated Demineralized Bone

A hydrogen/deuterium (H/D) exchange was used to exchange the hydrogen atoms within the collagenous phase with deuterium atoms (i.e., exchanging water with heavy water) to increase the intensity and ease of tracking water movement caused by tensile loading (see Appendix A3 for deuteration protocol). Since the water signal collected with the 785 nm laser is so low and noisy, it is crucial to conduct an H/D exchange to measure the effects of tension on the movement of water in the demineralized bone specimens.

Raman measurements of deuterated demineralized bone under no mechanical load were collected as baseline measurements for comparison with loaded data. As expected, the Raman spectrum of deuterated demineralized bone shows the characteristic peaks of both deuterium oxide and demineralized bone, as shown in Figure 2.8.

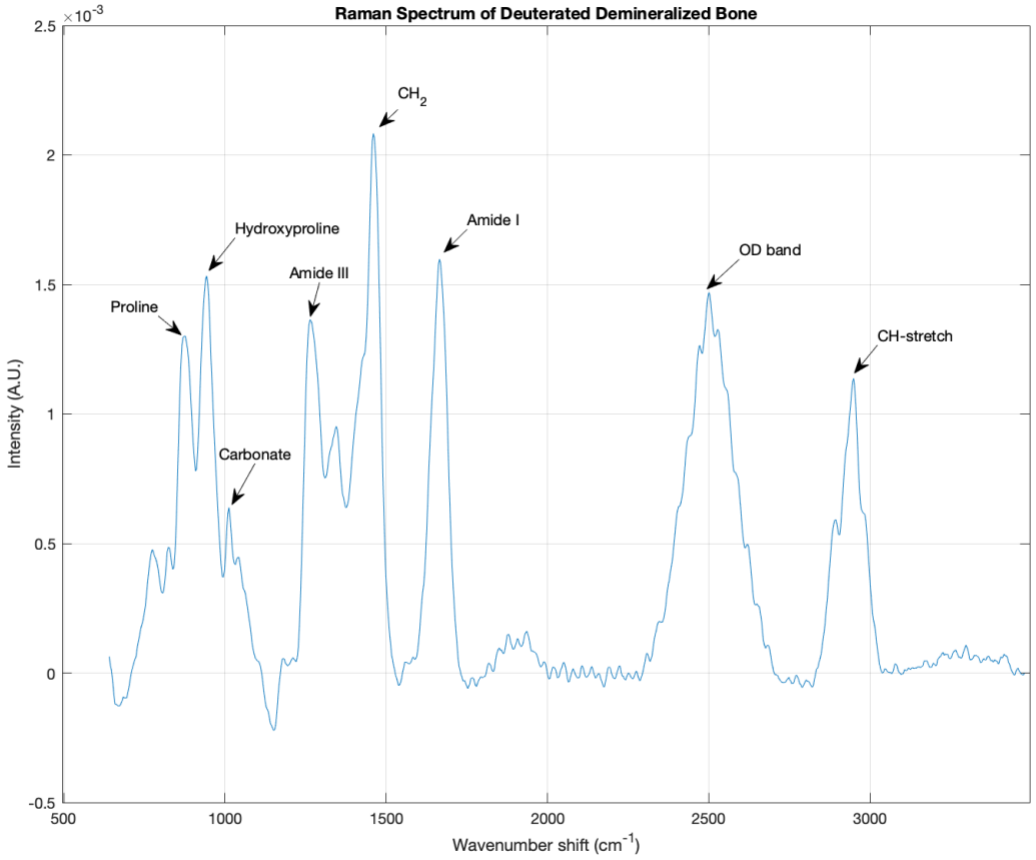

Figure 2.8: Average Raman spectral data of deuterated demineralized bone with major peaks indicated. The OD-band resulting from the H/D exchange is present between ~2,200 – 2,800 cm^{-1}. (Acquisition settings: objective = 20x; power = 67 mW; kinetic series length = 10; acquisition time = 10 seconds.)

2.3 Characterization Experiments

2.3.1 Determining The Yield Strain of Demineralized Bone

Experiments were conducted to confirm stress-whitening and to identify the yield strain of demineralized bone specimens loaded in tension. Demineralized bone specimens (n=2) were mounted with the mineralized ends of the beams secured in the grips, creating a gauge length of 31 mm. Specimens were loaded in tension at a constant strain rate of 0.07 s^{-1} to a nominal strain of 0.10 (calculated as displacement/31 mm). All tests were performed under "strain"-control, as defined by the MTESTQuattro software.

Synchronized video data (30 fps) was captured during each experiment using a Sony a7R camera (Sony, Tokyo, Japan). All mechanical testing was conducted at 29ºC in a temperature-controlled saline bath. Stress-whitening was observed and captured on video for both specimens.

Both specimens yielded at a nominal strain of ~0.045. This value was determined using the offset method, which involves constructing a line on the stress-strain curve which is parallel to the line of the modulus of elasticity and offset by ~0.2% strain. The intersection of the offset line and the stress-strain curve yields the value of the yield strain. This calculation assumes that the gauge length of the specimen is 31 mm. However, based on a 5 mm demineralized center, a more accurate estimate of the true yield strain is = displacement/5 mm = 0.3.

2.3.2 Determining The Repeatability of Stress-whitening

Now knowing the estimated yield strain of the demineralized bone beam specimens, another set of experiments was conducted to show that stress-whitening can be repeatably observed when specimens are loaded in tension. Specimens (n=2) were mounted with the mineralized ends of the beams secured in the grips, creating a gauge length of 31 mm. Specimens were loaded in tension below failure, at a constant strain rate of 0.001 s^{-1} to a nominal strain of 0.02. This protocol was repeated six times for each specimen. Synchronized video data was captured during each experiment. All mechanical testing was conducted at 29ºC in a temperature-controlled saline bath. Stress-whitening was observed in each test and captured on video.

A final set of experiments was conducted to show that stress-whitening can be repeatably observed when specimens are loaded under tension to a strain of 0.03. The specimen (n=1) was mounted such that the mineralized ends of the beam were secured in the grips, creating a gauge length of 31 mm. The specimen was loaded in tension below failure, at a constant strain rate of

0.001 s^{-1} to a nominal strain of 0.03. After loading, the specimen was unloaded by moving grips to the home position using the MTESTQuattro software. This protocol was repeated three times with no delay between tests. Synchronized video data was captured during each experiment. All mechanical testing was conducted at 29ºC in a temperature-controlled saline bath. Stress-whitening was observed in each test and captured on video.

2.4 Summary

This chapter outlined the work completed to characterize the mechanical testing and the Raman spectroscopy systems used for the data collection of this thesis. Furthermore, experiments were described which were completed to confirm the observation of stress-whitening in demineralized equine bone. The next chapter details the preliminary experiments conducted to measure the effect of stress-induced changes on the Raman spectrum of deuterated, demineralized equine bone undergoing stress-whitening.

References

[1] J. Jonas, J. Burns, E. W. Abel, M. J. Cresswell, J. J. Strain, and C. R. Paterson, "A Technique for the Tensile Testing of Demineralised Bone," *Journal of Biomechanics*, vol. 26, no. 3, pp. 271–276, 1993.

[2] S. M. Bowman, J. Zeind, L. J. Gibson, W. C. Hayes, and T. A. McMahon, "The Tensile Behavior of Demineralized Bovine Cortical Bone," *Journal of Biomechanics*, vol. 29, no. 11, pp. 1497–1501, 1996.

[3] J. Catanese, E. P. Iverson, R. K. Ng, and T. M. Keaveny, "Heterogeneity of the mechanical properties of demineralized bone," *Journal of Biomechanics*, vol. 32, pp. 1365–1369, 1999.

[4] "PID Theory Explained," *ni.com*, Mar. 17, 2020. https://www.ni.com/en-us/innovations/white-papers/06/pid-theory-explained.html (accessed Mar. 09, 2022).

[5] M. D. Morris and G. S. Mandair, "Raman assessment of bone quality," in *Clinical Orthopaedics and Related Research*, 2011, vol. 469, no. 8, pp. 2160–2169. doi: 10.1007/s11999-010-1692-y.

[6] F. A. Shah, "Towards refining Raman spectroscopy-based assessment of bone composition," *Scientific Reports*, vol. 10, no. 1, Dec. 2020, doi: 10.1038/s41598-020-73559-2.

[7] P. E. Timchenko, E. v. Timchenko, L. T. Volova, and O. O. Frolov, "Spectral Analysis of Organic Components of Demineralized Bone Biografts," *Optics and Spectroscopy*, vol. 126, no. 6, pp. 769–775, Jun. 2019, doi: 10.1134/S0030400X19060262.

[8] E. v. Timchenko, P. E. Timchenko, L. A. Taskina, L. T. Volova, M. N. Miljakova, and N. A. Maksimenko, "Using Raman spectroscopy to estimate the demineralization of bone transplants during preparation," *Journal of Optical Technology*, vol. 82, no. 3, p. 153, Mar. 2015, doi: 10.1364/jot.82.000153.

Chapter 3: Preliminary Experiments

3.1 Introduction

This chapter outlines the materials and methods used to measure the effect of tension on the Raman signature of demineralized equine bone, specifically the movement from bound-water to free-water. The primary aim was to determine if the Raman signature is correlated with the observation of stress-induced whitening in demineralized bone.

3.2 Materials

3.2.1 Specimen Preparation

Cortical bone beam specimens were cut from the mid-diaphysis of the right third metacarpal bone (MC3) of a three-year-old Thoroughbred gelding euthanized due to a unilateral biaxial proximal sesamoid bone fracture of the left forelimb while in race-training. The horse was necropsied as part of the California Horse Racing Board's racing safety program [1].

A 100 mm long section was cut from the dorsomedial aspect of the mid-diaphysis; this center of this section occurred at the proximodistal midpoint of the MC3 (Figure 3.1). Rectangular prism (2x2x40mm) bone beams were cut from this section, while under constant irrigation with deionized (DI) water using a diamond-coated bandsaw (Exakt Technologies, Oklahoma City, OK, USA) and a custom-built specimen jig. Specimens were cut so that the beam was parallel with the proximodistal axis of the bone. Figure 3.1 indicates where the bone beam specimens originate from within the cross-section of the MC3 bone (see Appendix A1 for more details). Bone beams were individually stored in in a Falcon tube containing 10 mL of saline (7 g NaCl/1 L DI H_2O) at -20°C. Samples were completely thawed in a refrigerator for 24 hours prior to use in experiments. For the preliminary experiments, three bone specimens were

used (n=3) with the following naming convention (where number indicates the row and color indicates the column): 8.1 Red, 8.1 Green, and 8.1 Navy.

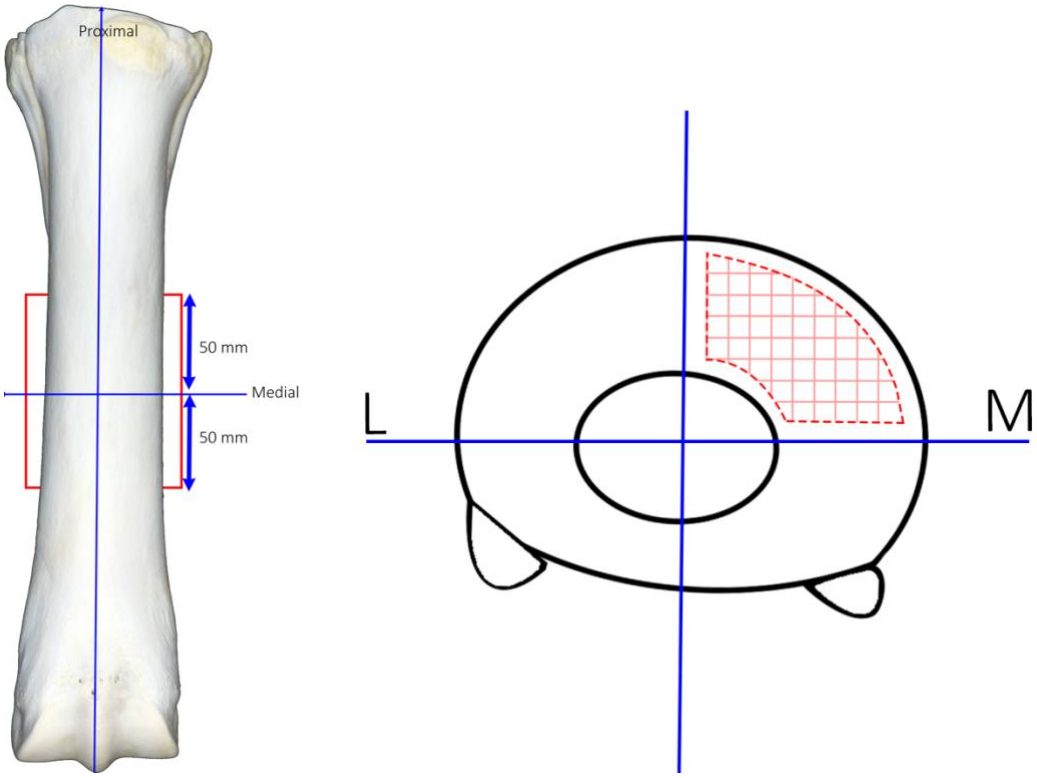

Figure 3.1: Left: Graphic of an equine MC3 bone. The proximal and medial axes are marked to show where the bone was cut. **Right:** Cross-section of the diaphysis of the equine third metacarpal bone (MC3). The vertical axis separates the lateral (L) and medial (M) regions of the bone. The red grid indicates the 2x2 mm cuts made within the dorsomedial quadrant of the MC3 to manufacture the bone beam specimens.

3.2.2 Demineralization

The central 5 mm of each bone beam was demineralized using a buffered [sodium citrate (100g/L)] formic acid (22.5% v/v) solution. This demineralization method was chosen because it maintains the integrity of the collagen network [2] and was successfully used for previous stress-whitening experiments in our laboratory [3], [4]. The proximal and distal ends of the bone beams (~17.5 mm each) were protected from demineralization by a coating of silicone sealant (Advanced Silicone 2, GE Sealants & Adhesives). The extent of demineralization was assessed using radiography (Dental Aire DTX) via visual inspection of x-ray transparency.

Demineralization media was changed every 24 hours until full demineralization was reached (~72-96 hours). Successful demineralization was indicated by complete transparency in the central ~5mm of the bone beams. Appendix A2 outlines the demineralization protocol in more detail.

3.2.3 H/D Exchange

The specimens (n=3) underwent a hydrogen/deuterium (H/D) exchange prior to testing. The purpose of the H/D exchange is to improve visualization of any changes in the spectral profile of collagen-bound and -unbound water caused by mechanical stress. Deuterium has its own identifiable peak (the OD-band) in the 2200-2800 cm^{-1} wavenumber range. In the characterization experiments (Section 2.2.1), the water region (~3000-3800 cm^{-1}) was difficult to detect using the 785 nm Raman laser; hence deuterium was identified to be a suitable surrogate and was used to measure the hydration state of the demineralized bone specimens. Deuterium is a hydrogen isotope; however, deuterium causes a spectral profile distinct from hydrogen due to its difference in mass. Replacing the hydrogen in a specimen with deuterium increases the signal-to-noise ratio, making shifts in intensities of the OD- (2200-2800 cm^{-1}) and OH-stretch modes (3000-3800 cm^{-1}) much more discernible [5]. For the purposes of this experiment, an H/D exchange (Appendix A3) enabled the changes in the spectral profile to be more apparent, thus aiding in the visualization of water moving between compartments of bone upon the application of tensile stress.

The bone specimens (n=3) were immersed in deuterium oxide (D_2O) (99.9% isotopic purity, Sigma-Aldrich, St. Louis, MO, USA). Deuteration was performed in an excess of D_2O and allowed to equilibrate for 24 hours under refrigeration. To confirm the infiltration of D_2O in

the bone beams, an initial Raman spectrum was collected to identify the OD-band (2200-2800 cm^{-1}). For reference, Raman spectra were acquired for bulk D_2O prior to testing.

3.3 Methodology

3.3.1 Mechanical Testing

Tensile testing experiments were conducted using a custom micromechanical tester (ADMET, Norwood, MA, USA) designed to fit on the stage of an inverted confocal scanning upright microscope for simultaneous Raman spectral imaging (see Appendix A8 for detailed experimental setup). Samples were placed in the serrated clamp grips and grip displacement was driven by a motor (Faulhaber, Clearwater, FL, USA). The testing system was controlled by ADMET's PC-based MTESTQuattro controller (ADMET, Norwood, MA, USA), which collected the mechanical data (i.e., position, load, temperature, etc.) at a rate of 20 samples/sec during each of the mechanical tests. Synchronized force and elongation data were collected during each experiment.

3.3.2 Raman Spectroscopy

Spectra were acquired using a custom-built inverted Raman scanning confocal microscope with an excitation wavelength of 785 nm and a 20x (NA=0.4) air immersion objective. The Raman spectra were processed using Solis v4.31.30005.0 software in Dr. Randy Carney's laboratory (Appendix A8 details the experimental setup). Exposure time was set to 10 seconds per scan with a laser power of 67 mW; power was measured just prior to the objective.

3.3.3 Experimental Procedure

Two separate test procedures were conducted on the three specimens. The two procedures are outlined in Section 3.3.3a and 3.3.3b.

3.3.3a Sitting in Solution Test Procedure

This experiment was conducted to assess if any changes in the Raman spectrum of deuterated, demineralized bone occur due to sitting in a saline solution. Specimens (n=3) were mounted with the mineralized ends of the beams secured in the grips. The grip separation was 31 mm, and the gauge length (demineralized portion of the specimen) was approximately 5 mm. The fluid bath was filled with saline solution (7 g NaCl/1 L DI H_2O). Raman data were collected every 20 minutes over the span of one hour (t=0, 20, 40, and 60 min). The initial time point (t=0 min) was chosen to be analogous to the Unloaded condition in the Mechanical Test, and similarly the t=60 min time point was chosen to be analogous to the Loaded condition in the Mechanical Test (see Section 3.3.3b). A 20x (NA = 0.4) objective was used on the microscope. Three kinetic series of 10 ten-second acquisitions were collected at each timepoint, for a total of 30 Raman spectra per timepoint. This experiment was conducted at ~26°C (i.e., the ceiling value of the temperature controller) in a temperature-controlled saline bath.

3.3.3b Mechanical Test Procedure

This experiment was conducted to assess if any changes in the Raman spectrum of deuterated, demineralized bone occur due to loading in tension. The bone beams (n=3) were mounted with the mineralized ends of the beams secured in the grips and loaded in tension at a constant strain rate of 0.001 s^{-1} to a nominal strain of 0.03 (calculated using the grip separation, i.e., displacement/31 mm). During characterization experiments (Section 2.3), beams fractured at an approximate nominal strain of 0.045 (displacement/31 mm), so the end strain value (0.03) was chosen as the maximum for these experiments to induce stress-whitening without breaking the specimen. Tests were performed under displacement-control (which is defined by the software as "strain"-control; see Section 2.1.4). After loading, the specimens were unloaded to zero strain at

a displacement rate of 1 mm/sec. The mechanical test protocol was repeated three times for each specimen, with no delay between mechanical tests.

For each sample, Raman data were collected three times before the mechanical test (Unloaded) and three times after the specimens were loaded in tension (Loaded). The Raman laser was refocused between each data collection. Three kinetic series of 10 ten-second acquisitions (i.e., 30 individual spectra) were collected for each instance of data collection with a 20x (NA = 0.4) objective. The Raman spectral data were used to calculate the *K* ratio for each increment (see Section 3.4.3).

Video data were captured during the full 30 second mechanical test (from 0 to 0.03 strain) for each experiment using a DJI Pocket 2 camera (DJI, Shenzhen, China). An external trigger was placed in the field of view and used to synchronize the video data with the mechanical and Raman data. A color calibration card was obtained online (DGK Color Tools) and included a grayscale reference. The calibration card was printed using a laser printer, and the print quality was fine enough to suit the purpose of a correction factor. The grayscale calibration card was included in the field of view for reference and the black rectangle was used as a correction factor for the whitening calculations. This experiment was conducted at ~26°C (i.e., the ceiling value of the temperature controller) in a temperature-controlled saline bath.

3.4 Data Reduction

The video data were used to calculate the stress-whitening of the bone beams (Section 3.4.1). The Raman data was processed (Section 3.4.2) and used to perform the Principal Component Analysis (PCA).

3.4.1 Video Data Reduction

Stress-whitening was quantified using a custom macro in ImageJ/Fiji (NIH, Bethesda, MD, USA). Specifically, stress-whitening was quantified by comparing the average pixel intensity of the rectangular region of interest (ROI; Figure 3.2; right) to the initial (pre-strained) pixel intensity of the ROI (Figure 3.2; left). The pixel intensity was corrected by using the black rectangle on the grayscale calibration card that was included in the frame for all videos (Figure 3.2). Stress-whitening (W) was calculated using the following equation [3]:

$$W = \frac{\frac{\sum_x \sum_y I_{max}(x,y)}{n_{pixel}} - \frac{\sum_x \sum_y I_{init}(x,y)}{n_{pixel}}}{\frac{\sum_x \sum_y I_{init}(x,y)}{n_{pixel}} - I_{correction}}$$

Where I_{max} is the intensity of the ROI; I_{init} is the intensity of the ROI prior to loading; $I_{correction}$ is the average intensity of the black rectangle on the grayscale calibration card included in the frame; and n_{pixel} is the area of the ROI.

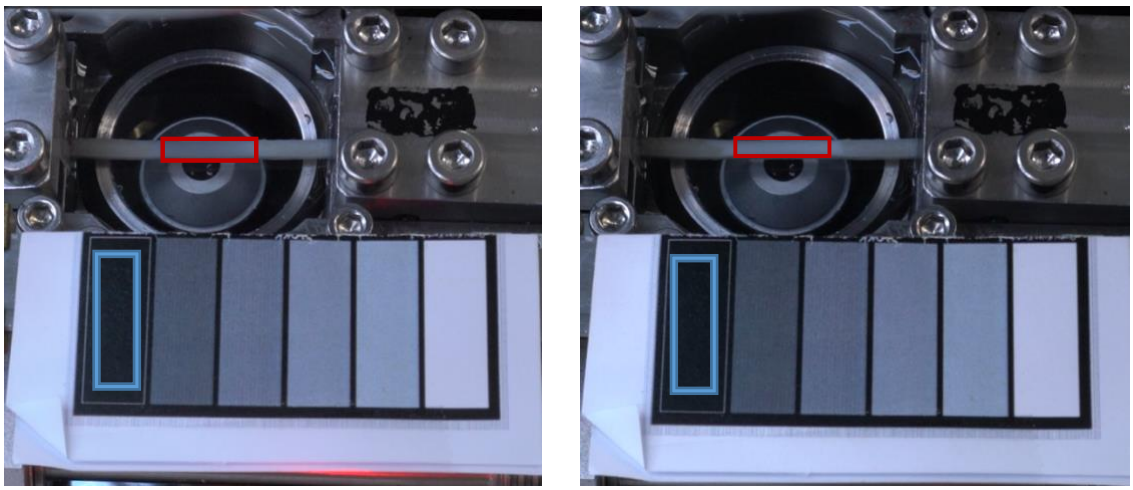

Figure 3.2: Comparison of a demineralized bone specimen in the unloaded state (left) and the loaded state (right). The red rectangle shows the ROI that was used to calculate the pixel intensity of the bone beam. The blue rectangle shows the ROI that was used to calculate the pixel intensity of the black rectangle on the grayscale calibration card.

Whitening time points were determined using the external trigger that was placed in the field of view of the camera during the experiments. This method was used to identify the whitening during the ramp to the final nominal strain of 0.03.

3.4.2 Raman Spectral Data Pre-processing

Spectral data processing was conducted using a custom MATLAB (MathWorks, Natick, MA, USA) program called "Noodle," from the Carney Lab (Randy Carney, UC Davis, unpublished). First, noise is minimized in the raw spectra using a Whittaker smoother (Whittaker value = 5) [9]. Second, the smoothed spectra undergo baseline correction using airPLS (adaptive iteratively reweighted Penalized Least Squares) [10], [11]. Baseline correction is necessary because Raman spectral data are subject to baseline drift, a low frequency vertical shift in the raw data, which distorts peak position and area [11]. Figure 3.3 illustrates baseline correction using airPLS and how changing the lambda value controls the smoothness and location of the baseline [10]; a lambda value of $1x10^6$ was used for all data. Third, the smoothed and background-subtracted spectra were unit normalized (i.e., area under the curve was set equal to one). This normalization procedure normalized to the total intensity of the spectrum to remove artifacts [12].

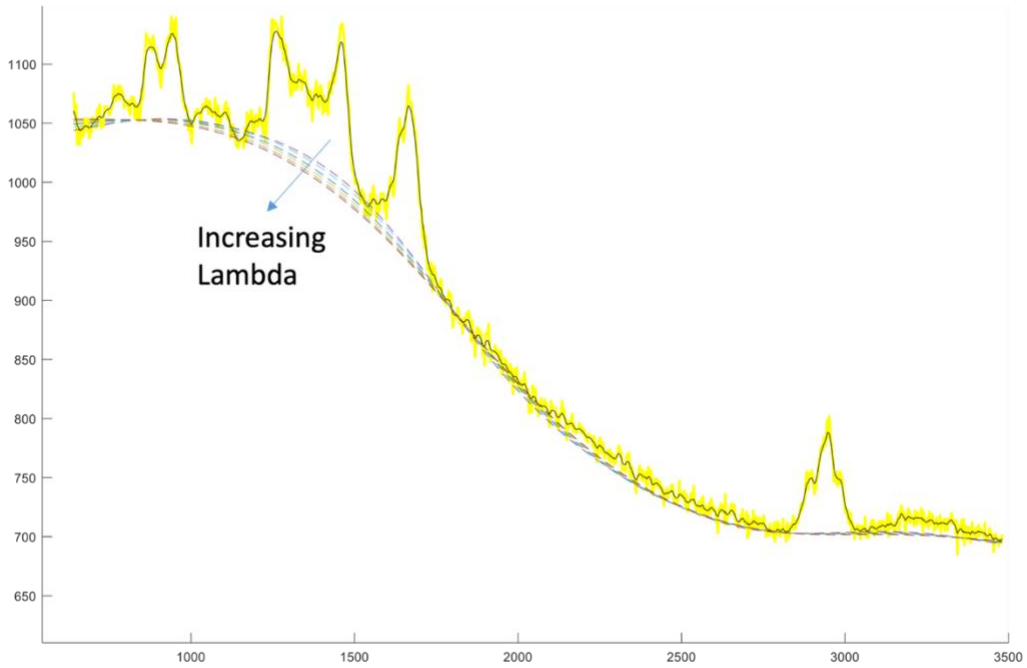

Figure 3.3: The effect of increasing lambda value during baseline correction of raw Raman spectral data using airPLS (adaptive iteratively reweighted Penalized Least Squares). The blue arrow indicates the shift of the baseline with increase in the lambda value from $1x10^6$ to $6x10^6$.

For the two test procedures (Sitting in Solution and Mechanical Test), the Raman spectra from each kinetic series for each Specimen (8.1 Red, 8.1 Green, and 8.1 Navy) and each Condition (t = 0, 20, 40 60 min *or* Unloaded, Loaded, respectively) were averaged. Due to a recording error, Specimen 8.1 Red only had one kinetic series at timepoint t=0, for the Sitting in Solution Test. So, for the Sitting in Solution Test there was a total of 34 data points ((3 samples * 4 tests/sample * 3 kinetic series/test) – 2 kinetic series = 34 data points total). For the Mechanical Test there was a total of 54 data points (3 samples * 3 tests/sample * 2 conditions/test * 3 kinetic series/condition = 54 data points total).

The grand averages of the Raman spectra of all samples for each test condition (t = 0, 20, 40 60 min *or* Unloaded, Loaded, respectively) were then calculated **(**Figure 3.4 and Figure 3.5, respectively).

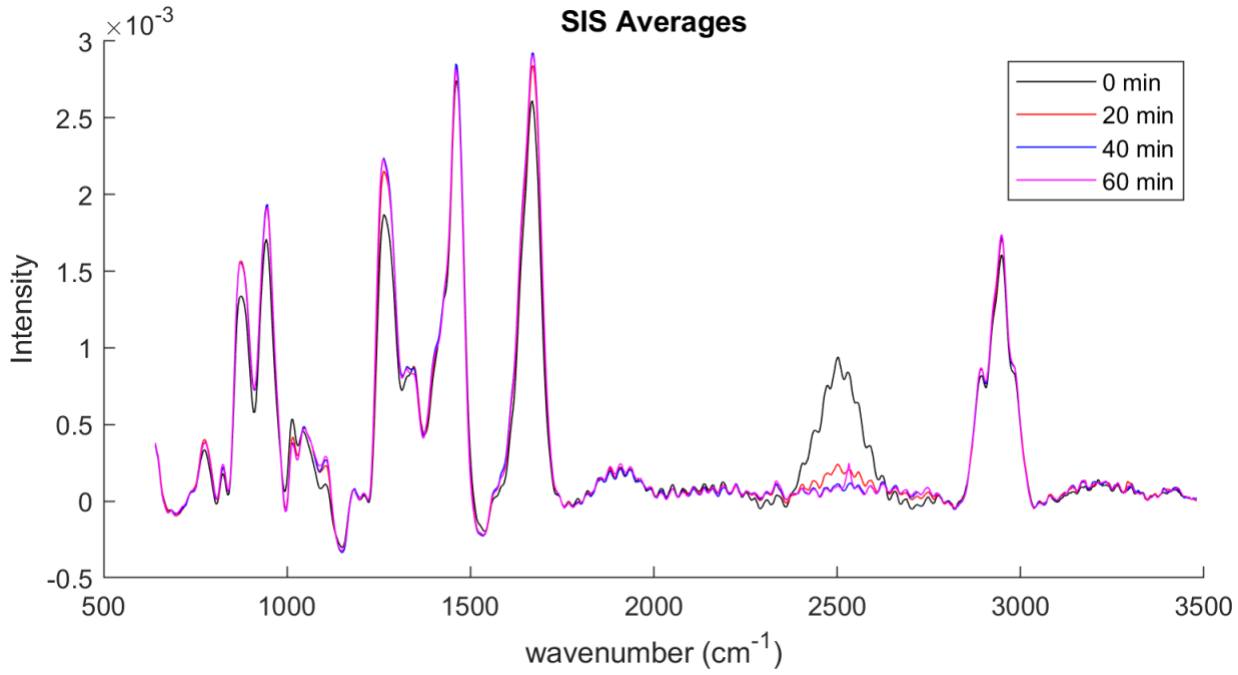

Figure 3.4: Grand averages of the Raman spectral data collected during the Sitting in Solution Test for each timepoint (0 min = black; 20 min = red; 40 min = blue; 60 min = magenta).

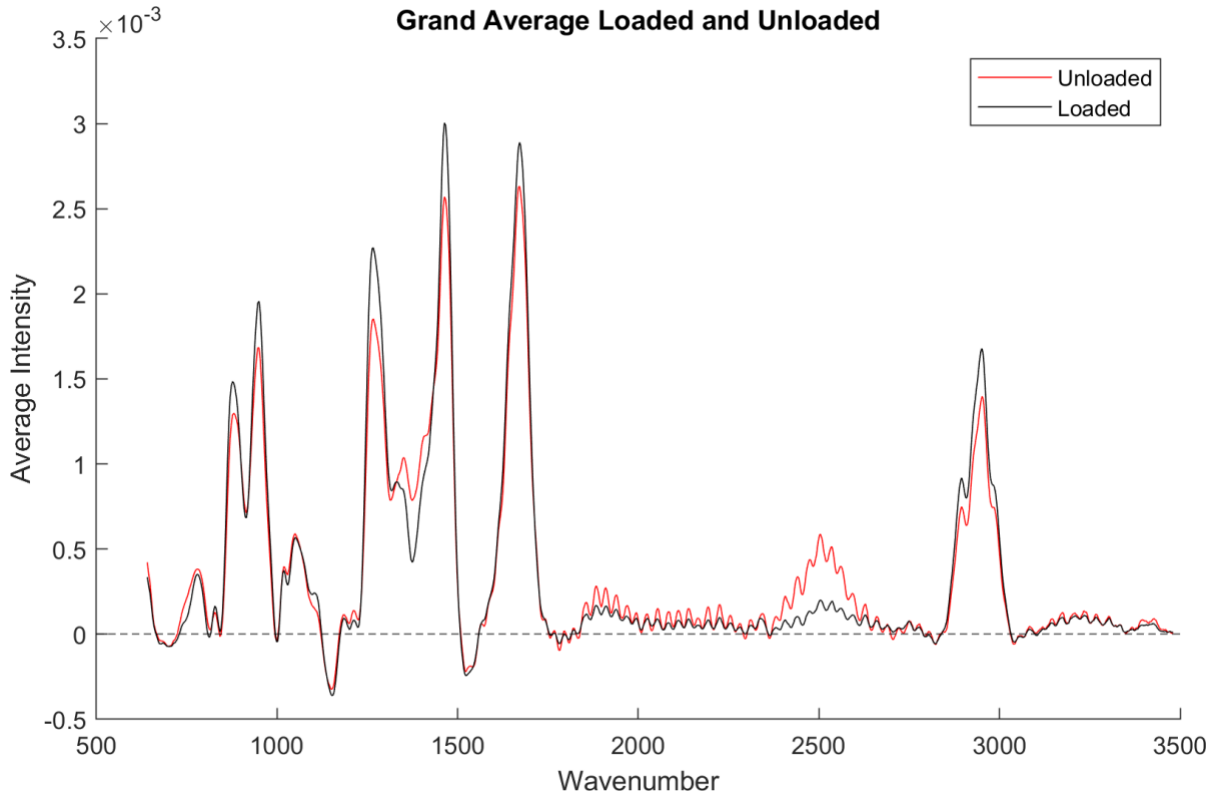

Figure 3.5: Grand averages of the Raman spectral data collected during the Mechanical Test for each condition (Unloaded = red; Loaded = black).

3.4.3 *K* Ratio Calculation

Raman spectroscopy was used to estimate the mechanically driven changes in water location within bone by measuring changes in the ratio of the intensities of the two main Gaussian OH-stretch components. This ratio (*K*) was characterized by Walrafen and colleagues as follows: $K = I_1 / I_2$, where I_1 is the wavenumber value of the symmetric OH stretch mode and I_2 is the wavenumber value of the asymmetric OH stretch mode [6].

The *K* ratio is proportional to the ratio of bound (I_1) to free water (I_2) in a collagen fibril and is correlated with changes in the interaxial spacing between collagen triple helices [6], [7]. Further, the *K* ratio has been used to measure the changes in location of water within the collagen triple helices in glutaraldehyde crosslinked pericardial tissue [8]. For glutaraldehyde-treated tissue, I_1 is equivalent to the lower wavenumber component of OH-stretch (3220-3243 cm^{-1}) and I_2 is equivalent to the higher wavenumber component of OH-stretch (3429-3445 cm^{-1}). Previous work showed that *K* decreased upon crosslinking with glutaraldehyde, which the researchers reported as an increase in the number of water molecules in the hydration shell surrounding the collagen of the pericardial tissue and an increase in the interaxial distance between collagen triple helices [8].

Therefore, we will use the *K* ratio to measure the effects of different stress-whitening factors (e.g., tension, dehydration, etc.) on the movement of water between compartments (i.e., the transition between bound water and free water) within the demineralized bone samples. In the deuterated, demineralized bone samples, the intensities of the two main Gaussian OD mode components serve as a surrogate for those of the OH-stretch mode to determine the *K* ratio. So, I_1 is set to the peak intensity at the lower wavenumber component of the OD mode and I_2 = peak intensity of the higher wavenumber component of the OD mode. These peaks occurred at 2400

cm^{-1} and 2500 cm^{-1}, respectively, which were determined by identifying local maxima on the OD mode. So, in the deuterated samples, $K = I_{2400cm\text{-}1} / I_{2500cm\text{-}1}$ (where $I_{2400cm\text{-}1}$ is the intensity at the lower wavenumber component of the OD mode and $I_{2500cm\text{-}1}$ is the intensity at the higher wavenumber component of the OD mode). A custom code (MATLAB, MathWorks, Natick, MA, USA) was used to determine the *K* value before and after the specimen was loaded in tension to stress-whitening.

3.4.4 Principal Component Analysis

Raman spectral data are complex, and therefore Principal Component Analysis (PCA) is commonly performed to mathematically reduce the dimensionality of the data to make it easier to analyze [13]–[15]. PCA decomposes data into principal components (PCs) which account for variability of the data and summarize its main features [13], [14]. To perform Principal Component Analysis, first the data must be centered around zero [13]. The first PC is found by drawing a line through the data which minimizes the total distance between each data point and its projection onto the line (thus maximizing the distance from the origin, via Pythagorean's Theorem). The distances between the origin and each projection onto the line are squared (to account for negative values) and summed. The line through the data with the largest sum of squared distances is principal component 1 (PC 1). This process is equivalent to performing multiple linear regression in which the perpendicular distance from the PC to the data point is minimized [14]. The "PC loading scores," are the perpendicular distances from each of the datapoints to the PC [13]. These scores indicate the level of contribution of the feature to the PC. Thus, the larger the score, the more that spectral feature contributes to the PC [15]. Each subsequent PC is orthogonal to the previous PC; hence all PC scores are uncorrelated with each other [14]. The PC scores are stored in "PCA loading plots" which visually depict how strongly

certain spectral features of each PC influence the original dataset. The original data can be expressed as a linear combination of the PC "scores" multiplied by the "loading" coefficients (also known as "weights").

For the purposes of this project, PCA was performed using a custom MATLAB (MathWorks, Natick, MA, USA) program called "Noodle," written by the Carney Lab (Randy Carney, UC Davis, unpublished). To improve the signal-to-noise ratio, PCA was performed using the averages of each kinetic series from each condition of two test procedures (see Section 3.4.2).

PC scores and loadings for the PCs accounting for ~90% of the variance were extracted for each spectral recording. Tables 3.1 and 3.2 provide the spectral variance accounted for by the first 10 PCs for both tests.

Table 3.1: Spectral variance of the Sitting in Solution Test Raman spectral data, accounted for by the first 10 principal components. The first three PCs (bolded) account for ~90% of the variance in the spectral data.

Principal Component	Percent Variability	Cumulative Variability
1	**75.50%**	**75.50%**
2	**13.03%**	**88.52%**
3	**3.69%**	**92.21%**
4	2.22%	94.43%
5	0.78%	95.20%
6	0.56%	95.77%
7	0.44%	96.21%
8	0.38%	96.59%
9	0.33%	96.92%
10	0.28%	97.20%

Table 3.2: Spectral variance of the Mechanical Test Raman spectral data, accounted for by the first 10 principal components. The first four PCs (bolded) account for ~90% of the variance in the spectral data.

Principal Component	Percent Variability	Cumulative Variability
1	**54.18%**	**54.18%**
2	**19.27%**	**73.45%**
3	**15.16%**	**88.61%**
4	**3.82%**	**92.43%**
5	2.30%	94.73%
6	1.35%	96.07%
7	0.83%	96.91%
8	0.67%	97.57%
9	0.40%	97.97%
10	0.27%	98.24%

Figure 3.6 is a 3-dimensional plot of the PC scores from the first three PCs for the Sitting in Solution Test data. Figure 3.7 is a 3-dimensional plot of the PC scores from the first three PCs for the Mechanical Test data.

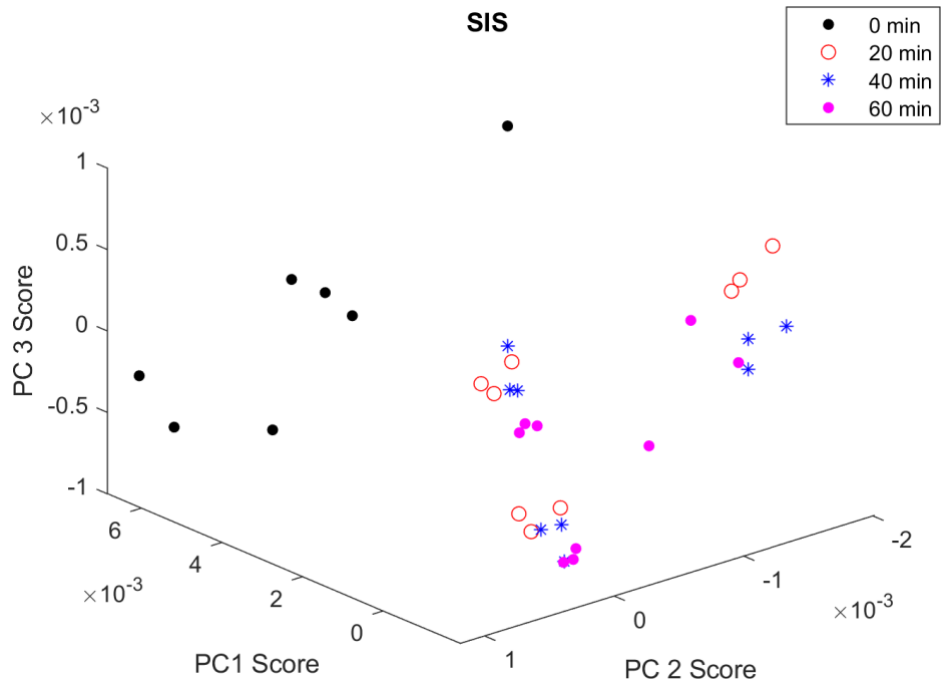

Figure 3.6: 3-dimensional plot of the PC scores from the first three PCs from the data collected during the Sitting in Solution Test (0 min = black; 20 min = red; 40 min = blue; 60 min = magenta). This plot illustrates that the t=0 min time point was separated from the t=20-, 40-, and 60-min times points.

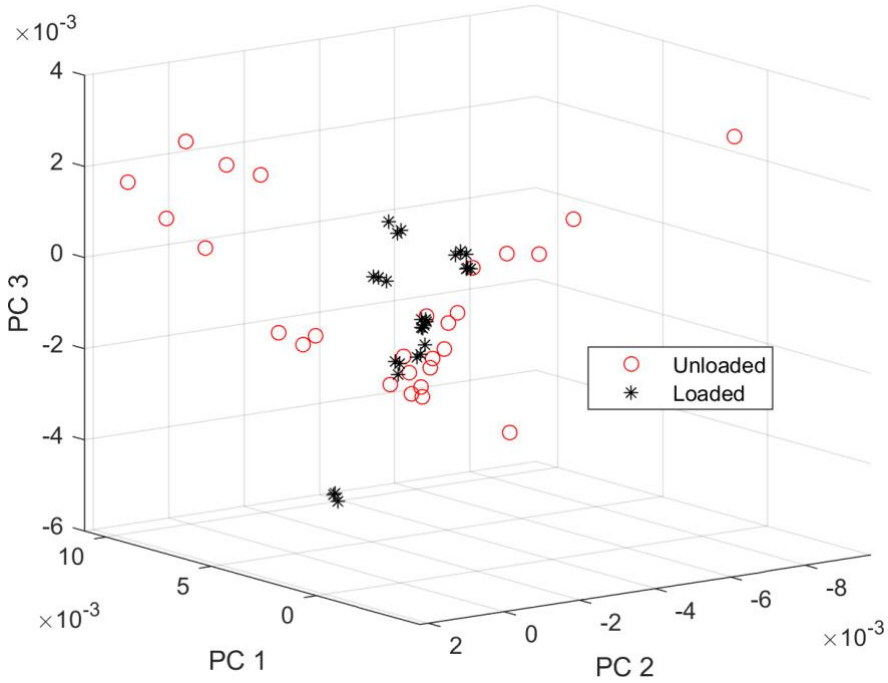

Figure 3.7: 3-dimensional plot of the PC scores from the first three PCs from the data collected during the Mechanical Test (Unloaded = red; Loaded = black).

3.5 Statistical Analysis

Even though there was a small sample size, preliminary statistics were performed on this data set. All statistical analyses were performed using SAS 9.4 (SAS Institute Inc., Cary, North Carolina, USA). Univariate linear mixed models (LMM) were performed on the PC 1, PC 2, and PC 3 scores from the Sitting in Solution Test to assess whether there is an effect of prolonged saline submersion on the Raman signature of deuterated, demineralized bone (t=0, 20, 40, and 60 min). Only PC 1, PC 2, and PC 3 scores were tested because they accounted for ~90% of the variance in the Sitting in Solution Test. For each LMM, the fixed effect was Timepoint (t=0, 20, 40, and 60 min) and the random effect was Sample ID.

LMMs were also performed on the Mechanical Test PC Scores to assess whether there is an effect of mechanical loading on the Raman signature of deuterated, demineralized bone (Unloaded and Loaded). Specifically, univariate LMMs were performed on the PC 1, PC 2, PC 3, and PC 4 scores because they accounted for ~90% of the variance in the spectral data. For

these LMMs, the fixed effects were Condition (Unloaded or Loaded), Test Number (Test Number = 1, 2, or 3), the interaction of Condition and Test Number, and Temperature; and the random effect was Sample ID.

White value is defined as a relative measure between the Loaded and Unloaded Conditions. First, a LMM was performed on Loaded data to determine if Test Number (1, 2, and 3) had a significant effect on the mean white value. Because Test Number did not affect the mean white value, a second intercept-only LMM was used to test if the mean white value from Loaded tests was different from zero (i.e., the Unloaded value). Due to the small sample size, Sample ID could not be included in these two LMMs as a random effect.

All LMMs were performed in SAS 9.4 using the "proc mixed" function, with a p-value of 0.05 considered significant. Shapiro-Wilk W-scores were used to check for residual normality ($W > 0.9$ indicated normal distribution of residuals). If $W < 0.9$, then those PC scores were ranked, and the LMM was performed using the ranked data. The differences of the Least Square Means were included in the mixed procedure to assess the model means and comparisons (Tukey-Kramer adjustment; $p \leq 0.05$ significant). Additionally, for the Mechanical Test Data, a post hoc test for simple differences in Condition means and Test Number means was performed.

3.6 Results

3.6.1 Sitting in Solution Test

The deuterium oxide signal in the deuterated demineralized bone specimens decays to zero over the one-hour period of sitting in saline solution. Rapid decrease of the OD-band (~2200-2800cm^{-1}) occurs within the first 20 minutes of sitting in saline solution (Figure 3.4). Between 20 and 60 minutes, the OD-band decreases to baseline (Figure 3.4). All other major peaks, specifically in the fingerprint region (~400-1800 cm^{-1}) and the CH-stretch peak (~2950

cm^{-1}), show an intensity increase between t=0 min and t=60 min (the black and magenta curves, respectively, in Figure 3.4).

These observations were confirmed by the LMM performed on PC 1, PC 2, and PC 3. Timepoint (t = 0, 20, 40, or 60 min) was significant for PC 1 ($p<0.0001$), PC 2 ($p=0.0054$), PC 3 ($p<0.001$), and PC 4 ($p<0.001$), as shown in Table 3.3. For PC 1 and PC 3 the mean PC score of the first time point (t = 0) was significantly different from the t=20-, 40-, and 60-minute time points (Table 3.4). Likely, the mean PC Scores at t = 0 were significantly different because the OD-peak decreased intensely during the first 20 minutes. For the PC 3 scores, the difference of the Least Square Means also indicates that the t=60 min data was significantly different from all other time points. Perhaps this effect results from the D_2O diffusion stabilizing over the one-hour period.

Table 3.3: Results of the linear mixed model for the Sitting in Solution Test. *Significance $p<0.05$.

Dependent Variable	Effect	P-value for Type 3 Effect	W Score for Residual Normality
PC 1	Timepoint	0.0001*	0.95
PC 2	Timepoint	0.0054*	0.92
PC 3	Timepoint	0.0001*	0.99
PC 4 (ranked)	Timepoint	0.0001*	N/A

Table 3.4: Differences of Least Square Means (standard error) of PC scores for the Sitting in Solution Test. In each column, means that share a superscript (A, B, C) are not significantly different at $p \leq 0.05$.

Timepoint	PC 1	PC 2	PC 3
t = 0 min	0.004268 (0.000670) ^{A}	0.000236 (0.000677) ^{A}	0.000267 (0.000343) ^{A}
t = 20 min	-0.00048 (0.000651) ^{B}	-0.00029 (0.000675) ^{B}	0.000044 (0.000342) ^{B}
t = 40 min	-0.00137 (0.000651) ^{B}	-0.00013 (0.000675) ^{B}	-6.35E-6 (0.000342) ^{B}
t = 60 min	-0.00131 (0.000651) ^{B}	-0.00006 (0.000675) $^{A, B}$	-0.00020 (0.000342) ^{C}

3.6.2 Mechanical Test

3.6.2a Stress-whitening

Whitening was observed during each mechanical test. A representative photo of a demineralized bone specimen in the Unloaded state (not whitened) and Loaded state (whitened) is shown in Figure 3.2. The average whitening (AW) value for each specimen, over all three tests, is shown in Figure 3.8. The AW for each specimen increased monotonically with strain. The maximum and minimum AW values were identified for specimens. The maximum final AW value was 0.209 (specimen 8.1 Navy) and the minimum final AW value was 0.192 (specimen 8.1 Red). A linear trendline with an R^2 value of 0.9854 was fit to the AW for all the bone specimens (shown in red on Figure 3.8). The grand average of stress-whitening is shown in Figure 3.9 and follows the same trend. The final AW value was 0.20. Overall, whitening was apparent and increased monotonically with strain.

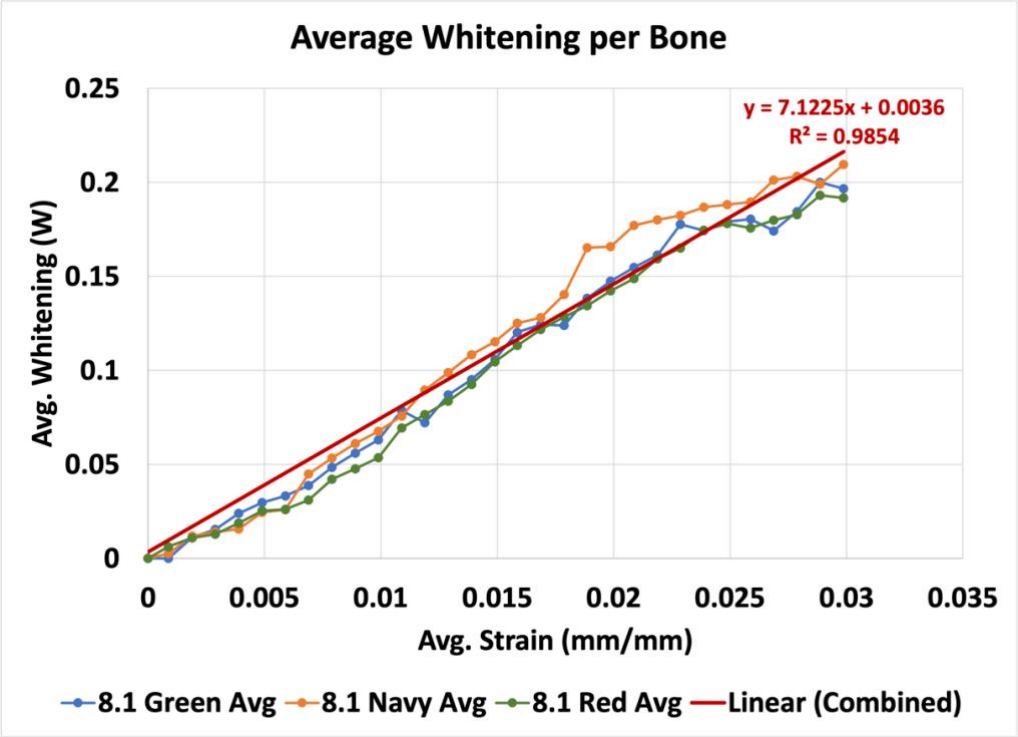

Figure 3.8: Average of whitening of all three mechanical tests for each specimen (n=3) plotted against average strain. A linear trendline is fit to the data and has an $R^2 = 0.9854$.

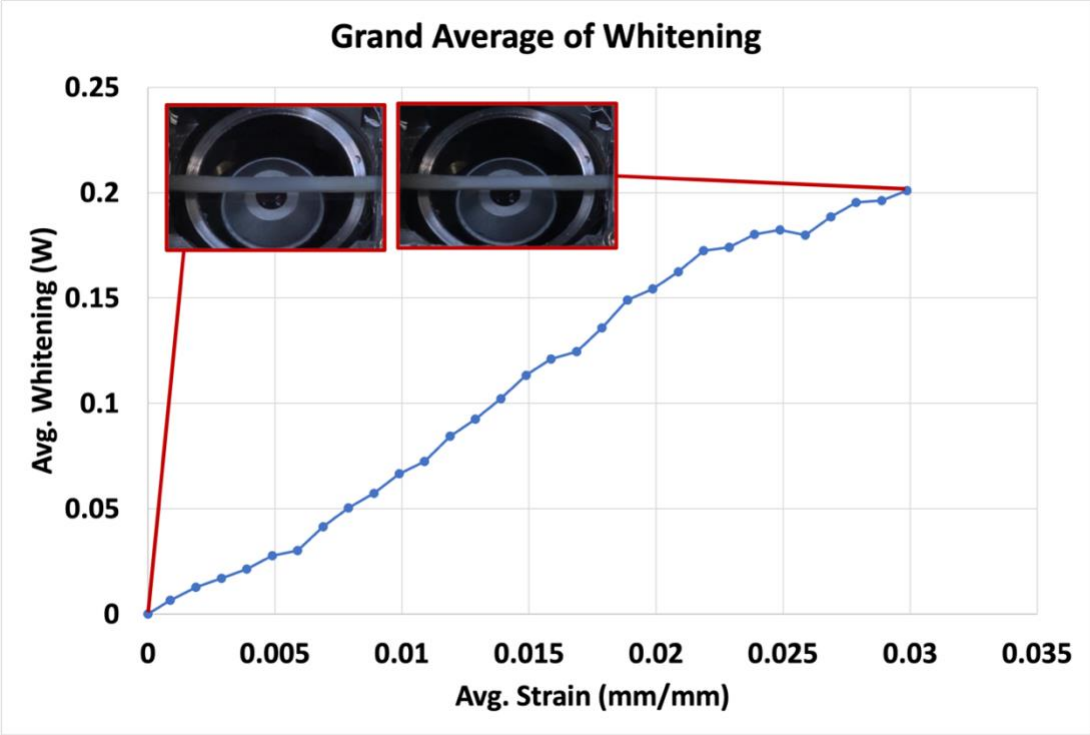

Figure 3.9: Grand average of whitening for all specimens (n=3) plotted against average strain.

3.6.2b Raman Spectral Data

Figure 3.5 shows grand averages of the Unloaded and Loaded Raman spectra. Specifically, the OD-peak (~2200-2800 cm^{-1}) intensity decreased upon loading, whereas most other peaks (including proline, hydroxyproline, amide III, CH_2, amide I, and CH-stretch; see Table 2.1 for wavenumber ranges) increased upon loading.

Condition had a significant effect on PC 1 ($p<0.0001$) and PC 2 ($p<0.0001$), but not PC 3 ($p=0.1244$) or PC 4 ($p=0.0976$). Test Number had a significant effect on PC 1 ($p<0.0001$), PC 2 ($p<0.0001$), and PC 3 ($p=0.0145$). The interaction of Condition and Test Number was only significant for PC 1 ($p<0.0001$). Temperature was not significant for any of the dependent variables (the temperature was 26.08°C ± 0.55). Table 3.5 contains the results from the univariate LMM. For PC 1, the G matrix was not positive definite, so Sample ID was removed as a random effect for PC 1 to fix this error [16]. Pairwise differences in the in the Least Square Means of the PC scores from PC 1, PC 2, PC 3, and PC 4 are reported in Table 3.6.

Table 3.5: Results of the linear mixed model for the Mechanical Test. *Significance $p<0.05$. †G matrix was not positive definite, therefore removed sample ID as a random effect. Ranked PC data was used for PC 2 and PC 4 because the W-score on the raw data's LMM was < 0.90.

Dependent Variable	Effect	P-value for Type 3 Effect	W Score for Residual Normality
PC 1†	Condition	0.0001*	0.93
	Test #	0.0001*	
	Cond * Test	0.0001*	
	Temp_C	0.0717	
PC 2 (ranked)	Condition	0.0001*	N/A
	Test #	0.0001*	
	Cond * Test	0.1831	
	Temp_C	0.0838	
PC 3	Condition	0.1244	0.91
	Test #	0.0145*	
	Cond * Test	0.9886	
	Temp_C	0.3128	
PC 4 (ranked)	Condition	0.0976	N/A
	Test #	0.0776	
	Cond * Test	0.8058	
	Temp_C	0.9364	

Table 3.6: Least Square Means (standard error) of principal component scores from the LMM of the Mechanical Test. Across a row, simple differences in Condition means are indicated by subscripts (a, b). Down a column, simple differences in the Test Number means are indicated by superscripts (A, B, C). Significance was set at $p \leq 0.05$.

PC 1		
	Unloaded	Loaded
Test 1	$0.000236\ (0.000533)_{a}$ ^{A}	$-0.00030\ (0.000532)_{a}$ ^{A}
Test 2	$-0.00279\ (0.000532)_{a}$ ^{B}	$0.005994\ (0.000530)_{b}$ ^{B}
Test 3	$-0.00081\ (0.000530)_{a}$ ^{A}	$-0.00232\ (0.000538)_{a}$ ^{C}
PC 2		
	Unloaded	Loaded
Test 1	$-0.00159\ (0.000683)_{a}$ ^{A}	$0.001010\ (0.000680)_{b}$ ^{A}
Test 2	$0.000612\ (0.000680)_{a}$ ^{B}	$0.001156\ (0.000679)_{a}$ ^{A}
Test 3	$-0.00170\ (0.000679)_{a}$ ^{A}	$0.000506\ (0.000688)_{b}$ ^{A}
PC 3		
	Unloaded	Loaded
Test 1	$-0.00084\ (0.000840)_{a}$ ^{A}	$-0.00034\ (0.000839)_{a}$ ^{A}
Test 2	$0.000329\ (0.000839)_{a}$ $^{B, C}$	$0.000907\ (0.000838)_{a}$ $^{B, C}$
Test 3	$-0.00025\ (0.000838)_{a}$ $^{A, C}$	$0.000206\ (0.000843)_{a}$ $^{A, C}$
PC 4		
	Unloaded	Loaded
Test 1	$0.000363\ (0.000333)_{a}$ ^{A}	$-0.00024\ (0.000332)_{a}$ ^{A}
Test 2	$0.000178\ (0.000332)_{a}$ ^{A}	$-0.00016\ (0.000331)_{a}$ ^{A}
Test 3	$-0.00005\ (0.000331)_{a}$ ^{A}	$-0.00009\ (0.000336)_{a}$ ^{A}

Test Number did not have a significant effect on mean white value ($p = 0.059$) collected for Loaded data. Additionally, the mean white value of the Loaded data was significantly different from zero (the white value of the Unloaded data).

3.7 Discussion

3.7.1 Sitting in Solution Test

Raman spectral data were collected every 20 minutes over a one-hour period to measure any changes in the deuterated, demineralized bone that might result from sitting in a saline solution. The most distinct peak intensity change occurred in the OD-band (~2200-2800 cm^{-1}), which decayed to zero over the one-hour period. The intense decrease in the OD-band indicates

that most of the deuterium oxide in the specimen passively diffused into the saline solution during the first 20 minutes. Generally, all other peaks experienced slight increases in intensity, which could be a consequence of unit normalization. Since the spectra were normalized to the total area under the curve, when the OD-band intensity reduced greatly, perhaps it caused the other peak intensities to compensate with a slight increase in intensity.

The results of this experiment indicate that there is complete decay of the D_2O signal independent from mechanical loading. Because of the complete collapse in the signal, D_2O could not be successfully used as a signal intensifier and surrogate for water, for the purposes of a *K* ratio calculation. Therefore, the K ratio was not calculated as initially proposed (Section 3.4.3).

3.7.2 Mechanical Test

Deuterated, demineralized bone beam specimens were loaded to a point of stress-whitening. The intensity of the OD-band (~2200-2800 cm^{-1}) decreased upon loading deuterated, demineralized bones in tension to a strain of 0.03 (Figure 3.5). However, as discussed in Section 3.7.1, the OD-band also decayed to baseline while sitting in a saline solution under no mechanical load. The decrease in the deuterium peak in both the loaded and unloaded conditions were so similar that it is impossible to ascertain whether the decrease of the peak in the loaded condition was not simply due to time in saline solution. Therefore, it cannot be concluded that the OD-band intensity changed as an effect of mechanical loading or stress-whitening.

Other notable changes were present in the Raman signal upon loading, indicating that there might be an effect of mechanical loading on stress-whitening, independent from deuteration. More specifically, increases were seen in the intensities of the proline (~855cm^{-1}), hydroxyproline (~876 cm^{-1}), amide III (~1243-1320 cm^{-1}), CH_2 (~1450 cm^{-1}), amide I (~1616-1720 cm^{-1}), and CH-stretch (~2700-3100 cm^{-1}) regions. However, as stated above, these peak

intensity changes could be an effect of sitting in solution and normalization of the data during processing. To further investigate these peak intensity changes, additional experiments will be conducted without the use of an H/D exchange (Chapter 4), to eliminate this potential confounder. The aim of these experiments will be to identify changes in the overall Raman spectrum of demineralized bone that are correlated with the stress-whitening phenomenon.

3.7.3 Limitations

There are several equipment-related limitations that must be discussed. First, the temperature controller was unable to heat the fluid bath to the desired temperature of 38°C (i.e., equine physiological temperature) due to the previously discussed issues with controller operation (Section 2.1.6). Therefore, the temperature of the saline bath was heated to about 26°C, which was the maximum capability of the controller at that time. Second, the mechanical tester was unable to accurately measure load (Section 2.1.5), so load and stress data were not included in the study. Third, the mechanical tester rested at a slight angle on the Raman microscope platform, so the laser beam did not enter the demineralized bone specimens at exactly 90°. Finally, the laser must be cooled to -60°C prior to taking Raman measurements; because the laser cannot be powered on during the mechanical test, the laser must be powered on and allowed to cool before collecting Raman data of the loaded specimen. Therefore, the loaded specimen is held in tension for about eight minutes before the Loaded Raman data is collected, which might allow for specimen stress-relaxation and potential loss of whitening. In future experiments, video data should begin from the start of the mechanical test up to Raman data collection to assess if stress-relaxation and loss of whitening occurs during that period.

3.8 Summary

The results of this study indicate that the Raman signature of deuterated, demineralized bone changes upon loading in tension. As anticipated, there was a decrease in the intensity of the OD-band in the Raman signal of the Loaded specimens. However, because the results of the Sitting in Solution Test indicate that deuterium oxide was passively leaching from the specimens, it cannot be stated that loading in tension caused the decrease in the OD-band intensity. Therefore, it remains unclear whether loading in tension and the observation of stress-whitening is directly related to the movement of water from a bound-state to a free-state in the collagen fibrils of demineralized bone. However, changes were also measured in the fingerprint region of the Raman spectra, indicating that stress-whitening may be attributed to other changes in the structure of demineralized bone upon loading.

In conclusion, it appears that there may be an effect of mechanical loading on the Raman spectra of demineralized bone, independent from the hydration state of the collagen phase. The next set of experiments will better characterize the change in the Raman signature during stress-whitening without the potential confounder of the time dependent changes in the spectrum caused by the initial use of deuterium.

References

[1] JD Wheat Veterinary Orthopedic Laboratory, “Equine Health Research,” 2021. https://vorl.vetmed.ucdavis.edu/research-programs/equine-health-research (accessed Mar. 21, 2022).

[2] Y. N. Yeni, M. B. Schaffler, G. Gibson, and D. P. Fyhrie, “Prestress due to dimensional changes caused by demineralization: A potential mechanism for microcracking in bone,” *Annals of Biomedical Engineering*, vol. 30, no. 2, pp. 217–225, 2002, doi: 10.1114/1.1451078.

[3] M. R. Hardisty, T. C. Garcia, S. Choy, J. Dahmubed, S. M. Stover, and D. P. Fyhrie, “Stress-whitening occurs in demineralized bone,” *Bone*, vol. 57, no. 2, pp. 367–374, Dec. 2013, doi: 10.1016/j.bone.2013.08.029.

[4] M. R. Hardisty, M. A. Soicher, T. C. Garcia, S. M. Stover, and D. P. Fyhrie, “Do stress-whitening and optical clearing of collagenous tissue occur by the same mechanism?,” *Journal of Biomechanics*, vol. 46, no. 14, pp. 2411–2418, Sep. 2013, doi: 10.1016/j.jbiomech.2013.07.026.

[5] J. J. Katz, “Chemical and Biological Studies with Deuterium,” *American Scientist*, vol. 48, no. 4, pp. 544–580, 1960, [Online]. Available: https://www.jstor.org/stable/27827650

[6] G. E. Walrafen and Y.-C. Chu, “Nature of collagen-water hydration forces: a problem in water structure,” *Chemical Physics*, vol. 258, no. 2–3, pp. 427–446, 2000, doi: 10.1016/S0301-0104(00)00072-0.

[7] S. Leikin, V. A. Parsegian, W.-H. Yang, and G. E. Walrafen, “Raman spectral evidence for hydration forces between collagen triple helices,” *Biophysics*, vol. 94, pp. 11312–11317, 1997, [Online]. Available: www.pnas.org.

[8] M. Jastrzebska, R. Wrzalik, A. Kocot, J. Zalewska-Rejdak, and B. Cwalina, “Hydration of glutaraldehyde-fixed pericardium tissue: Raman spectroscopic study,” *Journal of Raman Spectroscopy*, vol. 34, no. 6, pp. 424–431, Jun. 2003, doi: 10.1002/jrs.1016.

[9] P. H. C. Eilers, “A perfect smoother,” *Analytical Chemistry*, vol. 75, no. 14, pp. 3631–3636, Jul. 2003, doi: 10.1021/ac034173t.

[10] Z. M. Zhang, S. Chen, and Y. Z. Liang, “Baseline correction using adaptive iteratively reweighted penalized least squares,” *Analyst*, vol. 135, no. 5, pp. 1138–1146, 2010, doi: 10.1039/b922045c.

[11] Y. Liu and J. Lin, “A general-purpose signal processing algorithm for biological profiles using only first-order derivative information,” *BMC Bioinformatics*, vol. 20, no. 1, Nov. 2019, doi: 10.1186/s12859-019-3188-4.

[12] N. K. Afseth, V. H. Segtnan, and J. P. Wold, “Raman Spectra of Biological Samples: A Study of Preprocessing Methods,” *Applied Spectroscopy*, vol. 6, no. 12, pp. 1358–1367, 2006.

[13] A. M. C. Davies and T. Fearn, “Back to basics: the principles of principal component analysis,” *Spectroscopy Europe*, pp. 20–23, [Online]. Available: www.spectroscopyeurope.com

[14] J. Lever, M. Krzywinski, and N. Altman, “Points of Significance: Principal component analysis,” *Nature Methods*, vol. 14, no. 7, pp. 641–642, Jun. 2017, doi: 10.1038/nmeth.4346.

[15] H. Abdi and L. J. Williams, “Principal component analysis,” *Wiley Interdisciplinary Reviews: Computational Statistics*, vol. 2, no. 4, pp. 433–459, Jul. 2010, doi: 10.1002/wics.101.

[16] R. Wicklin, “Convergence in mixed models: When the estimated G matrix is not positive definite,” *The DO Loop*, Apr. 03, 2019.

Chapter 4: Final Experiments

4.1 Introduction

This chapter outlines the experiments employed to measure the effect of tension on the Raman signature of demineralized equine bone. Ultimately the goals are (1) to determine whether the Raman signature of demineralized bone changes with tensile loading, and if it does, (2) to use the results to explain the phenomenon of stress-induced whitening.

4.2 Materials

4.2.1 Specimen Preparation

As described in Section 3.2.1, cortical bone beam specimens were cut from the mid-diaphysis of the right third metacarpal bone (MC3) of a three-year-old Thoroughbred gelding euthanized due to a unilateral biaxial proximal sesamoid bone fracture of the left forelimb while in race-training. The horse was necropsied as part of the California Horse Racing Board's racing safety program [1].

A 100 mm long section was cut from the mid-diaphysis; the center of this section occurred at the proximodistal midpoint of the MC3 (Section 3.2.1; Figure 3.1). Rectangular prism (2x2x40mm) bone beams were cut from this section, while under constant irrigation with deionized (DI) water using a diamond-coated bandsaw (Exakt Technologies, Oklahoma City, OK, USA) and a custom-built specimen jig. Specimens were cut so that the beam was parallel with the proximodistal axis of the bone. Figure 3.1 (Section 3.2.1) indicates where the bone beam specimens originate from within the cross-section of the MC3 bone (see Appendix A1 for more details). Bone beams were individually stored in a Falcon tube containing 10 mL of saline (7 g NaCl/1 L DI H_2O) at -20°C. Samples were completely thawed in a refrigerator for 24 hours

prior to use in experiments. For the final experiments, seven bone specimens were used (n=7) with the following naming convention (where the number indicates the row and the color indicates the column): 9.3 Green, 9.3 Navy, 9.3 Red, 9.4 Black, 9.4 Green, 9.4 Navy, and 9.4 Red.

4.2.2 Demineralization

The central 5 mm of each bone beam was demineralized using a buffered [sodium citrate (100g/L)] formic acid (22.5% v/v) solution. This demineralization method was chosen because it maintains the integrity of the collagen network [2] and was successfully used for previous stress-whitening experiments in our laboratory [3], [4]. The proximal and distal ends of the bone beams (~17.5 mm each) were protected from demineralization by a coating of silicone sealant (Advanced Silicone 2, GE Sealants & Adhesives). The extent of demineralization was assessed using radiography (Dental Aire DTX) via visual inspection of x-ray transparency. Demineralization media was changed every 24 hours until full demineralization was reached (~72-96 hours). Successful demineralization was indicated by complete transparency in the central ~5mm of the bone beams. Appendix A2 outlines the demineralization protocol in more detail.

4.3 Methodology

4.3.1 Mechanical Testing

Tensile testing experiments were conducted using a micromechanical tester (ADMET, Norwood, MA, USA) designed to fit on the stage of an inverted confocal scanning upright microscope for simultaneous Raman spectral imaging. Samples were placed in the serrated clamp grips and grip displacement was driven by a motor (Faulhaber, Clearwater, FL, USA). The testing system was controlled by ADMET's PC-based MTESTQuattro controller (ADMET,

Norwood, MA, USA), which collected the mechanical data (i.e., position, load, temperature, etc.) during each of the mechanical tests. Synchronized force and elongation data were collected during each experiment at a sample rate of 20 samples/sec.

4.3.2 Raman Spectroscopy

Spectra were acquired using a custom-built inverted Raman scanning confocal microscope with an excitation wavelength of 785 nm and a 20x (NA=0.4) air immersion objective. Raman spectra were processed using Solis v4.31.30005.0 software in Dr. Randy Carney's laboratory (Appendix A8 details the experimental setup). Exposure time was set to 10 seconds per scan with a laser power of 67 mW; power was measured just prior to the objective.

4.3.3 Experimental Procedure

Each specimen underwent two experimental procedures. These procedures are outlined in Section 4.3.3a and 4.3.3b.

4.3.3a Sitting in Solution Test Procedure

This experiment was conducted to assess if any changes in the Raman spectrum of demineralized bone occur due to sitting in a saline solution. Demineralized bone beam specimens (n=7) were mounted with the mineralized ends of the beams secured in the grips. The grip separation was 31 mm, and the gauge length (demineralized portion of the specimen) was approximately 5 mm. The fluid bath was filled with saline solution (7 g NaCl/1 L DI H_2O). Raman data were collected every 20 minutes over the span of one hour (t=0, 20, 40, and 60 minutes). A 20x (NA = 0.4) objective was used on the microscope. One Raman spectral kinetic series of 30 ten second acquisitions (i.e., 30 individual spectra) were collected at each of the four time points. The temperature of the saline bath was measured using a hand-held infrared

thermometer (Model #800100, Sper Scientific, Scottsdale, AZ, USA) at each timepoint of the experiment.

4.3.3b Mechanical Test Procedure

This experiment was conducted to assess if any changes in the Raman spectrum of demineralized bone occur due to loading in tension. For each specimen, the Mechanical Test was conducted immediately after the Sitting in Solution Test. Specimens (n=7) were mounted with the mineralized ends of the beams secured in the grips. Specimens were loaded in tension at a constant strain rate of 0.001 s^{-1} to a nominal strain of 0.03 (calculated using the grip separation, i.e., displacement/31 mm). During characterization tests (Section 2.3), beams fractured at an approximate nominal strain of 0.045 (displacement/31 mm), so the end strain value (0.03) was chosen as the maximum for these experiments to induce stress-whitening without breaking the specimen. Tests were performed under displacement-control (which is defined by the software as "strain"-control; Section 2.1.4). After loading, the specimens were unloaded to zero strain at a displacement rate of 1 mm/sec. The mechanical test protocol was repeated three times for each specimen, with no delay between each mechanical test.

For each sample, Raman data were collected before the mechanical test (Unloaded condition, i.e., zero applied strain) and after the specimen was loaded in tension to a nominal strain of 3% (Loaded condition). The laser was refocused between the Loaded and Unloaded conditions to ensure that the laser was in the demineralized bone. A 20x (NA = 0.4) objective was used and one kinetic series of 30 ten second acquisitions (i.e., 30 individual spectra) were collected for each instance of data collection.

During each mechanical test (i.e., during tensile strain application) specimens were evenly illuminated at a ~45° angle from above using a ring light. The ring light was powered

down during the Raman spectral data collection. Video data of the 30 second mechanical test was captured using a Sony a7R camera (Sony, Tokyo, Japan). An external trigger was placed in the field of view and used to synchronize the video with the mechanical data. A color calibration card was obtained online (DGK Color Tools) and included a grayscale reference. The calibration card was printed using a laser printer, and the print quality was fine enough to suit the purpose of a correction factor. The grayscale calibration card was included in the field of view for reference and the black rectangle was used as a correction factor for the whitening calculations. The temperature of the saline bath was measured using a hand-held infrared thermometer (Model #800100, Sper Scientific, Scottsdale, AZ, USA) at the Unloaded and Loaded conditions for each of the three mechanical tests.

4.4 Data Reduction

The video data were used to calculate the stress-whitening of the bone beams (Section 4.4.1). The Raman data were pre-processed (Section 4.4.2) and subsequently analyzed for differences between treatment groups using Principal Component Analysis (PCA).

4.4.1 Video Data Reduction

As described in Section 3.4.1, stress-whitening was quantified using a custom macro run in ImageJ/Fiji (NIH, Bethesda, MD, USA). Briefly, stress-whitening was quantified by comparing the average pixel intensity of the rectangular region of interest (ROI) to the initial (pre-strained) pixel intensity of the ROI. The pixel intensity was corrected for using the black rectangle on the grayscale calibration card that was included in the frame for all videos. Refer to Section 3.4.1 for more details.

4.4.2 Raman Spectral Data Pre-processing

Spectral data processing was conducted using a custom MATLAB (MathWorks, Natick, MA, USA) program called "Noodle," from the Carney Lab (Randy Carney, UC Davis, unpublished) as described in Section 3.4.2. First, noise is minimized in the raw spectra using a Whittaker smoother with a value of 5. Second, smoothed spectra are background subtracted using airPLS (adaptive iteratively reweighted Penalized Least Squares) with a lambda value of $1x10^6$. Third, the spectra are unit normalized.

For the two test procedures (Sitting in Solution and Mechanical Test), the Raman spectra from each kinetic series for each test specimen and condition (t = 0, 20, 40 60 min *or* Unloaded, Loaded, respectively) were averaged. For the Sitting in Solution Test, there were a total of 28 data points (7 samples * 4 test conditions/sample = 28 data points total). For the Mechanical Test, there were a total of 42 data points (7 samples * 6 test conditions/sample = 42 data points total).

The grand averages of the Raman spectra of all samples for each test condition (t = 0, 20, 40 60 min *or* Unloaded, Loaded, respectively) were then calculated. Figure 4.1 (top) shows the grand averaged of the Unloaded and Loaded data from the Mechanical Test. Additionally, the grand averages were used to determine the mean Difference in Average Raman Intensity (dI) for Unloaded and Loaded data (Figure 4.1; bottom). The Difference in Average Raman intensity was calculated as: dI = Average Intensity Loaded – Average Intensity Unloaded (Figure 4.1; bottom; calculated using MATLAB).

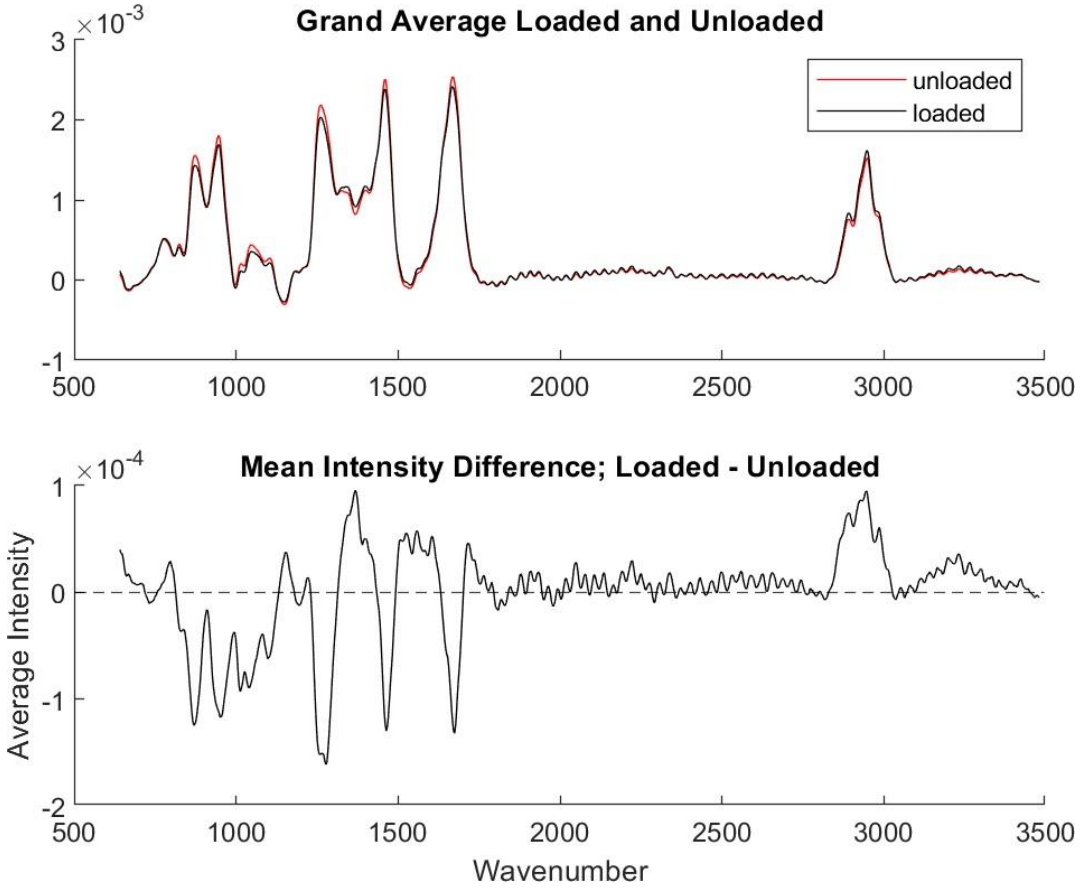

Figure 4.1: Top: Grand averages of the Unloaded (red) and Loaded (black) data from the Mechanical Test. **Bottom:** Mean intensity difference of the Loaded and Unloaded data.

4.4.3 Principal Component Analysis

As described in Section 3.4.3, PCA was performed using a custom MATLAB (MathWorks, Natick, MA, USA) program called "Noodle," written by the Carney Lab (Randy Carney, UC Davis, unpublished). The average processed Raman spectra (Section 4.4.2) from the seven specimens were used in the PCA.

To improve the signal-to-noise ratio, PCA was performed using the averages of each kinetic series from each condition of two test procedures (Sitting in Solution and Mechanical Test; see section 4.4.2). Principal component scores and loadings for the PCs accounting for ~90% of the variance were extracted for each test procedure.

4.5 Statistical Analysis

All statistical analyses were performed using SAS 9.4 (SAS Institute Inc., Cary, North Carolina, USA). A linear mixed model (LMM) was performed on the Sitting in Solution Test data to assess whether there is an effect of prolonged saline submersion on the Raman signature of demineralized bone (t=0, 20, 40, and 60 min). Univariate LMMs were performed on PC 1, PC 2, PC 3, and PC 4 scores; these are the PC scores that accounted for ~90% of the variance in the Sitting In Solution spectra data. In each LMM, the fixed effects were Timepoint (t=0, 20, 40, and 60 min) and Temperature and the random effect was Specimen ID.

Univariate LMMs was performed on the Mechanical Test data to assess whether there is an effect of mechanical loading PC Scores (Unloaded and Loaded). Univariate LMMs were performed PC 1, PC 2, PC 3, and PC 4 scores; these scores accounted for ~90% of the variance in the spectral data. For the Mechanical Test, the fixed effects were Condition (Unloaded or Loaded), Test Number (Test Number = 1, 2, or 3), the interaction of Condition and Test Number, and Temperature and the random effect was Specimen ID.

White value is defined as a relative measure between the Loaded and Unloaded Conditions. First, a LMM was performed on the white values from the Loaded condition to determine if Test number had a significant effect on the mean white value. Second, an intercept-only LMM was performed on the white values of the Loaded data to determine if the mean white value score (i.e., model intercept) was statistically different from zero (i.e., the Unloaded value). Specimen ID was used as a random effect in both LMMs.

All LMMs were performed in SAS 9.4 using the “proc mixed” function, with a p value of 0.05 considered significant. Shapiro-Wilk W-scores were used to check for residual normality ($W > 0.9$ indicated normal distribution of residuals). If the W-score did not pass ($W < 0.9$), then

those PC scores were ranked, and the p-value of the ranked PC's LMM was considered. When applicable, the differences of the Least Square Means were included in the mixed procedure to assess the model fixed effect means and comparisons (Tukey-Kramer adjustment; $p \leq 0.05$ significant). Additionally, for the Mechanical Test Data, a post hoc test for simple differences in Condition means and Test Number means was performed.

Linear regressions were performed to assess the relationship between PC Score and White Value (W). Three regressions were performed in total: the White Value being the dependent variable and the scores from each of the first three PCs being the independent variables. The p-values, model R-squared, and adjusted R-squared values were calculated for each independent variable. Note: the regression results should be interpreted with caution, since the white value is bounded on (0,1) which contradicts the linear regression assumption that the response variable (W) is unbounded.

4.6 Results

Tables 4.1 and 4.2 provide a breakdown of the spectral variance accounted for by the first 10 PCs for the Sitting in Solution and Mechanical Test data, respectively.

Table 4.1: Spectral variance in the Sitting in Solution Test Raman spectral data, accounted for by the first 10 principal components. The first four PCs (bolded) account for >90% of the variance in the spectral data.

Principal Component	Percent Variability	Cumulative Variability
PC 1	**59.34%**	**59.34%**
PC 2	**24.06%**	**83.40%**
PC 3	**6.55%**	**89.95%**
PC 4	**2.71%**	**92.66%**
PC 5	1.97%	94.63%
PC 6	1.43%	96.06%
PC 7	0.85%	96.91%
PC 8	0.64%	97.56%
PC 9	0.46%	98.02%
PC 10	0.36%	98.38%

Table 4.2: Spectral variance in the Mechanical Test Raman spectral data, accounted for by the first 10 principal components. The first four PCs (bolded) account for >90% of the variance in the spectral data.

Principal Component	Percent Variability	Cumulative Variability
PC 1	**53.08%**	**53.08%**
PC 2	**19.53%**	**72.61%**
PC 3	**11.86%**	**84.46%**
PC 4	**5.68%**	**90.14%**
PC 5	3.66%	93.81%
PC 6	1.94%	95.75%
PC 7	0.86%	96.61%
PC 8	0.64%	97.25%
PC 9	0.54%	97.79%
PC 10	0.36%	98.14%

Figure 4.2 is a 3-dimensional plot of the first three PCs for the Mechanical Test data. Figure 4.3 contains 2-dimensional plots of the Mechanical Tests data PC 1 plotted against PC 2, PC 3, PC 4, and PC 5, respectively. The loading plots of the first two PCs are shown in Figure 4.4.

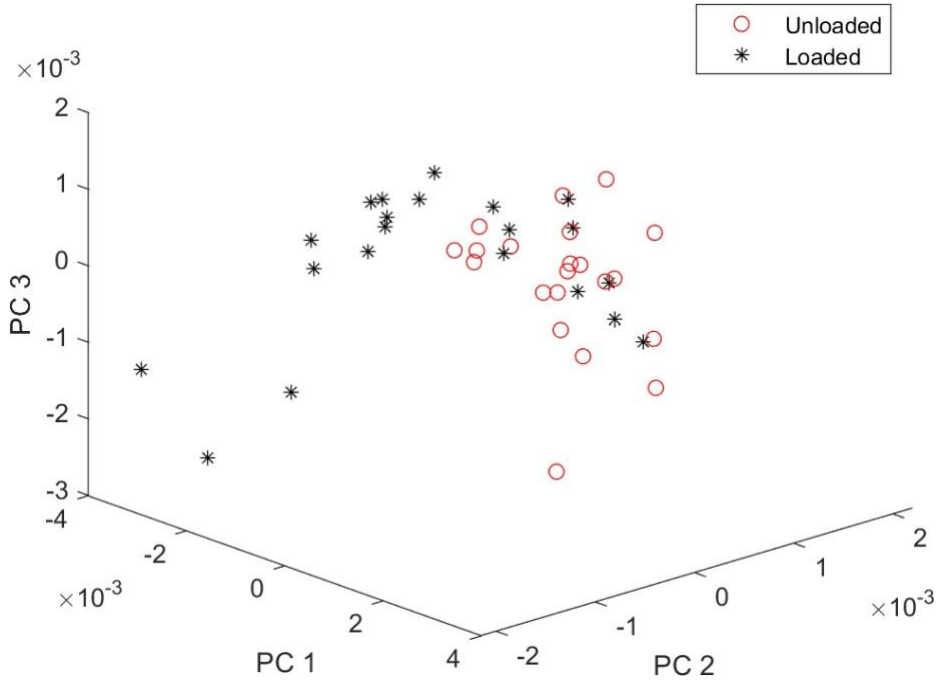

Figure 4.2: For the mechanical test data, Three-dimensional plots of the PC scores from the first three PCs plotted against each other. Unloaded data is indicated by red circles and Loaded data is indicated by black asterisks.

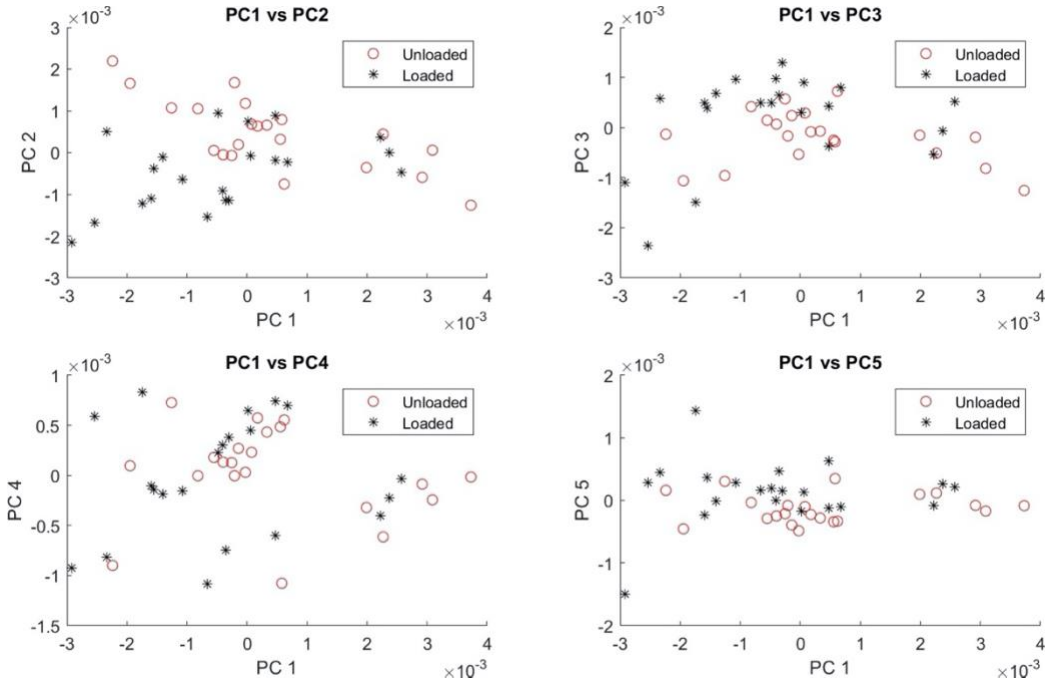

Figure 4.3: Two-dimensional plots of the scores from the primary PCs plotted against PC 1 scores for the Mechanical Test data. Unloaded data is indicated by red circles and Loaded data is indicated by black asterisks.

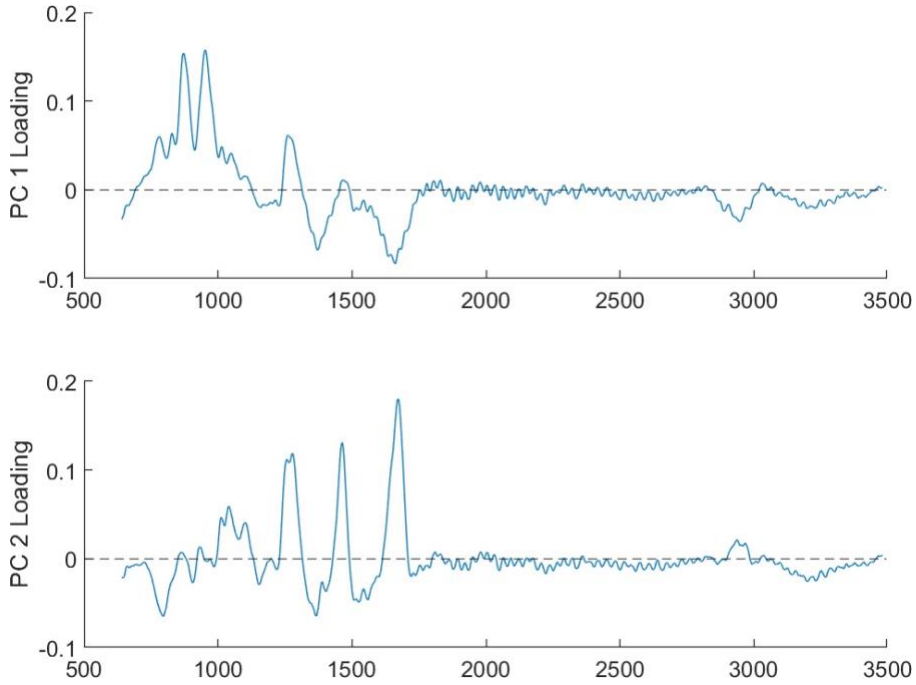

Figure 4.4: PC 1 and PC 2 loading plots for the Mechanical Test data.

4.6.1 Sitting in Solution Test

Timepoint (i.e., t=0, 20, 40, or 60 min) was not significant for PC 1, PC 2, or PC 4, however it was significant for PC 3 (see Table 4.3 for p values). Percent variability accounted for by the first ten PCs is show in Table 4.1. The one statistically significant effect was in PC 3, which shows timepoint t=0 min being different from the other timepoints (i.e., t=20, 40, and 60 min) and t=20 min being different from t=60 min (Table 4.4). The first four PCs account for ~93% of the variability within the Raman spectral data. Since PC 3 was only responsible for 6.5% of the total variance in the data, the significance found for the timepoints in this PC does not have a large influence on the data.

Table 4.3: Results of the linear mixed model for the Sitting in Solution Test. *Significance $p<0.05$.

Dependent Variable	Effects	P-Value for Type 3 Test of Fixed Effect	Shapiro-Wilks Score (W)
PC 1	Timepoint	0.6415	0.91
PC 2 (ranked)	Timepoint	0.1314	N/A
PC 3	Timepoint	< 0.0001*	0.97
PC 4	Timepoint	0.3737	0.95

Table 4.4: Differences of Least Square Means (standard error) of PC scores for the "Sitting in Solution Test." In each column, LS means that share a superscript (A, B, C) are not significantly different at $p \leq 0.05$.

Timepoint	PC 1	PC 2	PC 3	PC 4
t = 0	-0.02001 (0.01436) ^{A}	0.002736 (0.004162) ^{A}	-0.00056 (0.000108) ^{A}	0.007374 (0.004122) ^{A}
t = 20	-0.02044 (0.01451) ^{A}	0.002681 (0.004206) ^{A}	0.000084 (0.000108) ^{B}	0.007310 (0.004166) ^{A}
t = 40	-0.02034 (0.01440) ^{A}	0.002454 (0.004175) ^{A}	0.000133 (0.000108) $^{B, C}$	0.007216 (0.004135) ^{A}
t = 60	-0.02047 (0.01445) ^{A}	0.002375 (0.004189) ^{A}	0.000341 (0.000108) ^{C}	0.007216 (0.004149) ^{A}

4.6.2 Mechanical Test

4.6.2a Stress-whitening

A representative photo of a demineralized bone specimen in the Unloaded state (not whitened) and Loaded state (whitened) is shown in Figure 4.5. The average whitening (AW)

value for each specimen, over all three tests, is shown in Figure 4.6. The AW for each bone specimen increased monotonically with strain. Two of the specimens (i.e., 9.3 Navy and 9.3 Red) experienced an initial darkening (as shown by the negative values) and then began whitening at about 0.007 strain. All other specimens started whitening immediately when loaded. The maximum final AW value was 0.67 (specimen 9.4 Navy) and the minimum final AW value was 0.12 (specimen 9.3 Navy). A linear trendline with an R^2 value of 0.9114 was fit to the AW for all the bone specimens (shown in red on Figure 4.6).

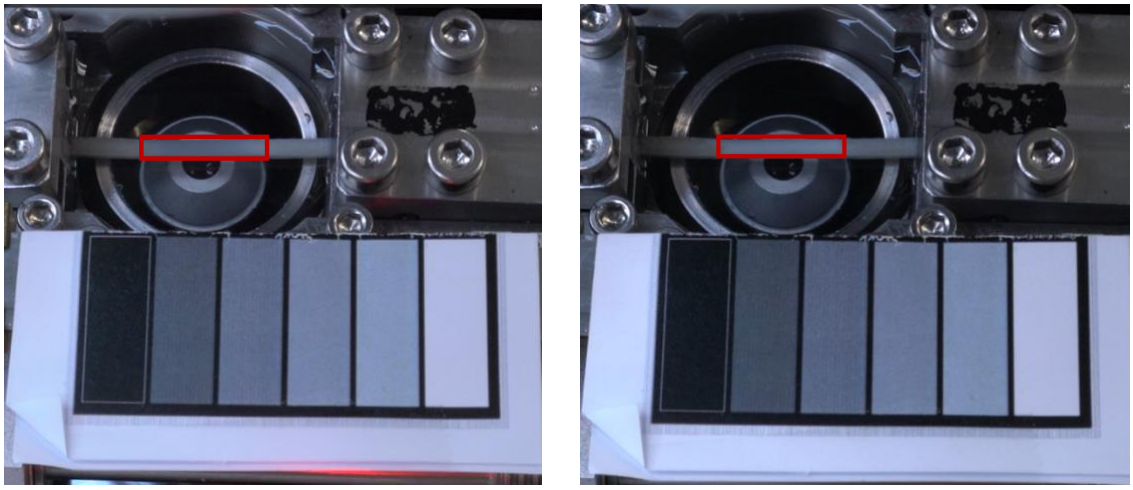

Figure 4.5: Comparison of a demineralized bone specimen in the Unloaded state (left) and the Loaded state (right). Bone beam ROI indicated by a red rectangle.

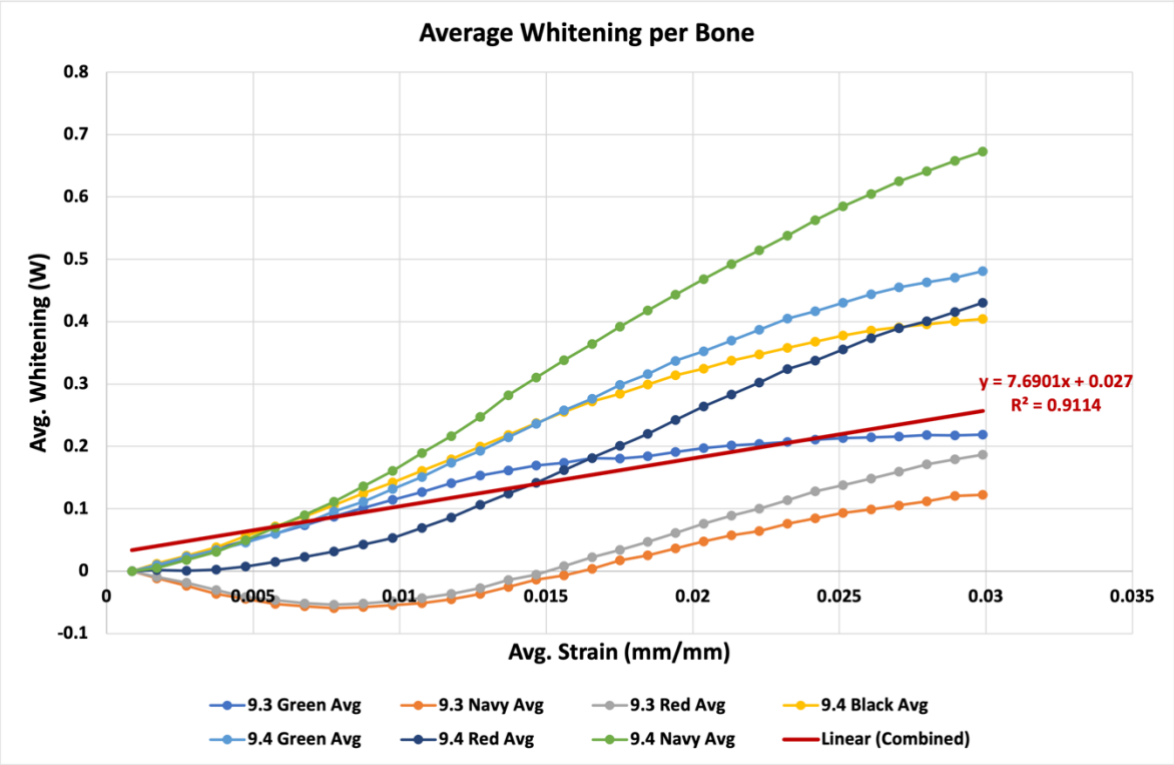

Figure 4.6: Average of whitening of all three mechanical tests for each specimen (n=7) plotted against average strain.

The grand average of stress-whitening is shown in Figure 4.7 and follows the same trend as the individual whitening curves (Figure 4.6). There is an initial toe region in the plot of the grand average of whitening, indicating that some amount of strain is required to initiate whitening. The average final whitening value was 0.36. Overall, apparent whitening was nonlinear and increased monotonically with strain.

Test number did not have a significant effect on mean white value ($p = 0.1728$). The mean white value for the Loaded Condition was significantly different from zero ($p = 0.0027$). The LMM's estimate for the white value (i.e., model intercept) was 0.359 +/- 0.07.

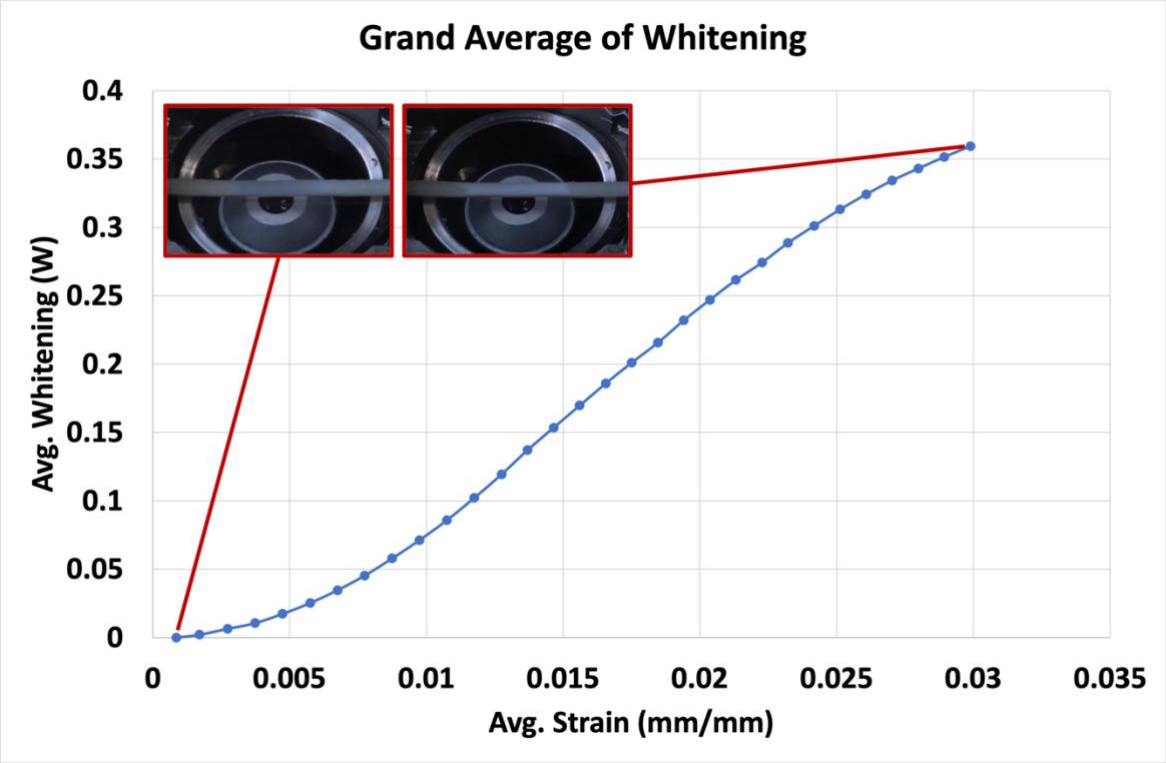

Figure 4.7: Grand average of whitening for all specimens (n=7) plotted against average strain.

4.6.2b Raman Spectral Data

Condition (Unloaded or Loaded) had a significant effect on PC 1 ($p = 0.0122$) and PC 2 ($p = 0.0019$), and PC 3 ($p = 0.0278$), but not PC 4 ($p = 0.6712$). Test Number, the interaction of Condition and Test Number, and Temperature were not found to be significant for PC 1, PC 2, PC 3, or PC 4 (Table 4.5). As shown in Figures 4.2 and 4.3, these four principal component scores were generally separated based on Condition.

Table 4.5: Results of the linear mixed model for the Mechanical Test. *Significance p<0.05.

Dependent Variable	Effect	P-value for Type 3 Effect	W Score for Residual Normality
PC 1	Condition	0.0122*	0.9855
	Test Number	0.2535	
	Condition*Test Number	0.4792	
	Temperature	0.8317	
PC 2	Condition	0.0019*	0.9875
	Test Number	0.2003	
	Condition*Test Number	0.1108	
	Temperature	0.0821	
PC 3	Condition	0.0278*	0.9173
	Test Number	0.1115	
	Condition*Test Number	0.1301	
	Temperature	0.2612	
PC 4	Condition	0.6712	0.933
	Test Number	0.24	
	Condition*Test Number	0.2442	
	Temperature	0.8847	

The simple differences in the Least Square Means of the principal component scores (Table 4.6) indicate that Condition was only significant for one of the three tests (Test 1, 2, or 3), in PC 1, PC 2, and PC 3. Because Condition had an overall effect on the mean principal component scores, some of the similarities in this post hoc test are perhaps due to the relatively small sample size.

Table 4.6: Least Square Means (standard error) of principal component scores from the LMM of the Mechanical Test. Across a row, simple differences in Condition means are indicated by subscripts (a, b). Down a column, simple differences in the Test Number means are indicated by superscripts (A, B, C). Significance was set at $p \leq 0.05$.

PC 1		
	Unloaded	Loaded
Test 1	0.000424 (0.000625) $_{a}$ ^{A}	0.000039 (0.000619)$_{a}$ ^{A}
Test 2	0.000462 (0.000613)$_{a}$ ^{A}	-0.00027 (0.000614)$_{a}$ ^{A}
Test 3	0.000303 (0.000613)$_{a}$ ^{A}	-0.00096 (0.000613)$_{b}$ ^{A}
PC 2		
	Unloaded	Loaded
Test 1	0.000109 (0.00033)$_{a}$ ^{A}	-0.00057 (0.000323)$_{a}$ $^{A, B}$
Test 2	0.00041 (0.000316)$_{a}$ ^{A}	0.000146 (0.000318)$_{a}$ ^{A}
Test 3	0.000684 (0.000317)$_{a}$ ^{A}	-0.00078 (0.000316)$_{b}$ ^{B}
PC 3		
	Unloaded	Loaded
Test 1	0.000074 (0.000295)$_{a}$ ^{A}	0.000475 (0.000289)$_{a}$ ^{A}
Test 2	-0.00054 (0.000285)$_{a}$ ^{A}	0.000393 (0.000286)$_{b}$ $^{A, B}$
Test 3	-0.0002 (0.000285)$_{a}$ ^{A}	-0.00021 (0.000285)$_{a}$ ^{B}
PC 4		
	Unloaded	Loaded
Test 1	-0.00001 (0.000209) $_{a}$ ^{A}	0.000243 (0.000205) $_{a}$ ^{A}
Test 2	0.000197 (0.000201) $_{a}$ ^{A}	-0.00011 (0.000202) $_{a}$ ^{A}
Test 3	-0.0001 (0.000201) $_{a}$ ^{A}	-0.00022 (0.000201) $_{a}$ ^{A}

Linear regressions predicting peak whitening at 3% nominal strain were performed using the scores from each of the first three principal components. Using both Loaded and Unloaded data, White Value was found to decrease with the PC 2 score ($p=0.0009$; $R^2 = 0.24$), but not the PC 1 score ($p=0.4576$) or the PC 3 score ($p=0.0611$). Table 4.7 contains the results from the linear regressions; note that the regressions do not account for variation within Sample ID. The plots of the linear regressions with the first three PCs are shown in Figure 4.8. The model R-squared values indicate that PC 2 was the best predictor of white value (Table 4.7 and top right panel of Figure 4.8).

Table 4.7: Results from the regressions (independent variables = PC 1-4 scores; dependent variable = white value).

Independent Variable	Model Parameter	DF	Parameter Estimate	Standard Error	t Value	Pr > |t|	Model R-Squared
PC 1	Intercept	1	0.17970663	0.03545051	5.07	<.0001	0.0139
	PC1_score	1	-16.8504227	22.46374169	-0.75	0.4576	
PC 2	Intercept	1	0.1797066	0.03104153	5.79	<.0001	0.2439
	PC2_score	1	-116.492754	32.4297517	-3.59	0.0009	
PC 3	Intercept	1	0.17970663	0.03414909	5.26	<.0001	0.0849
	PC3_score	1	88.23247199	45.78792404	1.93	0.0611	

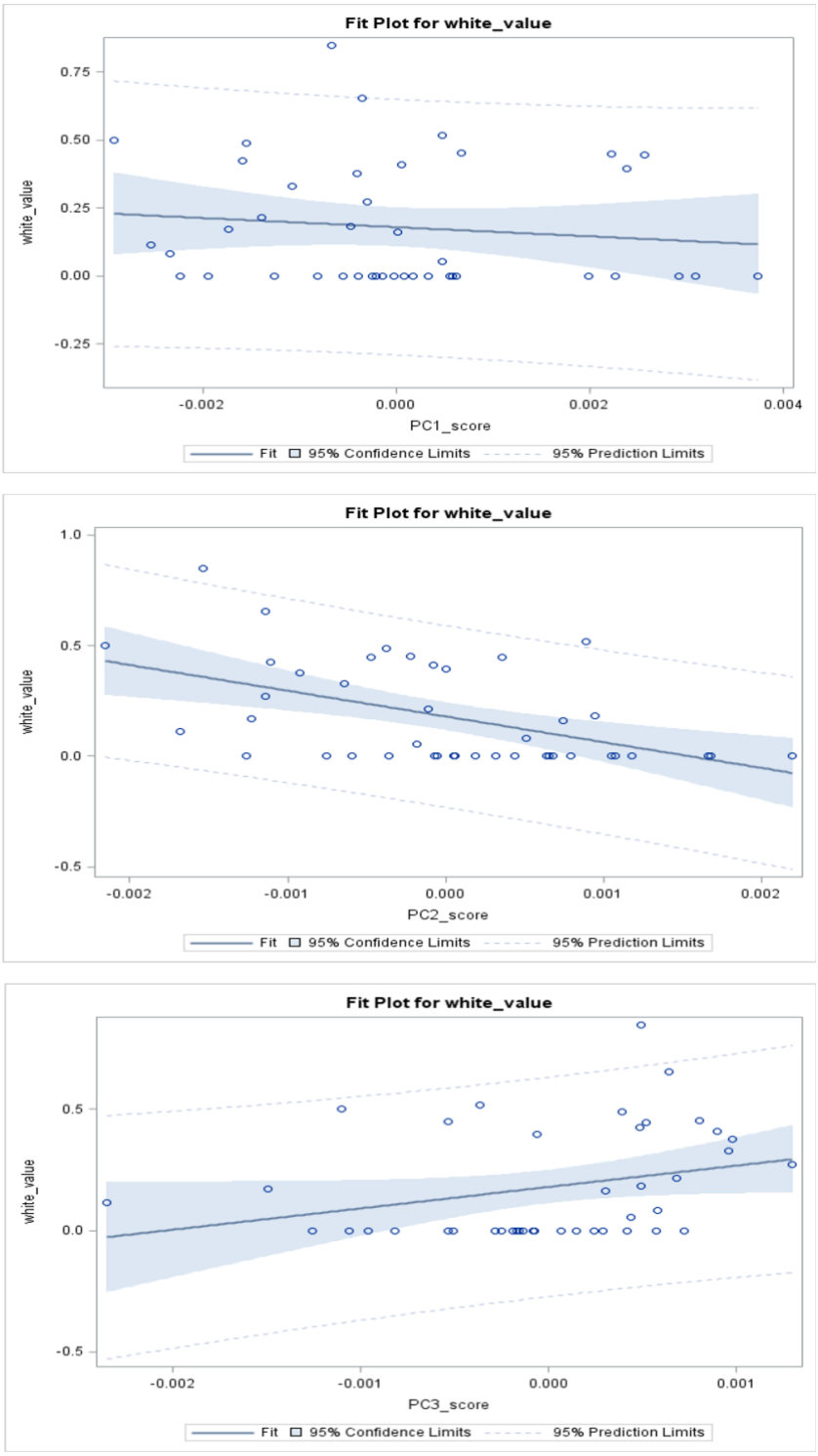

Figure 4.8: Results of the linear regression performed on the scores from the first three principal components of the Mechanical Test data. **Top:** PC 1 Score v. White Value. **Middle:** PC 2 Score v. White Value. **Bottom:** PC 3 Score v. White Value.

There were peak intensity differences between the grand averages of the Unloaded and Loaded Raman spectra when overlayed (Figure 4.1; top). These differences are made clear by plotting the mean intensity difference (Loaded – Unloaded), as shown in the bottom panel of Figure 4.1. The peaks that changed with loading are indicated in the figure, including proline (866.8 cm^{-1}), hydroxyproline (954 cm^{-1}), amide III (1280 cm^{-1}), CH_2 (1467 cm^{-1}), amide I (1671 cm^{-1}), and CH-stretch (2949 cm^{-1}). The only peak that increased in intensity upon loading was the CH-stretch peak, whereas all other peak intensities decreased upon loading. As illustrated by Figure 4.4, these spectral differences were picked up by PC 2.

4.7 Discussion

4.7.1 Sitting in Solution Test

Raman spectral data were collected every 20 minutes over a one-hour period to measure any changes in the demineralized bone beam that might result from sitting in saline solution. Generally, there were no effects of time in solution on the Raman spectrum. We did not detect a difference in PC 1 or PC 2 scores over time and these two scores account for 83.4% of total variance. Timepoint (i.e., t=0, 20, 40, or 60 min) did have a significant effect on PC 3; however, PC 3 only accounts for 6.5% of the total variance in the data. Thus, we conclude that the Raman signal of demineralized bone is generally stable when sitting in saline for one hour.

4.7.2 Mechanical Test

Demineralized bone beam specimens were loaded in tension to a point of stress-whitening. Significant whitening was observed in all specimens and increased monotonically with strain. Statistically significant changes in the PC scores of Raman spectra were measured for the mechanically tested specimens. Specifically, Condition (Unloaded or Loaded) had a significant effect on the scores of the first three principal components.

Analysis of the PC loading plots enables the determination of the peak intensity changes associated with individual PCs. The loading plot of PC 1 (Figure 4.4; top) reveals that all the peaks identified by plotting the mean intensity difference (Figure 4.1; i.e., proline, hydroxyproline, amide III, CH_2, amide I, and CH-stretch) also strongly influence PC 1 and thus contribute to 53% of the total variation in the spectral data. Furthermore, the PC 2 loading plot (Figure 4.4; bottom) reveals that the magnitudes of the amide III, CH_2, and amide I peak intensity changes are two times as great, in comparison to the other peaks on the loading plot. Therefore, amide III, CH_2, and amide I most strongly influence PC 2 and are responsible for ~20% of the total variation of the data.

The results of the linear regression indicate that White Value decreases with the PC 2 score. Therefore, we hypothesize that PC 2 captures the variation in the Raman spectrum that caused by stress-whitening. This hypothesis is supported by the loading plot PC 2 (Figure 4.4; bottom), which show that PC 2 is primarily influenced by changes in the spectrum of the amide III (~1243-1320 cm^{-1}), CH_2 (~1450 cm^{-1}), and amide I (~1616-1720 cm^{-1}) bands. The shape of the loading plot of PC 2 also mirrors the dI at ~1243-1320 cm^{-1}, ~1450 cm^{-1}, and ~1616-1720 cm^{-1}. At these wavenumbers, the amide III, CH_2, and amide I peaks decreased with loading. Additionally, there was variation in the white value reached by the samples during repeated mechanical loading (although this variation was not statistically different). A LMM performed on the data (with Sample ID as a random effect) indicated that within each sample, lower white values (i.e., less whitening) were associated with higher PC 2 scores. Overall, these results imply that PC 2 represents the variation in the Raman spectrum of demineralized bone that is associated with stress-whitening.

Other laboratories have shown that the amide III, CH_2, and amide I peaks are associated with the protein structure of type I collagen in bone and have developed peak intensity ratios which indicate the state of the protein structure [5]. Specifically, these groups have shown that the CH_2 peak represents the total amount of collagen in the material [5]. Moreover, the ratio of the intensity of the CH_2 peak and intensities of the subpeaks from the amide III band (~1245 cm^{-1} and ~1320 cm^{-1}) have been used to assess collagen quality [5]. Taken together, the results of the current study show that stress-whitening is associated with changes in the protein structure of demineralized bone, which is captured as changes in the peak intensities of the amide III, CH_2, and amide I bands in the Raman spectrum.

4.7.3 Limitations

There are several limitations of this study that should be addressed. First, equipment failure limited the level of control of the experiments. The temperature controller was inoperable during the time of testing; therefore, temperature of the fluid bath could not be controlled. Additionally, the mechanical tester was unable to accurately measure load (see Section 2.1.5), so load and stress data were not included in the study. There were also limitations which may be attributed to the interaction of the mechanical tester and the Raman system. The mechanical tester rested at a slight angle on the Raman microscope platform, so the laser beam did not enter the demineralized bone specimens at exactly 90°. Additionally, the laser must be cooled to -60°C prior to taking Raman measurements, and because the laser cannot be powered on during the mechanical test, the laser must be powered on and allowed to cool before collecting Raman data of the Loaded specimen. Therefore, the Loaded specimen is held in tension for about eight minutes before the Loaded Raman data is collected, which might allow for specimen stress-relaxation and potential loss of whitening. In future experiments, video data will include from the

start of the mechanical test up to Raman data collection to assess if stress-relaxation and loss of whitening occurs during that period.

There was also limitation inherent to the specimens used in the study. All bone beam specimens used for the final experiments originated from the dorsomedial quadrant of the third metacarpal (MC3) bone. Compared to the lateral regions of the MC3, the medial region has been shown to experience the most remodeling in Thoroughbred racehorses [6]. This increased bone turnover of the medial quadrant might potentially affect the mechanical properties and might be important to consider when interpreting these results. Also, all specimens originated from the same donor, meaning variation between bones from different donor horses was not captured.

Finally, there is limitation inherent in the white value calculations. The equation used to calculate white value always causes the white value of the specimen in the unloaded condition to be zero. A white value of zero may be problematic in the linear regression. In the future, the black rectangle on the calibration card will be used to determine a calibration equation, which will then be used to calculate white value. This method of white value calculation would yield non-zero white values for the unloaded condition, which more accurately represent the "whiteness" of the specimen.

4.8 Summary

The results of this study indicate that the Raman signal of demineralized bone specimens submerged in saline solution is stable over one hour. Specimens that are loaded in tension to 3% nominal strain stress-whiten. Condition (Unloaded or Loaded) had a significant effect on the scores of the first three principal components of the Raman spectrum (PC 1, PC 2, and PC 3). The scores from PC 2 are significantly affected by the magnitude of whitening, and therefore changes in PC 2 reflect the effect of stress-whitening on the Raman spectrum of demineralized

bone. Taking Unal et. al.'s results [5] into consideration, it is apparent that the peak intensity changes in the amide III, CH_2, and amide I regions of the Raman spectral data caused by changes in collagen structure are directly associated with demineralized bone stress-whitening.

References

[1] JD Wheat Veterinary Orthopedic Laboratory, “Equine Health Research,” 2021. https://vorl.vetmed.ucdavis.edu/research-programs/equine-health-research (accessed Mar. 21, 2022).

[2] Y. N. Yeni, M. B. Schaffler, G. Gibson, and D. P. Fyhrie, “Prestress due to dimensional changes caused by demineralization: A potential mechanism for microcracking in bone,” *Annals of Biomedical Engineering*, vol. 30, no. 2, pp. 217–225, 2002, doi: 10.1114/1.1451078.

[3] M. R. Hardisty, T. C. Garcia, S. Choy, J. Dahmubed, S. M. Stover, and D. P. Fyhrie, “Stress-whitening occurs in demineralized bone,” *Bone*, vol. 57, no. 2, pp. 367–374, Dec. 2013, doi: 10.1016/j.bone.2013.08.029.

[4] M. R. Hardisty, M. A. Soicher, T. C. Garcia, S. M. Stover, and D. P. Fyhrie, “Do stress-whitening and optical clearing of collagenous tissue occur by the same mechanism?,” *Journal of Biomechanics*, vol. 46, no. 14, pp. 2411–2418, Sep. 2013, doi: 10.1016/j.jbiomech.2013.07.026.

[5] M. Unal, H. Jung, and O. Akkus, “Novel Raman Spectroscopic Biomarkers Indicate That Postyield Damage Denatures Bone’s Collagen,” *Journal of Bone and Mineral Research*, vol. 31, no. 5, pp. 1015–1025, May 2016, doi: 10.1002/jbmr.2768.

[6] R. B. Martin, S. M. Stover, V. A. Gibson, J. C. Gibeling, and L. v. Griffin, “In vitro fatigue behavior of the equine third metacarpus: Remodeling and microcrack damage analysis,” *Journal of Orthopaedic Research*, vol. 14, no. 5, pp. 794–801, 1996, doi: 10.1002/jor.1100140517.

Chapter 5: Conclusions

5.1 Summary

The aim of this thesis was to use Raman spectroscopy to determine the molecular mechanism of the bone stress-whitening phenomenon. Specifically, it was hypothesized that stress-whitening was a physical indication of the transition of bound-water to free-water in the collagen phase of the bone. A hydrogen/deuterium (H/D) exchange technique was proposed to track the movement of water within the demineralized bone specimens during tensile testing. Ultimately the H/D exchange was found to be an unreliable method of tracking water movement, using our Raman scanning confocal microscope. However, significant Raman peak intensity changes were found in the fingerprint region (peaks associated with bone matrix molecules; ~400-1800 cm^{-1}) of the Raman spectrum at 3% nominal strain.

The results confirm that the stress-whitening phenomenon occurs in demineralized equine bone. Further, the results of the Raman spectral data collection demonstrated an effect of mechanical loading on the protein structure of bone, that change the amide III (1280 cm^{-1}), CH_2 (1467 cm^{-1}) and amide I (1671 cm^{-1}) peaks of the Raman spectrum. The score of the second principal component (PC 2) was shown to be significantly affected by stress-whitening. Unal et. al. demonstrated that the Raman peak intensity ratios of the CH_2 and amide III regions are associated with changes in the conformation of the type I collagen in bone [1]. Taken together, our results show that stress-whitening of demineralized equine bone is related to a change in the conformational state of the organic phase. This change in the conformational state of the organic phase of demineralized bone might be indicative of increased ordering of the collagen molecules. Since 1928, it has been known that mechanical tension can cause increased ordering of collagen

molecules (i.e., increased crystallization) [2]. We hypothesize that the changes in Raman signal that were observed in this study are caused by mechanically induced increases in collagen order/crystallization that in turn causes bone collagen whitening.

5.2 Limitations and Future Directions

It is important to acknowledge the limitations of this work when considering the future directions. The primary limitations that should be ameliorated in future studies are the mechanical equipment malfunctions. Specifically, the issues of the inoperable temperature controller and malfunctioning mechanical tester should be addressed before more work is completed. Because the temperature controller was broken during the time of testing, differences in the temperature of the saline bath were included in the statistical model. Temperature was included as an effect when performing the linear mixed models (LMM) on the final experimental data, however in the future it would be best to control the temperature since it will influence the mechanical properties of the bone. Additionally, the design flaw in the mechanical tester that caused incorrect load measurements must be ameliorated if load and stress data are to be used in future studies. Specifically, it would be useful to know how whitening changes with stress.

Another limitation of the current study is that all bone beam specimens manufactured for this research originated from one equine donor. Therefore, results from this study cannot represent a population of equine bone, and this should be considered when interpreting the results. In the future, bone specimens will be fabricated from a larger population of donor horses to account for intra-species variations that might be present in the bone. Moreover, all bone beam specimens used for the final experiments originated from the proximal medial quadrant of the third metacarpal (MC3) bone. Cortical bone in the medial region of the equine MC3 bone of Thoroughbred racehorses has been shown to experience the most remodeling (compared to the

lateral and dorsal regions) [3]. Thus, there might be some effect on the mechanical properties of bone beams originating from the cortices of the medial region due to the increased bone turnover. Another set of experiments following the same protocols performed on demineralized bone specimens that originate from the lateral and dorsal regions of MC3 bone, and from different donor horses, would be useful to expand the application of this research.

All the experiments reported in this thesis were performed on demineralized bone. Hence the quantitative results are not representative of normal (un-demineralized) bone. Though the equine third metacarpal bone is similar in structure to the long bones of a human and served as an appropriate model for this exploratory study, it could be useful to repeat these experiments using bones from a human donor for a more convincing clinical relevance. However, since type I collagen and bone matrix are so strongly similar across many species with bones [4], the results would be strongly expected to be essentially identical to the present results.

Aside from overcoming the equipment limitations, the next step of this work is to follow the methods of Unal et. al. to quantify the peak intensity ratios of the protein regions of the demineralized bone, unloaded and loaded [1]. These results will provide more detail as to what conformational changes occur during stress-whitening. It is predicted that changes in the peak intensity ratios of the amide III and amide I regions upon loading will indicate a shift from an unordered state (i.e., random coil) to an ordered state of the type I collagen. This observation would further support the hypothesis that whitening coincides with stress-induced densification of the collagen fibrils, following the polymer-in-a-box theory.

5.3 Impact

This research augments our understanding of the ultrastructural mechanisms of bone mechanics and, furthermore, has the potential to supplement the understanding of bone diseases

associated with changes in molecular mechanics, such as osteogenesis imperfecta [5]. As time progresses, Raman spectroscopy is being further recognized for its benefits of contact-free and label-free imaging, and researchers are investigating its power in a clinical setting. Using Raman spectroscopy in a clinical setting to measure the chemical constituents of bone may inform clinicians of the structural integrity of the bone and risk of bone disease.

References

[1] M. Unal, H. Jung, and O. Akkus, “Novel Raman Spectroscopic Biomarkers Indicate That Postyield Damage Denatures Bone’s Collagen,” *Journal of Bone and Mineral Research*, vol. 31, no. 5, pp. 1015–1025, May 2016, doi: 10.1002/jbmr.2768.

[2] Janet H. Clark, “Reversible Crystallization In Tendons and Its Functional Significance,” 1928. doi: 10.1073/pnas.14.7.526.

[3] R. B. Martin, S. M. Stover, V. A. Gibson, J. C. Gibeling, and L. v. Griffin, “In vitro fatigue behavior of the equine third metacarpus: Remodeling and microcrack damage analysis,” *Journal of Orthopaedic Research*, vol. 14, no. 5, pp. 794–801, 1996, doi: 10.1002/jor.1100140517.

[4] G. M. Erickson, J. Catanese, and T. M. Keaveny, “Evolution of the biomechanical material properties of the femur,” *Anatomical Record*, vol. 268, no. 2, pp. 115–124, Oct. 2002, doi: 10.1002/ar.10145.

[5] A. Gautieri, S. Vesentini, A. Redaelli, and M. J. Buehler, “Osteogenesis imperfecta mutations lead to local tropocollagen unfolding and disruption of H-bond network,” *RSC Advances*, vol. 2, no. 9, pp. 3890–3896, Apr. 2012, doi: 10.1039/c2ra01047j.

APPENDIX

A1: Bone Beam Fabrication Protocol

Materials

- Equine cannon bone (3rd metacarpal)
- Permanent marker

Procedure

Preparing the bone for cutting

Obtain an equine cannon bone (third metacarpal bone, MC3) from the necropsy suite in the Veterinary Medicine 3A (Vet Med 3A) building. The bone should be clean, meaning there is no periosteum remaining on the outer surface of the bone. If the periosteal membrane is intact, remove it using a scalpel and tweezers.

Identify the proximal and distal ends of the cannon bone. The proximal end of the bone can be identified by locating the tuberosity on the dorsal surface. The distal end of the bone can be identified by locating the three ridges that protrude on the surface. Use the middle (sagittal) ridge of the distal end to estimate the midline of the bone and mark it using permanent marker. Identify the point equidistant from the proximal and distal ends and mark with permanent marker. Measure 50 mm away from either side of this point and mark, leaving a 100 mm segment of bone in the middle of the long bone between the proximal and distal ends (Figure A.1; left).

Cutting the bone into sections

Using the bandsaw in the Anatomy Department (contact Danielle McDonald for training), make cuts in the transverse plane to remove the proximal and distal ends of the cannon bone, leaving the 100 mm section in the middle (Figure A.1; right). Mark the lateral and dorsomedial regions of the bone to keep track. Make a lengthwise cut in the sagittal plane to separate the lateral and medial halves. Cut both the lateral and medial halves in the transverse plane to make a total of four 50 mm sections. Cut each of these sections in half in the dorsal plane. This process yields eight sections of cortical bone, each 50 mm long. Throughout this process, the bone marrow may be removed, leaving cortical bone. To store the bone sections for later use, wrap in a saline-soaked towel and store at -20ºC in an airtight freezer bag (i.e., Ziploc bag).

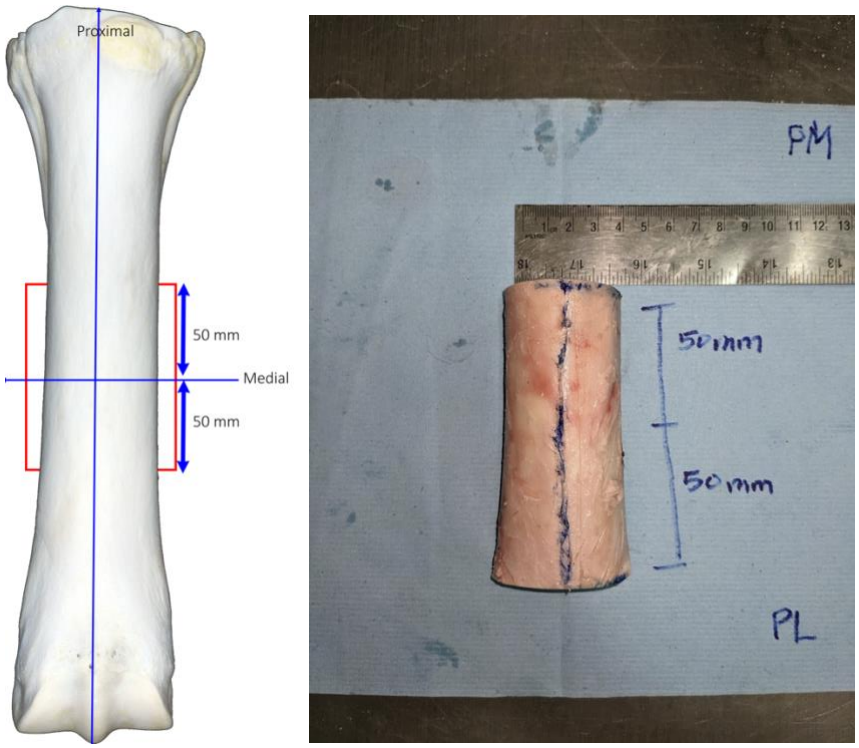

Figure A.1: Left: Graphic of an MC3 bone with the central 100 mm marked for reference. **Right:** Both the proximal and distal ends have been removed, leaving the 100 mm segment ready for further sectioning.

Cutting bone sections into beams

To cut the sections into beams, one must be trained on the diamond-coated bandsaw (Exakt Technologies, Oklahoma City, OK, USA) in Vet Med 3A Room 2404 (contact Tanya Garcia-Nolen for training). Prior to cutting, mark the bone segment at 40 mm for reference during cutting (this will be the final length of the bone beams) (Figure A.2; left). Secure the end of the bone section in the custom jig such that the 40 mm section is protruding and available for cutting (Figure A.2; right). Secure the jig into the moving arm of the bandsaw and adjust such that one end of the bone section is flush against the bandsaw blade. Proceed making 2 mm wide cuts across the width of the bone section, each 40 mm deep (use the marking for visual reference). Note: 25 turns of the knob are equivalent to 2 mm movement of the specimen. After the first pass of cuts, turn the bone section 90° and proceed making another pass of 2 mm cuts across the width of the bone. The result should be a checkered pattern of 2x2 mm cuts that travel 40 mm deep into the bone section.

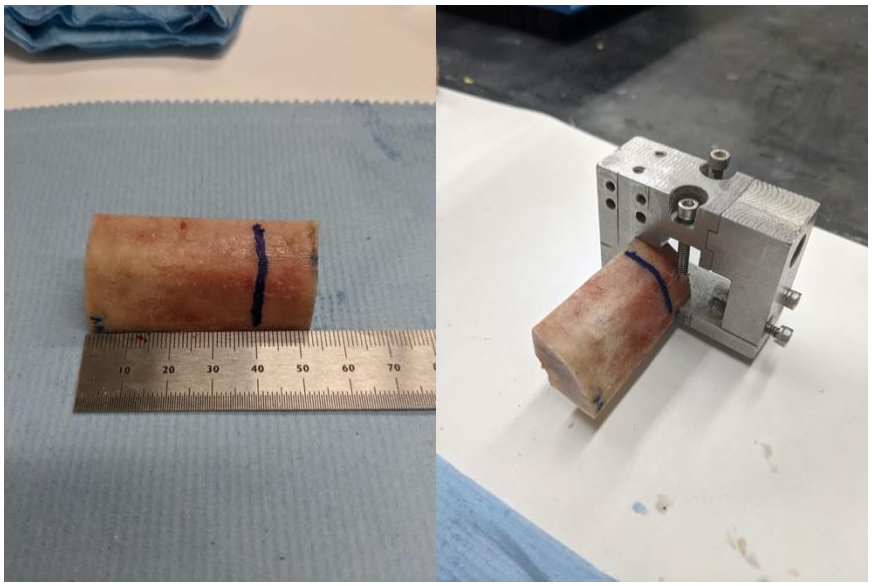

Figure A.2: Left: Bone section (~50 mm long) marked at 40 mm to guide depth of cuts with the bandsaw. **Right:** Bone section secured in the jig for cutting.

Prior to making the final cut, the beams of interest for testing must be marked for future reference (Figure A.3; left). Use multiple colors of permanent marker to mark the beams which are at least 2 mm away from the outer surface of the bone. Be sure to keep track of the number of rows and columns (I documented mine with pictures each time). Secure the cut face of the bone with strong tape (e.g., Gorilla tape) such that the beams do not fall away when cut and make a final pass on the bandsaw to separate the beams from the bone. This process usually yields about 10-15 bone beam specimens of 2x2x40 mm (Figure A.3; right).

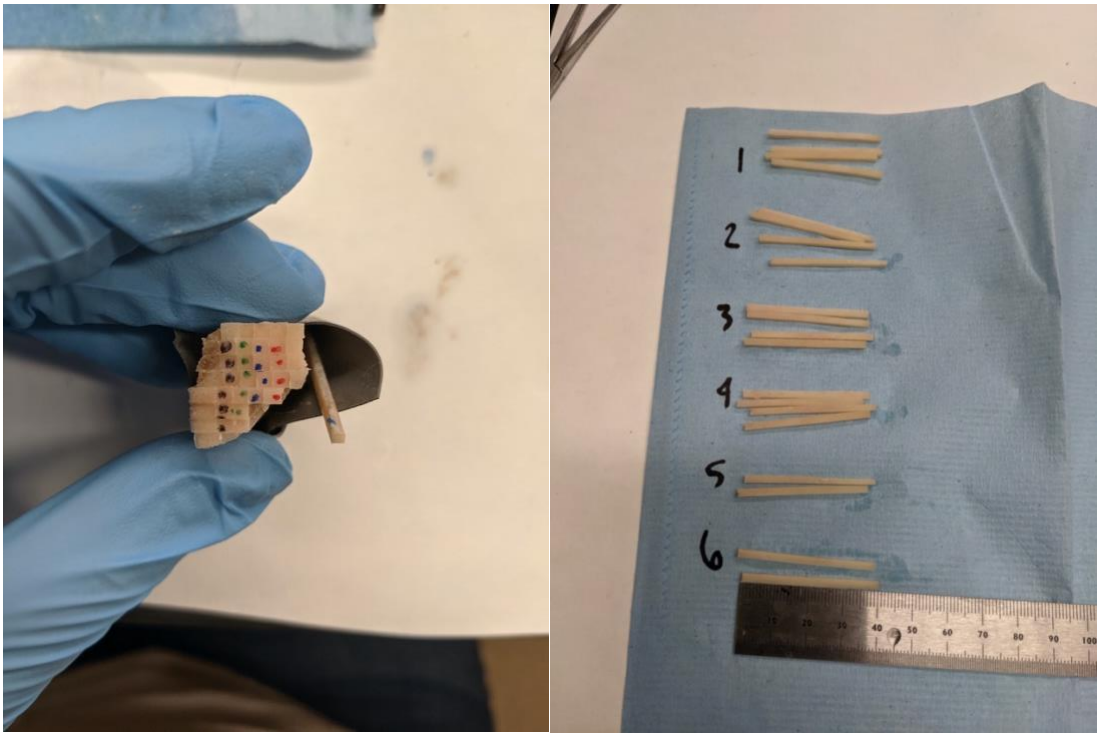

Figure A.3: Left: Individual bone beams, each column has been marked with a different color sharpie for tracking. **Right:** The same bone beams divided into rows. Each row contains beams whose ends have been marked with a different color.

After removing the tape, color the bare end of the bone beam with the corresponding color. Then apply silicone sealant (Advanced Silicone 2, GE Sealants & Adhesives) to the ends of the bone, leaving a bare 5 mm region in the center. The sealant acts as a barrier and prevents the bone from demineralizing in that region once placed in decalcification solution.

A2: Demineralization Protocol

Materials

- Formic acid stock solution
- Sodium citrate (greater than 99%)
- DI water
- Magnetic stirrer and stir bar
- Silicone sealant (Advanced Silicone 2, GE Sealants & Adhesives)

Procedure

The decalcification solution is a buffered [sodium citrate (100 g/L)] formic acid (22.5%) solution. I chose to use formic acid rather than EDTA because it acts more quickly to demineralize bone and is known to protect the collagen integrity [1]. To make the demineralization solution, obtain a formic acid stock solution of known concentration (I purchased formic acid 88% from Alfa Aesar by Thermo Fischer Scientific). If the stock solution is not 22.5%, dilute the stock solution with DI water using the equation $C_1V_1 = C_2V_2$ (where C = concentration and V = volume). Be sure to add the acid to water, in that order. Then calculate the amount of sodium citrate (100 g/L) required for the specific volume of formic acid solution (Sodium citrate, greater than 99%, R&D Systems). Using a magnetic stirrer and stir bar, mix the sodium citrate into the formic acid solution until the crystals have completely dissolved. Store the decalcification solution in an airtight container prior to use.

Before placing bone specimens in decalcification solution, cover ~17.5 mm of each end with silicone sealant (Advanced Silicone 2, GE Sealants & Adhesives) as a barrier to demineralization. This is important because the ends must be strong enough not to be crushed by

the grips during mechanical testing. Once the ends have been coated with silicone sealant and the sealant has dried (about 30 minutes), the bone specimen can be placed in Falcon conical tubes (15 mL) with decalcification solution and stored in the refrigerator during the decalcification process. Once bone specimens have been placed in decalcification media, the progress of demineralization should be assessed every 24 hours until the desired amount of demineralization is reached. For my purposes, the average demineralization time was between 72 and 96 hours. I used digital radiography to assess extent of demineralization (Figure A.4; Dental Aire DTX). Remember to peel off silicone sealant prior to mechanical testing, else the specimen will slip in the grips, or the sealant will transfer to the grips and make the grips sticky.

Note: Make sure to dispose of the demineralization solution in a waste bottle and mark with a hazardous waste label (follow lab protocol). Save for EHS to dispose of safely and properly. Contact Tanya Garcia-Nolen with questions.

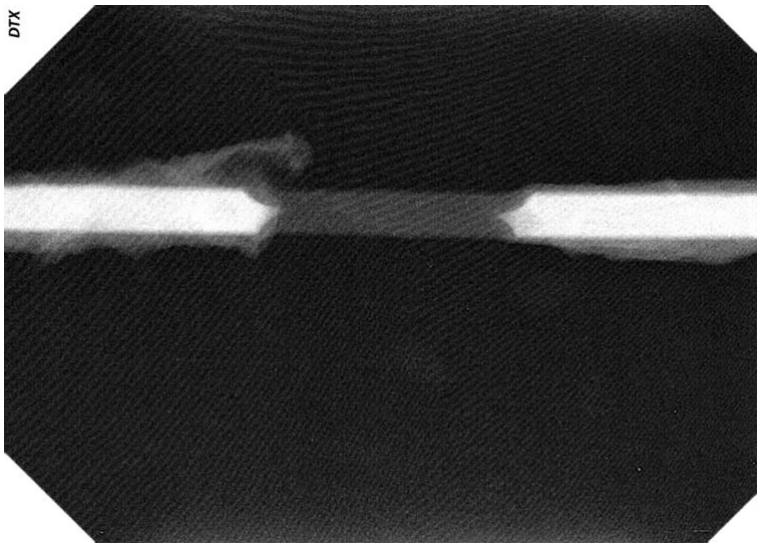

Figure A.4: Radiograph of one demineralized bone beam specimen, collected with the Dental Aire DTX radiography equipment. The center 5 mm of the beam is fully demineralized, indicated by the radiolucent quality. The mineralized ends (17.5 mm each) are protected by silicone sealant and appear radiopaque.

A3: Deuteration Protocol

Materials:

- Deuterium oxide, i.e., D_2O (99.9% isotopic purity, Sigma-Aldrich, St. Louis, MO, USA)
- Demineralized bone specimen
- Falcon tube

Procedure

Place the bone beam specimen in an empty Falcon tube. The next steps must be performed in the fume hood. Pipette 10 mL of deuterium oxide into the Falcon tube containing the bone beam. Quickly secure the respective caps onto the Falcon tube and the stock solution bottle. Place the Falcon tube in a test tube rack and store under refrigeration for 24 hours.

Note: Make sure to dispose of the deuterium oxide in a waste bottle and mark with a hazardous waste label (follow lab protocol). Save for EHS to dispose of safely and properly. Contact Tanya Garcia-Nolen with questions.

This protocol was adapted from methods reported in the literature for hydrogen-deuterium exchange used for the tracking of water in biological specimens [2]–[4].

A4: ADMET Mechanical Tester Assembly Protocol

Assembly of the mechanical tester (ADMET, Norwood, MA, USA) is relatively simple, as the device was manufactured to be transported easily. One may also refer to the document provided by ADMET titled "eXpert 4200 – UC Davis – SO 022001" which outlines an overview of the system and general setup procedures. This guide is printed and stored in the Pelican case, along with a hard copy of the MTESTQuattro user manual.

Begin by assembling the stand-alone frame for use independent from the microscope. The stand-alone frame assembly is detailed on page 5 of the document. Place the mechanical tester on top of the frame and secure with two small screws on the left side of the machine. Next secure all the electrical connectors and cables, which are labeled to indicate where they connect to the MTESTQuattro controller. The electrical connections include:

1. B4 (servo control),
2. Load (load cell),
3. Position (motor feedback),
4. Axial Strain (crosshead-to-crosshead position transducer), and
5. Auxiliary 1 (if using temperature controller for communication).

Each of these cables will connect the mechanical tester to the MTESTQuattro controller box (Figure A.5). There are also electrical connectors that connect the mechanical tester to the temperature controller (i.e., the black box; Figure A.6; left). These are lever-lock connectors that make the connection to the fluid bath heaters (Figure A.6; right). Additionally, the thermocouples connect the temperature controller to the heating elements on the mechanical tester. Note: be sure to maintain the proper polarity when connecting the thermocouples. The wire labeled "Controller" is fastened to the front of the mechanical tester (i.e., the side with the

position transducer) and the wire labeled “Limiter” is fastened to the back of the mechanical tester (i.e., the side with the drive motor). Refer to the CAD drawings and system diagram (Figure A.7) when necessary (hard copies are stored in the Pelican case).

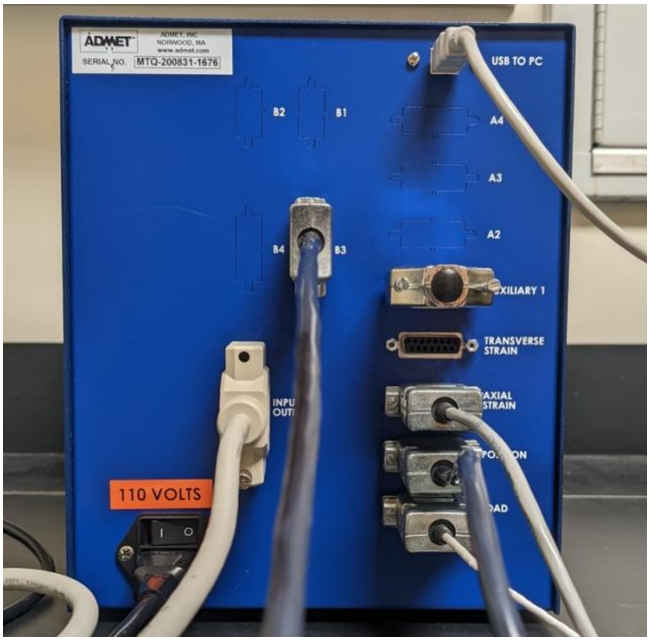

Figure A.5: Back-view of the MTESTQuattro controller box with all the electrical connections attached.

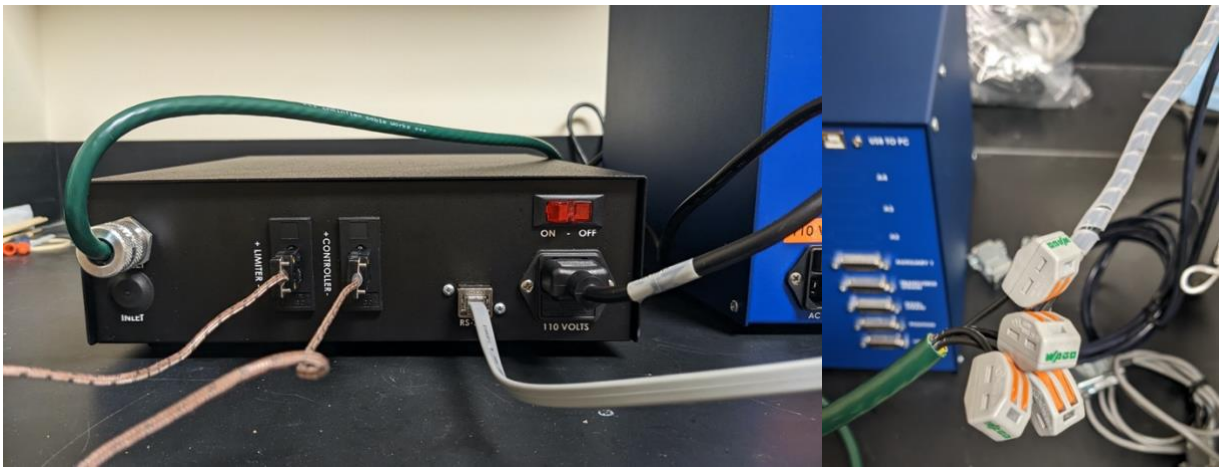

Figure A.6: Left: Back-view of the temperature controller box with all the electrical connections attached. **Right:** Lever-lock connectors.

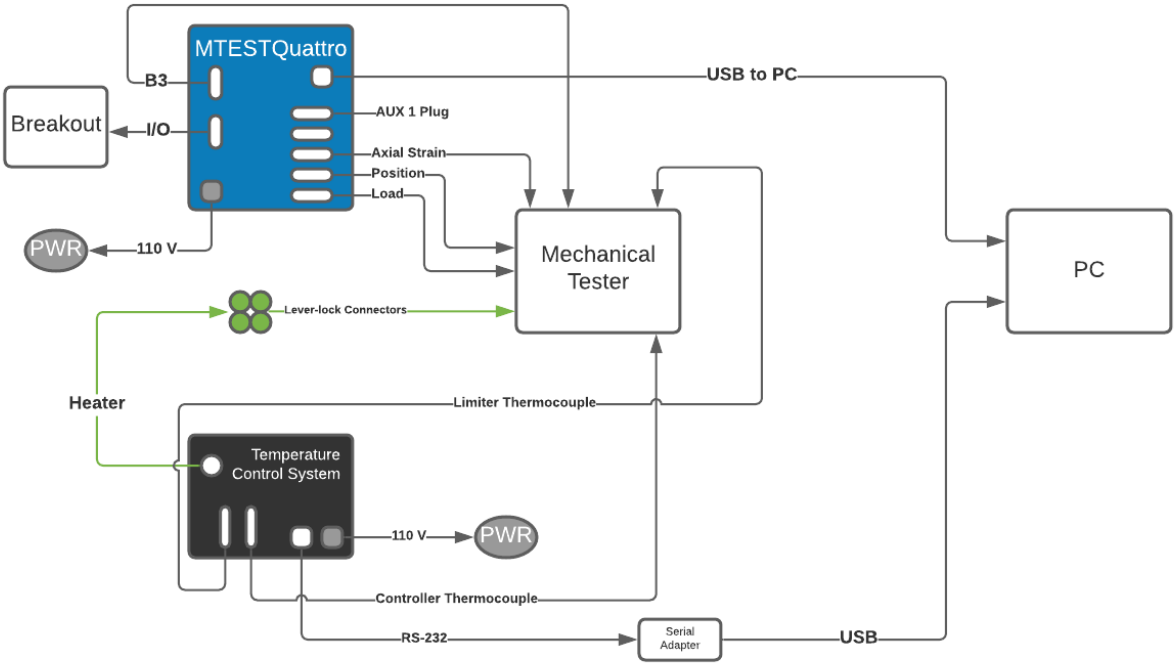

Figure A.7: Overall system diagram which includes all the necessary electrical connections for the AMDET mechanical tester, MTESTQuattro controller, temperature controller, and the PC.

The following pages (pp. 125-127) are the CAD drawings of the micromechanical tester. These drawings were reprinted with permission from ADMET (www.admet.com, Norwood, MA, USA).

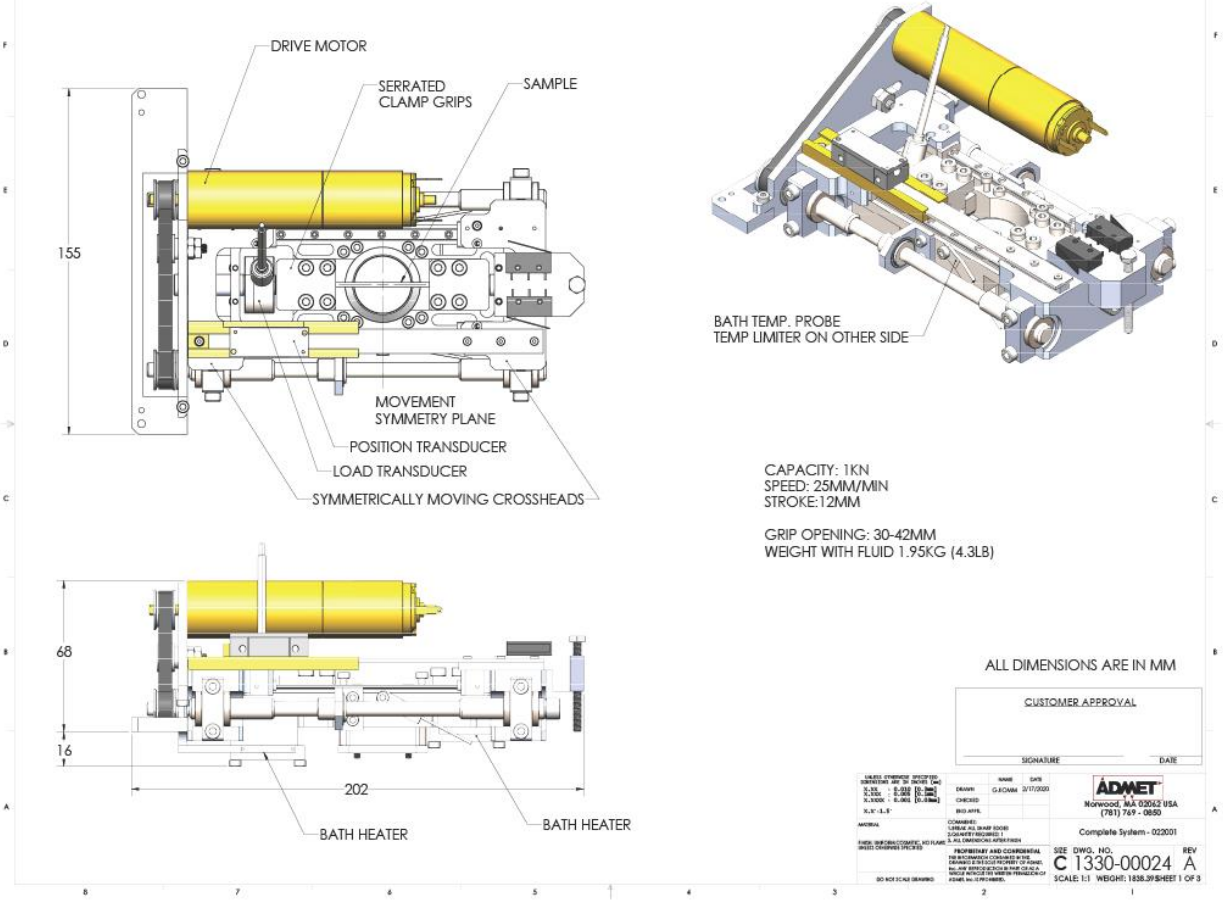
DRIVE MOTOR
SERRATED CLAMP GRIPS
SAMPLE
155
MOVEMENT SYMMETRY PLANE
POSITION TRANSDUCER
LOAD TRANSDUCER
SYMMETRICALLY MOVING CROSSHEADS
BATH TEMP. PROBE
TEMP LIMITER ON OTHER SIDE
CAPACITY: 1KN
SPEED: 25MM/MIN
STROKE:12MM
GRIP OPENING: 30-42MM
WEIGHT WITH FLUID 1.95KG (4.3LB)
68
16
202
BATH HEATER
BATH HEATER
ALL DIMENSIONS ARE IN MM
CUSTOMER APPROVAL
SIGNATURE
DATE
ADMET
Norwood, MA 02062 USA
(781) 769 - 0850
Complete System - 022001
SIZE DWG. NO. REV
C 1330-00024 A
SCALE: 1:1 WEIGHT: 1838.39 SHEET 1 OF 3

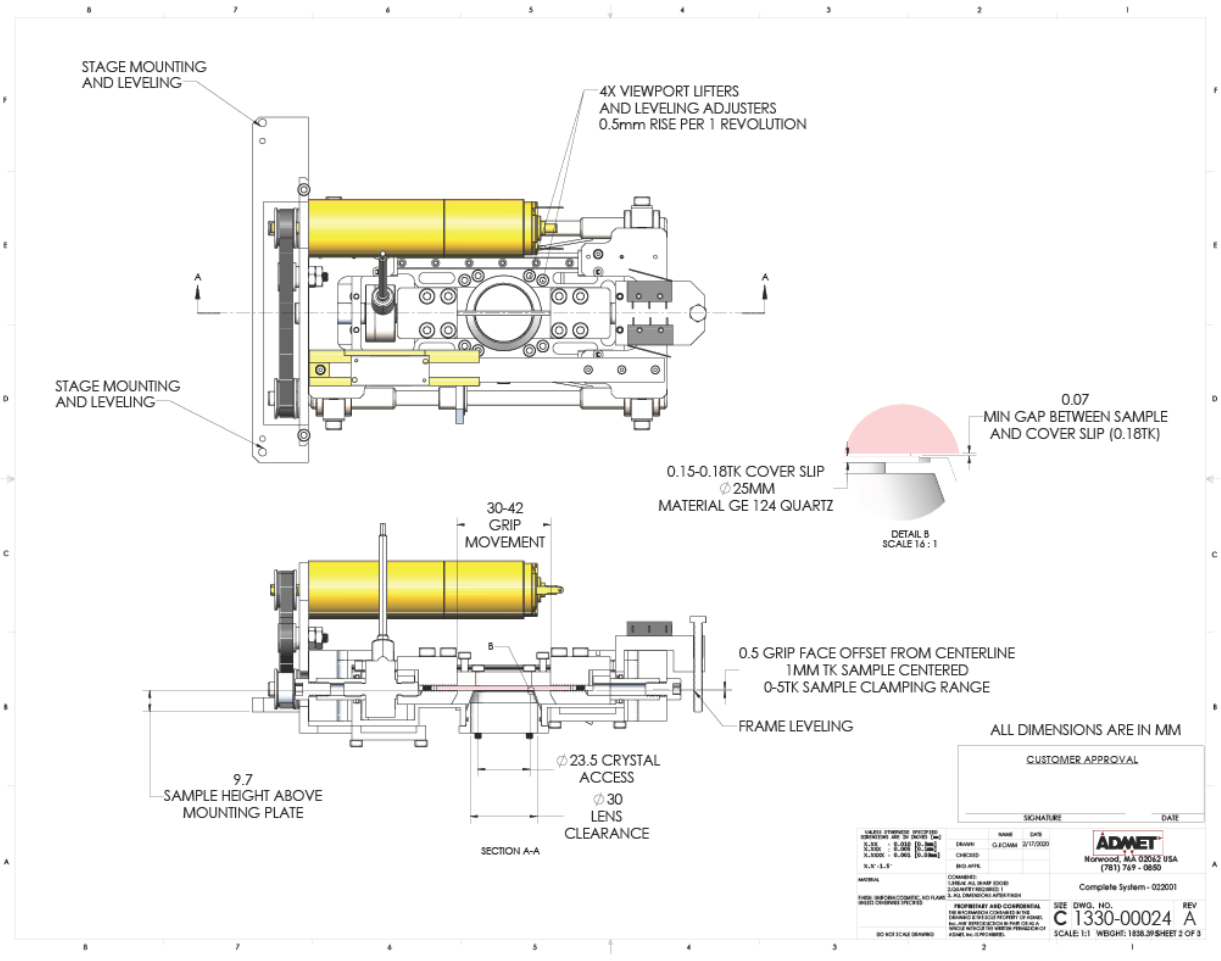
STAGE MOUNTING
AND LEVELING
4X VIEWPORT LIFTERS
AND LEVELING ADJUSTERS
0.5mm RISE PER 1 REVOLUTION
STAGE MOUNTING
AND LEVELING
0.07
MIN GAP BETWEEN SAMPLE
AND COVER SLIP (0.18TK)
0.15-0.18TK COVER SLIP
∅25MM
MATERIAL GE 124 QUARTZ
DETAIL B
SCALE 16 : 1
30-42
GRIP
MOVEMENT
0.5 GRIP FACE OFFSET FROM CENTERLINE
1MM TK SAMPLE CENTERED
0-5TK SAMPLE CLAMPING RANGE
FRAME LEVELING
ALL DIMENSIONS ARE IN MM
CUSTOMER APPROVAL
SIGNATURE
DATE
∅23.5 CRYSTAL
ACCESS
∅30
LENS
CLEARANCE
9.7
SAMPLE HEIGHT ABOVE
MOUNTING PLATE
SECTION A-A
ADMET
Norwood, MA 02062 USA
(781) 769 - 0850
Complete System - 022001
SIZE DWG. NO.
C 1330-00024
REV
A
SCALE: 1:1 WEIGHT: 1838.39 SHEET 2 OF 3

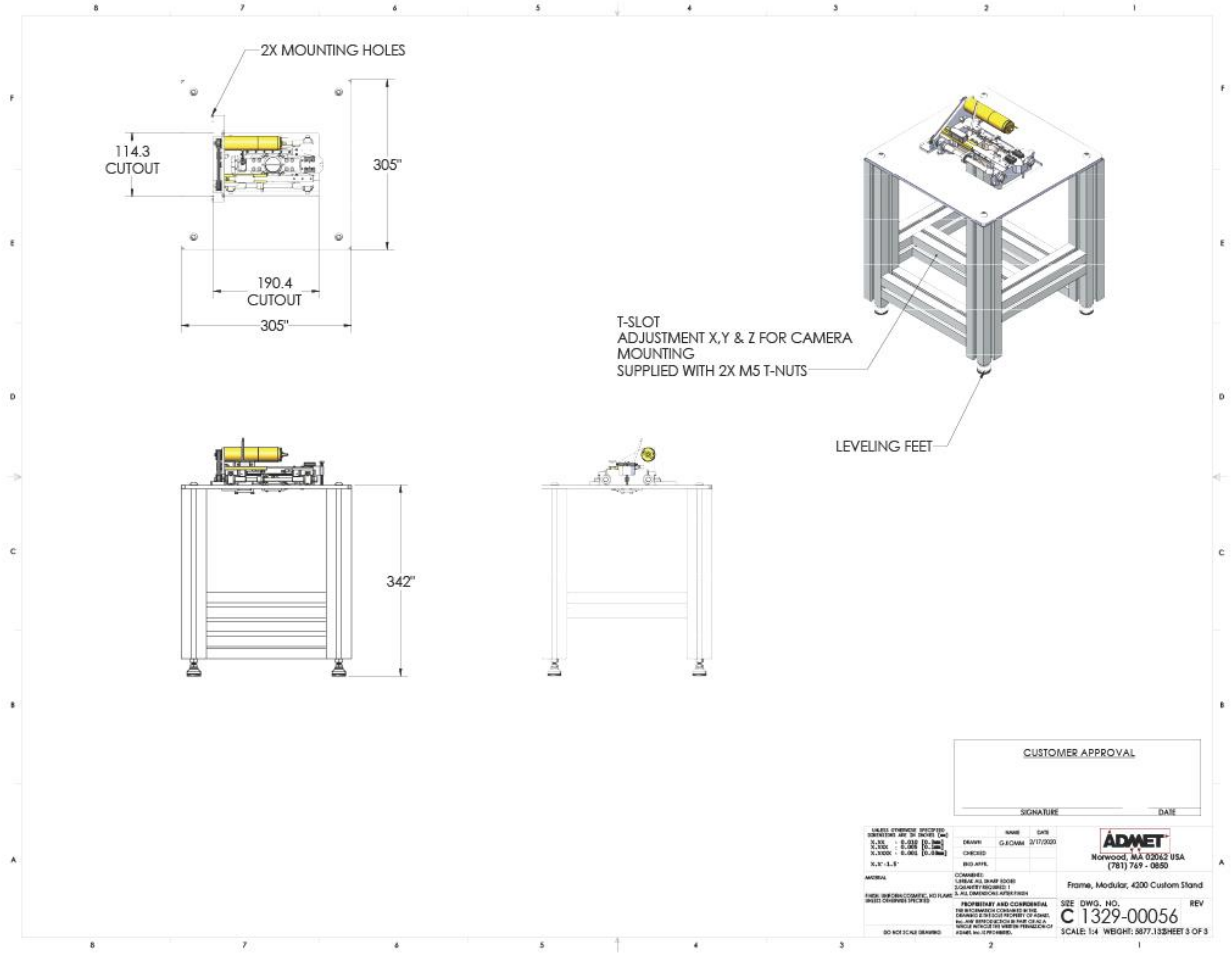
2X MOUNTING HOLES
114.3
CUTOUT
305"
190.4
CUTOUT
305"
T-SLOT
ADJUSTMENT X,Y & Z FOR CAMERA
MOUNTING
SUPPLIED WITH 2X M5 T-NUTS
LEVELING FEET
342"
CUSTOMER APPROVAL
SIGNATURE
DATE
ADMET
Norwood, MA 02062 USA
(781) 769 - 0850
Frame, Modular, 4200 Custom Stand
SIZE DWG. NO. REV
C 1329-00056
SCALE: 1:4 WEIGHT: 5877.13SHEET 3 OF 3

A5: Raman Microscope Standard Operating Procedure

The following information is adapted from the document titled “Death Star Protocol SOP.docx” which can be found on the Carney Lab Shared folder in Box.

Death Star - Raman Microscope Manual of Operation

The RAMAN microscope was designed and constructed on site by Lever Photonics. Please contact maria@leverphotonics.com or (720) 696-0195 for assistance.

WARNING: this microscope has a type IV 785nm laser. Use caution when operating and never look through the eyepiece when the laser is on!

Description

The Death Star is a custom Raman confocal microscope capable of imaging and trapping. It is also equipped with brightfield and widefield fluorescence microscopy. This is a very quick guide on how to operate the microscope without a dedicated GUI and only using third party vendor software.

Specs

Laser: 785 nm, 80 mW (after patch fiber) – IPS Technologies

Scope body: Olympus IX73

Objectives: Olympus 20x, NA = 0.75 and Olympus 60x, NA = 1.2 W

Camera: Andor Newton CCD

Raman Spectroscopy Starting Routine - Both Imaging and Trapping modes

1. Turn on mirrors power supply (orange button). Make sure the voltage values are close to **24 V** and current values are **0.3 A**. (**IMPORTANT**: If the values are off, there might be a short circuit. Turn off the power supply right away.) Note: only need to do this step if you are scanning a sample.
2. Turn on spectrometer. Note: this usually stays on, most likely won't need to turn on each time.
3. Turn on the laser. Pull the red knob toward you until it clicks. To turn the laser on, push the red button on the top left. A light will come on above it indicating that the laser is on. Give the laser a few minutes to warm up before use, the power will fluctuate during this time and measurements will not be accurate. Note: The CCD camera itself doesn't have a power switch.

Go to folder C:\Users\Carney Lab\Desktop\Death Star\Control Software and start the following software:

4. Andor SOLIS - See below for more information.
5. DAQExpress - Start ZeroGalvoMirrors and run the task either by clicking the green arrow or using the keystroke CTRL+R. This will zero the mirrors, so they are centered. Note: only open this if scanning.
6. MPH16 Control – The default should say COM5, click okay and then use the drop-down menu to set the pinhole at 1mm. Do not change the alignment unless specified by Randy or Maria.

7. ThorCam - Click on the small camera icon and open the CS2100M-USB sn: 07988 camera. Click the play icon on the top left corner to get a live feed. In the settings, the exposure time will need to be adjusted based on what the sample is.

Adjusting the spectrometer and CCD Camera settings using Solis.

When starting Solis with the spectrometer on, the software should automatically recognize the spectrometer and the CCD camera. If recognized properly Solis will 1) indicate the number of the camera on the very top left of the window (Figure A.8 Shows "Andor SOLIS Spectroscopy CCD-22728") and 2) the different boxes of the spectrometer's graphic user interface (GUI) should show below the data plot.

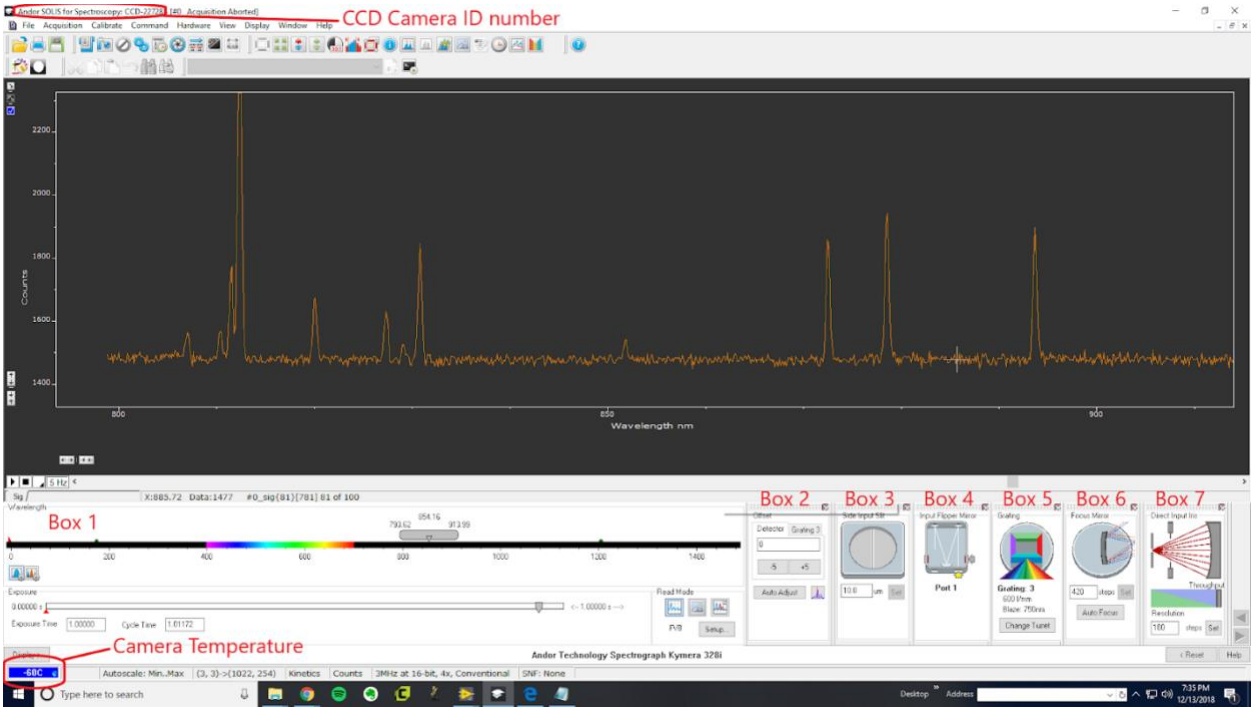

Figure A.8: Solis graphic user interface (GUI). The spectrum shown is that of the room light in the 800-950 nm range.

Temperature Setting

On the bottom left corner of the screen there is a blue or red display that indicates the temperature of the CCD camera (see Figure A.8). Click on it, turn it on and set the temperature

to -60°C for routine measurements. (This should happen automatically but watch to make sure it gets to -60°C before collecting measurements.) When the display turns blue it is indicating that the temperature is stable. If red, the CCD temperature is not stable, and any data acquired would not be reliable.

Grating Setting

Select the grating by clicking on of the color bars in Box 5 (Figure A.8). A good starting grating is the 600 lines/mm which would enables focus in the fingerprint region. There are three other gratings available: 150 lines/mm, 300 lines/mm, and 1200 lines/mm. As the number of lines per mm increases, so does the spectral resolution, but the spectral range (i.e., the number of observable wavelengths) decreases.

Spectral Range Setting

In Box 1, set the desired spectral range. This can be done by left clicking and setting the center, the minimum, or the maximum wavelengths to de desired values. Make sure that the spectral range does not include the laser wavelength to avoid damage to the CCD camera (i.e., make sure the minimum is above 785 nm). The spectral range can also be set by sliding the gray bar in Box 1.

Acquisition Mode and Exposure Settings

Single Spectrum

To acquire a single spectrum, go to Acquisition > Acquisition Setup. The acquisition setup window will open. On the Camera Setup tab (See Figure A.9) set:

- Acquisition Mode = Single

- Triggering = Internal
- Readout Mode = Multitrack

Go to Timings and set Exposure Time to the desired value.

For most of the experiments that the Death Star can perform there is no need (nor is it recommended) to modify any of the values on the **Vertical Pixel Shift**. The default values are Shift Speed (μsec) =12.9 and Vertical Clock Voltage Amplitude=Normal.

The next box below is the **Horizontal Pixel Shift** settings. Faster Readout Rates will allow faster measurements but the noise on the data will increase. For focusing and adjusting purposes it is recommended to use the fastest read out rate (3 MHz) but for data acquisition a slower rate is advised. On the other hand, the lowest Pre-Amplifier Gain will provide the highest sensitivity of the camera, but it will prevent the system from using the full dynamic range of the CCD camera. That means the camera will saturate easier, hence it is a good setting for weak signals but not for strong signals. The highest Pre-Amplifier Gain is recommended for very strong measurements or binned measurements, such as a single spectrum measurement.

When the Multitrack mode is selected the MT Setup button will activate (highlighted in blue on Figure A.9), when clicked, a second window called Setup Multi-track will appear. We will go over how to setup the tracks in the next section “Image or Full CCD chip.” Note: It is strongly recommended that none of the values in that window are modified unless the system has been recently re-aligned and they need to be changed. If changed, please do keep note of the current values as the software won’t keep records.

Click OK in both windows (there should be two windows opened if you clicked on the MT Setup button, only one window if you did not). The next step is to click on one of the acquisition buttons described below in the Toolbars summary.

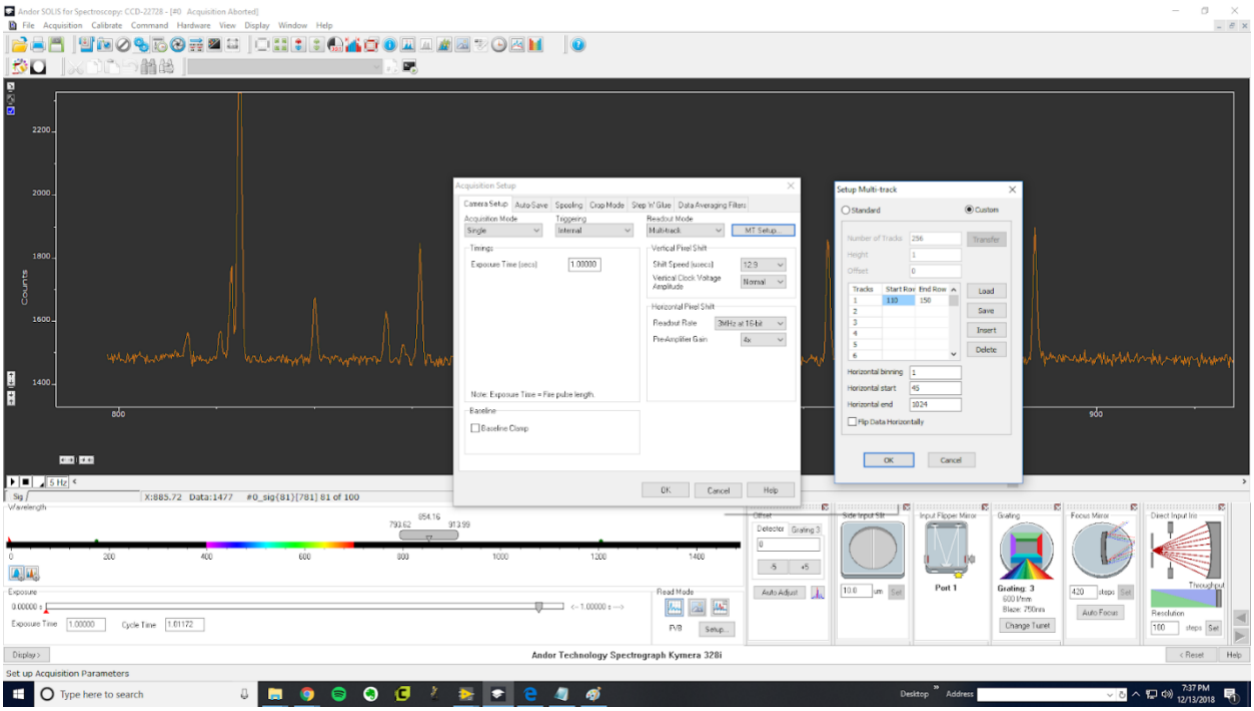

Figure A.9: Single spectrum setup GUI.

Toolbars Summary

There are three toolbars displayed by default: File Management, Acquisition and Display toolbars (Figure A.10). If they are not displayed, they can always be made visible by going to View on the Menu bar and selecting the toolbars.

The **Acquisition Toolbar** has (1) a video camera icon and (2) a normal camera icon. The first icon is for continuous or live acquisition. It will forever loop through acquisitions using whatever settings were specified. This function is useful for focusing purposes. The next icon, the regular camera, is used to acquire data. When clicked, the software will acquire the data with

the selected settings but unless specified it will not automatically save the collected data. Make sure to save your data before collecting more data or going into continuous mode, as your data could be overwritten. The third icon (forbidden sign) will only activate during an active acquisition and is used for stopping the current acquisition or the continuous mode. For brevity, the remainder of the icons will not be discussed.

The **Display Toolbar** has icons for quickly toggle between different pre-set data display modes. The best way to get to know each button is to use trial and error.

Figure A.10: Toolbars in SOLIS.

Adjusting laser power

The laser power can easily be adjusted from the side of the enclosure closest to the door. When viewing the optical setup, there will be a circular piece with numbers around the outside that rotates; this is the waveplate and the mechanism to adjust the laser power. Turn on the power meter (voltmeter) and place the sensor directly in front of the mirrors. Twist the waveplate to either increase or decrease the power as needed.

Optimizing Spectral Resolution

If the signal is noisy but it seems peaks are present, there are ways to adjust the system to increase the spectral resolution. The first method is to increase the exposure time. Normal samples are viewed at an exposure time of 1 second, however if the signal is noisy then peaks may be lost. The exposure time can be increased as much as necessary to gather the spectra while dimming the noise signal.

Another method is to adjust the laser location by slowly focusing it up and down on the sample. For some samples a better signal might be seen when the laser is not completely focused. Make minor adjustments while watching the spectra on the live mode to see if any of the peaks become more clear or stronger.

A6: MTESTQuattro Test Procedures

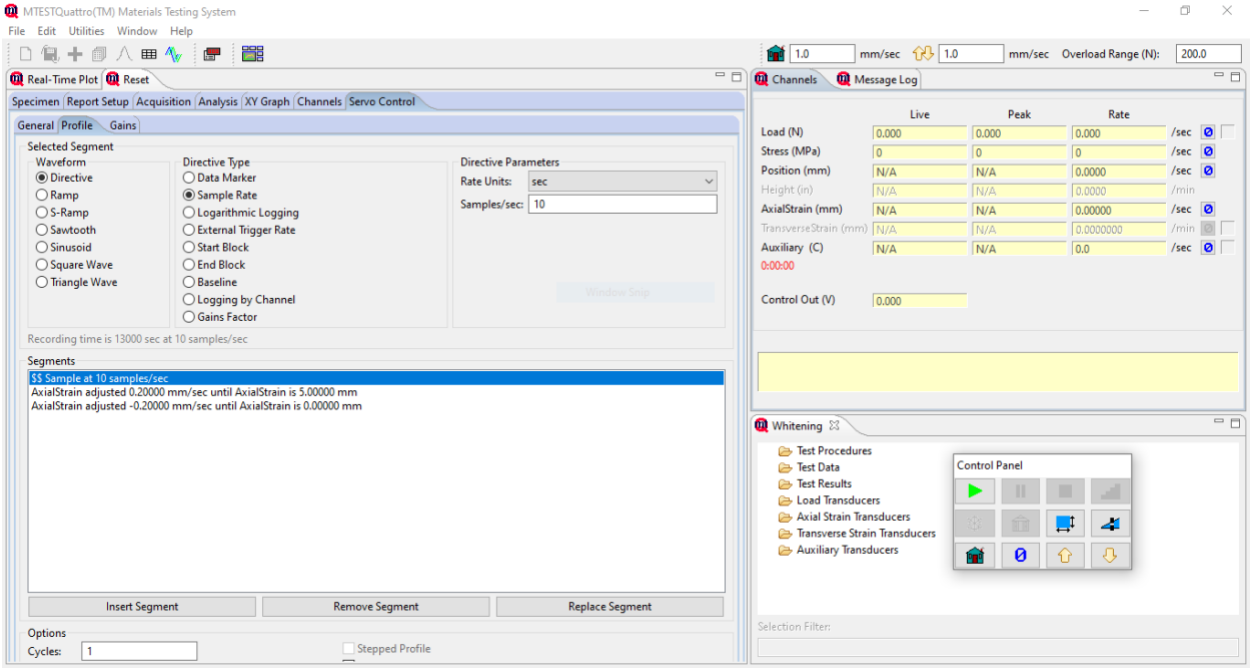

Figure A.11: Screenshot of the "Reset" protocol in MTESTQuattro, used to reset the machine before a mechanical test and maintain consistency.

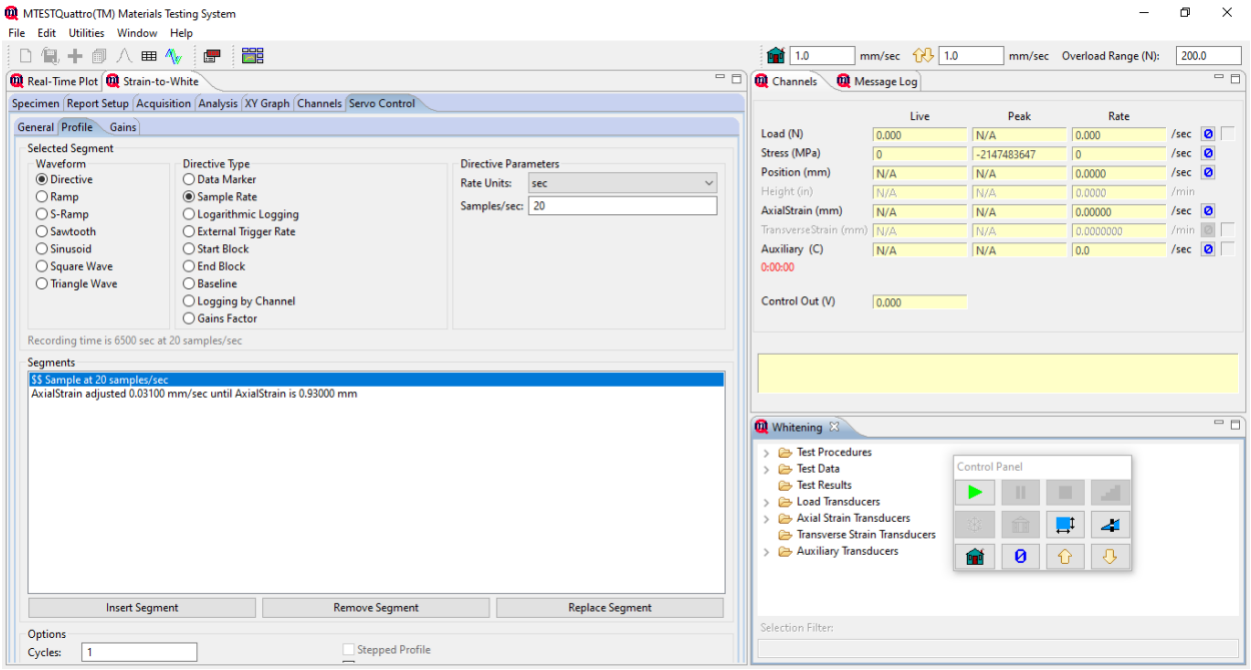

Figure A.12: Screenshot of the "Strain-to-White" protocol in MTESTQuattro, used to conduct the Mechanical Test procedure.

A7: Stress-Whitening Data Collection and Analysis Procedures

Collection

Stress-whitening was quantified using a custom macro in ImageJ/Fiji (NIH, Bethesda, MD, USA). The stress-whitening quantification followed this protocol:

1. Open .mp4 video files using the FFMPEG plugin (File > Import > Movie (FFMPEG)).
2. Run the macro to create a rectangular ROI (area = 2992 pixels) and place over the region of the bone specimen where whitening occurs (the demineralized center).
    a. Plugins > Macros > Run > "FINAL_DrawBoneROI.ijm"
3. Take a screenshot of the ROI position for reference.
4. Run macro to take an initial measurement (t = 0 sec) and then take a measurement every second for 30 seconds (chosen because the mechanical test procedure runs for 30 seconds).
    a. Plugins > Macros > Run > "FINAL_TakeInitialMeasurementThenMeasureEverySecfor30Sec.ijm"
5. Save the measurements and export into an Excel file for analysis.
6. Repeat steps 1-5, but instead creating a rectangular ROI (area = 15614 pixels) over the black rectangle on the calibration card.
    a. Plugins > Macros > Run > "FINAL_DrawReferenceROI.ijm"

Analysis

Stress-whitening was quantified using a custom macro in ImageJ/Fiji (NIH, Bethesda, MD, USA). Specifically, stress-whitening was quantified by comparing the average pixel intensity of the rectangular region of interest (ROI; Figure A.13; right) to the initial (pre-strained) pixel intensity of the ROI (Figure A.13; left). The pixel intensity was corrected for

using the black rectangle on the grayscale calibration card that was included in the frame for all videos (Figure A.13). Stress-whitening (W) was calculated using the following equation [3]:

$$W = \frac{\frac{\sum_x \sum_y I_{max}(x,y)}{n_{pixel}} - \frac{\sum_x \sum_y I_{init}(x,y)}{n_{pixel}}}{\frac{\sum_x \sum_y I_{init}(x,y)}{n_{pixel}} - I_{correction}}$$

Where I_{max} is the intensity of the ROI; I_{init} is the intensity of the ROI prior to loading; $I_{correction}$ is the average intensity of the black rectangle on the grayscale calibration card included in the frame; and n_{pixel} is the area of the ROI.

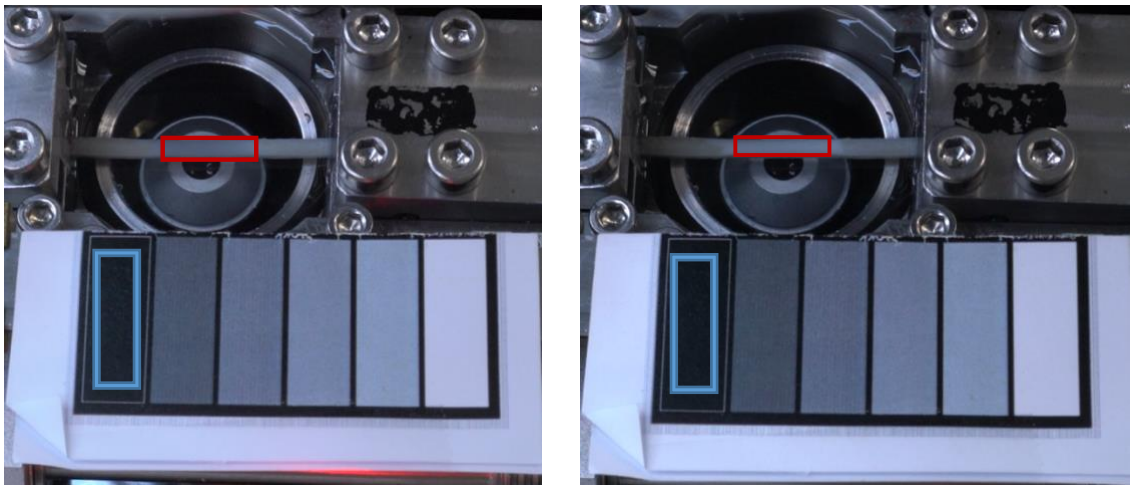

Figure A.13: Comparison of a demineralized bone specimen in the unloaded state (left) and the loaded state (right). The red rectangle shows the ROI that was used to calculate the pixel intensity of the bone beam. The blue rectangle shows the ROI that was used to calculate the pixel intensity of the black rectangle on the grayscale calibration card.

Whitening time points were determined using the external trigger that was placed in the field of view of the camera during the experiments. This method was used to identify the whitening during the ramp to the final nominal strain of 0.03.

Macro Codes

The macro codes can be accessed on GitHub (github.com/legloekler/Bone-Whitening). There are three files used for stress-whitening quantification, including:

1. “FINAL_DrawBoneROI.ijm”
2. “FINAL_DrawReferenceROI.ijm”
3. “FINAL_TakeInitialMeasurementThenMeasureEverySecfor30Sec.ijm”

A8: Final Experimental Protocol

Materials Checklist

- 8 demineralized bone beam specimens
- 1 L saline (7 g NaCl/1 L DI H_2O)
- ADMET mechanical testing equipment (everything in the Pelican case)
- Raman equipment
    - 20x objective (NA = 0.4)
- Video equipment
    - Camera
    - Tripod
    - SD card reader
    - Ring light
- Vacuum trap
- Forceps
- Falcon tubes
- Calipers or metric ruler
- Plastic transfer pipettes

Raman Data Collection Settings

- Grating: #2
- Throughput: 100%
- Wavelength: 826.61 - 1080.06 nm
- Power: 67 mW
- MPH16 Control: 1mm

- ThrorCam: “Display Settings” > Check “Continuous Autoscale” and “Use ROI”

Important Notes

- **Remember to take photos of each step for records.**
- **Both the “Sitting in Solution Test” and the “Mechanical Test” should be conducted on the same day for each specimen, always beginning with the “Sitting in Solution Test.”**

24 hours prior to testing:

Specimen Preparation (10 minutes)

1. Move the desired number of bone beam specimens from the freezer to the refrigerator (in the Carney Lab) to defrost for 24 hours prior to testing. Specimens should be stored in Falcon tubes containing at least 10 mL of saline solution while they defrost.
2. Ensure there is enough saline solution for testing the next day (including enough saline to fill the fluid bath during testing). This will depend on the number of specimens being tested, approximately 10 mL per specimen (upper estimate).

Equipment Setup (30 minutes)

1. Ensure that the required equipment is taken to the Carney Lab in preparation for testing (see "Materials Checklist" above).
2. The Raman microscope platform must be adjusted to accommodate the mechanical tester.
    a. Remove the condenser and unscrew the four points of contact between the platform and the base.
    b. Remove the spacers from under the platform (previously secured by the screws) and store them in a safe place.
    c. Remove the objective wheel, move the objective platform as far down in the Z-direction as possible, and secure the 20x, NA= 0.4 objective.
    d. Replace the microscope platform and secure with shorter screws.
    e. Place the mechanical tester on the platform and adjust the platform position such that the objective is located within the optical viewport of the mechanical tester (Figure A.14).
3. The mechanical testing equipment can now be assembled.

a. Place the Pelican case on the ground to the left of the Raman microscope and place the MTESTQuattro controller (blue) and, if using, the temperature controller (black) on top of the Pelican case.

b. Attach all electrical connections, including those that run from the mechanical tester to the MTESTQuattro controller.

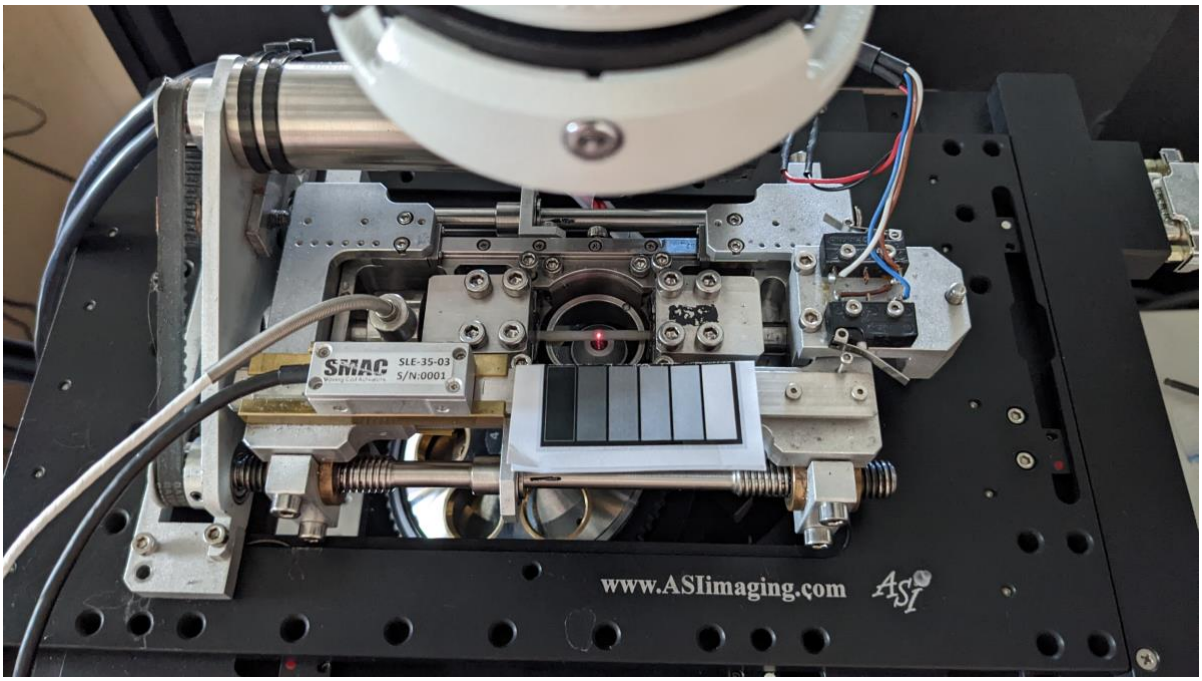

Figure A.14: Overview of the AMDET mechanical tester resting on the Raman microscope platform.

Day of testing:

Equipment Setup (1.25 hours)

1. Raman spectrometer
    a. Follow the instructions on the Carney Lab computer using the document titled "Death Star Protocol SOP" (included in Appendix A5).
    b. Ensure that the **20x objective, NA = 0.4** (green) is on the microscope.
    c. Set the laser power to **67 mW** for bone samples.
    d. In the Andor SOLIS software, select **Grating #2** (red) and change spectral range to **826.61 - 1080.06 nm** to capture the wavenumbers of interest. Set throughput to 100. Set exposure time = 10 (seconds); accumulations = 1; kinetic series length = 30. Make sure "Cosmic Ray Removal" is selected. (See Figure A.15 for screenshot of the correct settings.)
    e. Allow laser to cool to -60°C and ensure the temperature box is blue (Figure A.16) before collecting any data.

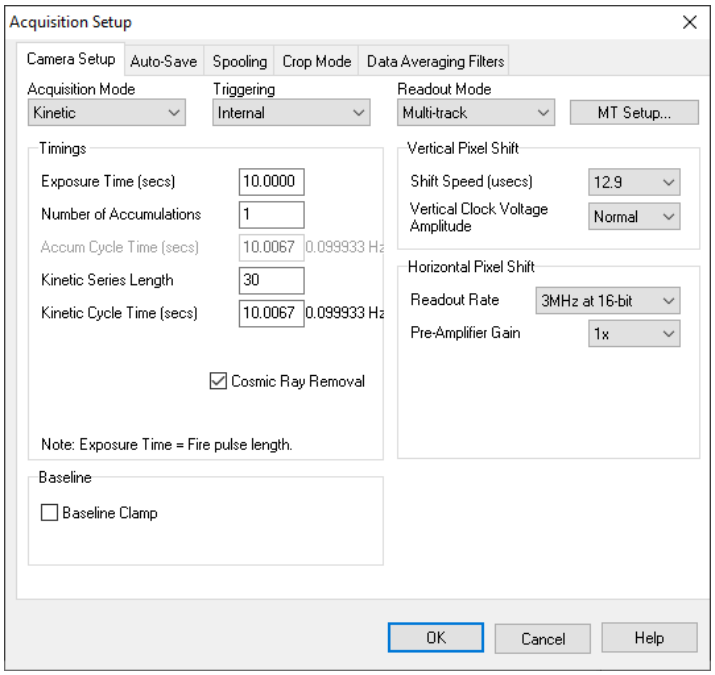

Figure A.15: Screenshot of the Acquisitions Setup window with the correct settings.

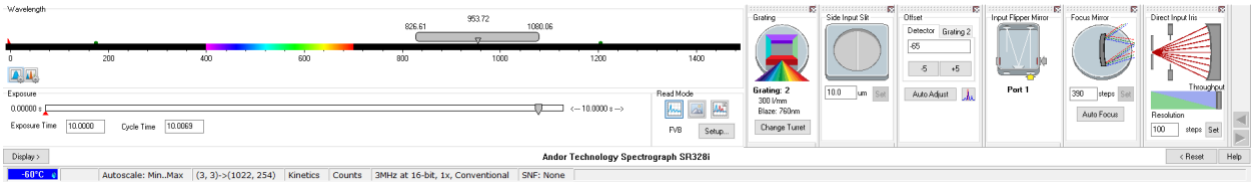

Figure A.16: Screenshot of the Andor SOLIS toolbar with the correct acquisition settings.

2. Specimen
    a. Follow the “Reset” protocol to adjust the grip separation to “home” (i.e., grip separation = 31 mm) using the MTESTQuattro software and confirm the grip separation is 31 mm using the metric ruler. Use this value as the value for grip separation in the “Report Setup” tab.
    b. Secure the specimen in vice grips.
    c. Use plastic transfer pipet to fill fluid bath with saline. Ensure the saline fully covers the specimen and monitor this level throughout the experiment.
3. Mechanical testing equipment

a. Start laptop computer and plug in both the USB cables from the MTESTQuattro and temperature controllers. Power up the MTESTQuattro controller and the temperature controller. Open the “Device Interface” and “MTESTQuattro” software (in that order) using the shortcuts on the desktop.
b. Ensure that the temperature setpoint it set at **38°C** and run the “Static Test” protocol. This protocol holds position and allows the temperature to equilibrate for 90 minutes while collecting temperature and mechanical data. This is **extremely important** because even minor variations in temperature will cause interference with the load data. Note: the temperature controller setpoint has already been set to the correct temperature. There is no need to reset each time, as it remembers the setpoint temperature.
    i. Aside: the temperature controller was having issues heating to the setpoint, so I allow it to heat up to whatever temperature it can achieve. Having the temperature controller on allows for the collection of temperature values, which cannot be collected with the controller powered down.
c. Once the “Static Test” protocol has completed and you saved the data, open the test procedure titled “**Strain-to-Whiten”** in MTESTQuattro software (i.e., the ramp-to-hold protocol).
d. Set up specific report parameters for the specimen in MTESTQuattro software under the “Report Setup” tab or by clicking on the shortcut in the Control Panel. Make sure to include (at the very least) the date, operator, and specimen identifiers.

4. Data collection
    a. Open Box (ucdavis.app.box.com) and prepare to save the mechanical test and the Raman data in their respective locations.
    b. Confirm that you have set up the correct test parameters in both the MTESTQuattro and Andor SOLIS software.

Experimental Procedure 1 – "Sitting in Solution Test" (1.25 hours)

Raman data naming convention:

YYYYMMDD_Row#_Color_LaserPower_Objective_Grating_Throughput_AcquisitionLength_KineticSeriesLength_Time=Xm.sif

e.g.,

20220127_Row2_Green_67mW_20x_0.4NA_Grating2_Throughput100_10sec_KS30_t=0m.sif

Note: During this experiment, periodically check fluid bath to ensure there is enough solution to submerge the bone specimen. Refill the fluid bath if the solution evaporates significantly during the experiment and take note of these occurrences.

This protocol will be completed once for each specimen.

1. Turn off all lights in the room, then turn on the laser and allow it to cool to -60°C.
    a. Focus the laser so it is within the material and take the temperature of the fluid bath using the hand-held temperature probe.
    b. Collect initial Raman data (1 kinetic series with length of 30, ten second acquisitions).
    c. Turn off laser and Andor SOLIS software, then turn all the lights on.
2. Wait for 20 minutes. Then, turn off all the lights in the room, turn on the laser and allow it to cool to -60°C, and restart Andor SOLIS (check settings).
    a. Focus the laser so it is within the material and take the temperature of the fluid bath using the hand-held temperature probe.
    b. Collect t=20 min Raman data (1 kinetic series with length of 30, ten second acquisitions).

    c. Turn off laser and Andor SOLIS software, then turn all the lights on.

3. Wait for 20 minutes. Then, turn off all the lights in the room, turn on the laser and allow it to cool to -60°C, and restart Andor SOLIS (check settings).
    a. Focus the laser so it is within the material and take the temperature of the fluid bath using the hand-held temperature probe.
    b. Collect t=40 min Raman data (1 kinetic series with length of 30, ten second acquisitions).
    c. Turn off laser and Andor SOLIS software, then turn all the lights on.
4. Wait for 20 minutes. Then, turn off all the lights in the room, turn on the laser and allow it to cool to -60°C, and restart Andor SOLIS (check settings).
    a. Focus the laser so it is within the material and take the temperature of the fluid bath using the hand-held temperature probe.
    b. Collect t=60 min Raman data (1 kinetic series with length of 30, ten second acquisitions).
    c. Turn off laser and Andor SOLIS software, then turn all the lights on.

The “Mechanical Test” procedure (i.e., Experimental Procedure 2) should be completed immediately following the “Sitting in Solution Test” procedure (i.e., Experimental Procedure 1). Each individual mechanical test should be completed immediately following the previous test. Put simply, all the tests should be completed on the same day with no breaks in between.

Experimental Procedure 2 – "Mechanical Test" (1 hour)

Raman data naming convention:

YYYYMMDD_Row#_Color_LaserPower_Objective_Grating_Throughput_AcquisitionLength_KineticSeriesLength_Unloaded/Loaded_Test#_Focus#.sif

e.g.,

20220127_Row2_Green_67mW_20x_0.4NA_Grating2_Throughput100_10sec_KS30_Unloaded_Test1_Focus1.sif

Note: During this experiment, periodically check fluid bath for leaking or evaporation. This protocol will be completed three times for each specimen (i.e., three total mechanical tests per specimen).

1. Set up the camera on the tripod to record a video of the experiment. Configure the external trigger and the grayscale reference card so they are in the field of view of the camera. Set up the ring light so that is in position to evenly illuminate the field of view. See Figure A.17 for overview of the setup.
2. Open Box (ucdavis.app.box.com) and prepare to save the mechanical test and the Raman data in their respective locations.
3. Confirm that you have set up the correct test parameters in both the MTESTQuattro and Andor SOLIS software.
4. Turn off all the lights in the room, then turn on the laser and allow it to cool to -60 deg C. Focus the laser so it is within the material.
5. Collect initial Raman data (i.e., "Unloaded_TestX_Focus1" – 1 kinetic series with length of 30, ten second acquisitions).

6. Move the objective out of the material, then refocus the laser within the material.
7. Collect Raman data (i.e., “Unloaded_TestX_Focus2” – 1 kinetic series with length of 30, ten second acquisitions).
8. Turn off laser and turn all the lights on.
9. Ensure the external trigger (indicating the beginning of the test) is in the video field of view. This is imperative, as the goal is to have synchronized data collection.
10. Turn on the ring light so that it is evenly illuminating the field of view.
11. Begin video recording and zero all parameters on MTESTQuattro software. Run the mechanical test program.
12. When the external trigger has indicated that the test is complete, end the video recording and turn off all the lights.
13. Turn on the laser and allow it to cool to -60 deg C. Refocus the laser to ensure that it is within the material.
14. Collect Raman data (i.e., “Loaded_TestX” — 1 kinetic series with length of 30, ten second acquisitions). and ‘save as’ to appropriate folder.
15. Export the mechanical test data and save to the appropriate folder in Box (make sure to save both the .csv and .mtw files).
16. Use the “Batch Conversion” option on the Andor SOLIS software (File > Batch Conversion) to convert the .sif files to .asc files so they can be analyzed in the Noodle program. Save both the .sif and .asc files to the appropriate folder in Box.
17. Download video and save to the appropriate folder in Box. Confirm the video has been saved to Box and delete the video from the SD card to preserve space.

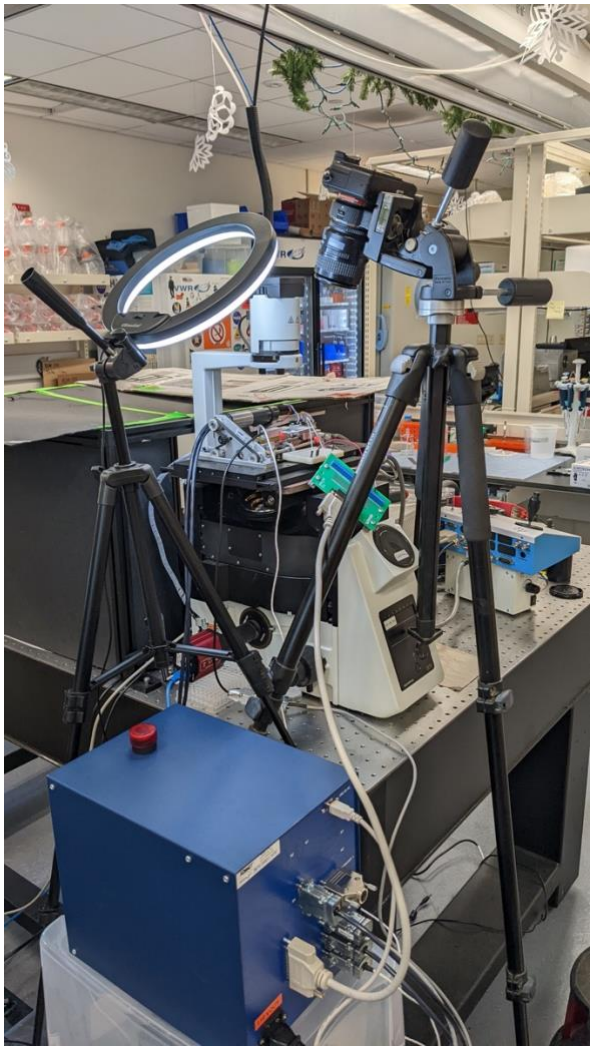

Figure A.17: Overview of the camera setup, including the external trigger, ring light, and tripod.

Setting Up a New Test

1. Extract the saline from the fluid bath using the vacuum trap.
2. Remove the specimen and place in Falcon tube with saline. Remember to take photos for reference.
3. Clean vise grips and fluid bath with DI water and remove any remaining debris. Clean optical viewport with a Kimwipe.
4. Follow the “Reset” protocol to adjust the grip separation to “home” (i.e., grip separation = 31 mm) using the MTESTQuattro software and confirm the grip separation is 31 mm

using the metric ruler. Use this value as the value for grip separation in the “Report Setup” tab.

5. Secure next specimen to be tested in the vice grips and fill the fluid bath with saline using a plastic pipette.
6. Repeat the entire protocol until all specimens have been tested and all data has been saved to the appropriate locations in Box.

At the end of the test day:

1. Place all the tested specimens in their respective Falcon tubes (clearly labelled) and store in the freezer.
2. If planning to test the next day, ensure the appropriate number of specimens are defrosting in the refrigerator.
3. If not planning to test the next day, take down all the mechanical test equipment. Reverse the set-up process for the Raman equipment and reset the ANDOR Solis acquisition settings.

Data to be collected during this set of experiments:

- Mechanical test data including load (if possible) and displacement.
- Raman spectral data and band shifts.
- Video recording of stress-whitening.

Data Processing Plan

Video Data

- Video data will be analyzed for stress-whitening. Whitening will be quantified following a manual segmentation method using a custom macro in ImageJ. For more detailed analysis protocol, see Appendix A7.
- Linear Mixed Models will be performed on the whitening measurements from before and after mechanical testing.

Raman Data Analysis

1. Principal component analysis (PCA) will be performed on the Raman spectral data.
    a. PCA will be run over all kinetic series collected from each bone for the "Sitting in Solution Test" data
    b. PCA will be run over all kinetic series collected from each bone for the "Mechanical Test" data
    c. PCA will be run over all kinetic series collected from each bone from both the "Sitting in Solution Test" and "Mechanical Test".
    d. From each PCA, PC scores and loadings for the PCs accounting for ~90% of the variance will be extracted for each spectral recording.
2. Average Raman Intensity and Difference in Average Raman Intensity will be determined using data from all bones, as follows:
    a. Average Raman spectra (Intensity v. Wavenumber) from the "Unloaded" condition, the "Loaded" condition, and the "Sitting in Solution" condition. *Sarah wrote a MATLAB program to do this from a saved data stack.
        i. Extract all kinetic series from the relevant condition

ii. Determine average Intensity at each wavenumber in range (400, 3800)

iii. Determine standard deviation of Intensity at each wavenumber in range (400, 3800)

b. The Difference in Average Raman intensity will also be determined for as:

dI = Average Intensity Loaded – Average Intensity Unloaded

3. Univariate linear mixed models will be performed on the extracted PC scores for the "Sitting in Solution Test" data and the "Mechanical Test" data, respectively.

   a. Likely, we will run the Univariate analysis on PC1, PC2, and PC3 – but will include PCs depending on the percent of variance accounted for.

   b. The results from the linear mixed model on the "Sitting in Solution Test" data will indicate if there is any effect of sitting in solution on the Raman signature (t = 0, 20, 40, and 60 min).

   c. The results from the linear mixed model NOVA on the "Mechanical Test" data will indicate if there is any effect of loading on the Raman signature (loaded and unloaded).

   d. The linear mixed model results from the PCA with both data sources (Sitting in Solution & Mechanical Test) will indicate if there are any significant differences between sitting in solution and mechanically testing the specimen.

4. If the univariate linear mixed models show significant difference in PCn score of "Unloaded" and "Loaded":

   a. Visually determine how the PCn score splits the two conditions (i.e., PCn >0, <0, …). *Alternatively, we can perform a classification tree to determine the best split

b. Compare the PCn Loading (intensity values) to the PCn score separation to determine which Raman shift bands (wavenumbers) are different between the two conditions

c. Use literature references to determine what the specific shift bands are identified as → this should indicate increases or decreases in the amount of substance xxx in the specimen

d. To check results, use the dI values calculated in Step 2b

5. OH-band shifts will be quantified for each mechanical test by measuring the difference between the intensities of the OH-peak before and after mechanical testing.
    a. LDA could also be performed?
6. If there are any other peaks whose intensities are significantly affected by mechanical testing (e.g., Amide 1 and CH-stretch), then the band shifts will be quantified by measuring the difference in the intensities before and after mechanical testing.

Mechanical Data

If load data **was** reliable:

- Load and displacement data will be used to calculate the stress and strain.
- The following plots will be created:
    - Stress v. strain v. OH-band shifts*.
    - Shift in OH-band position* v. stress
    - Shift in OH-band position* v. strain
    - Stress v. strain v. whitening
    - Strain v. whitening
    - Mean PC1 score v. whitening

If load data **was not** reliable:

- Displacement data will be used to calculate the strain.
- The following plots will be created:
    - Shift in OH-band position* v. strain
    - Strain v. whitening
    - Mean PC1 score v. whitening

*This will also include the band shifts for any other peak which shows significant shifts as an effect of mechanical testing.

Specimen Information

Preliminary data was collected of the Raman signature before and after performing the Strain-to-Whiten protocol. A univariate ANOVA was performed on the scores of the first principal components from this data. Based on the PC1 scores, **a minimum of 8 bone beams specimens** was needed to detect differences in mean PC1 scores and mean whitening values before and after loading to whitening.

The bone beam specimens that will be used in this experiment originate from a thoroughbred racehorse. The proximal medial section of the left MC3 bone was used to manufacture a total of 20 bone beams. From this set, 8 will be used for the experiments. The specimens originated from the second row of beams (9.2 Red, Navy, Green, and Black) and from the third row of beams (9.3 Red, Navy, Green, and Black) in the proximal medial section of bone.

A9: Summary of Troubleshooting and Tips

1. General difficulties with the equipment
    a. Setting up the device and learning how to use the temperature controller (not included in the initial training)
        i. Installing drivers
        ii. Learning the software and setting up serial connection
        iii. Setting the temperature setpoint
    b. Getting approval from UC Davis School of Veterinary Medicine (SVM) IT to set up the computer in the building (i.e., risk assessment questionnaire)
    c. Setting up temperature controller (ADMET failed to send the required cable initially)
        i. Tried replacing it with other cables from the lab; turned out it had to be a specific cable they provided, not a standard cable
    d. Position limit/overrange error (protocol issue)
        i. Manually set the grip separation; cannot go to limits
        ii. Fragile wiring (open to air) broke and needed to be re-soldered
    e. Device suddenly stopped calculating strain (electrical issue)
        i. Went through each electrical connection (unscrewed everything and put it back together)
2. Collecting good quality mechanical data during position-controlled tests
    a. Issues with strain creep and incorrect calculation
        i. Tried adding tension in the form of rubber bands
    b. Temperature controller not holding setpoint well

i. Autotuned the temperature controller

ii. Tuned PI values manually

c. Load and strain wiggling/generally being incorrect – electrical interference from fluid bath heaters

i. Tried moving the system to various places in the lab

ii. Tried grounding the temperature controller to the frame

iii. Tried applying Kapton tape to the fluid bath heaters

General tips and tricks:

- Use a quartz coverslip (not glass) when collecting Raman data. The glass will cause autofluorescence in the Raman data in the same range as the amide III, CH_2 and amide I peaks, covering the peak of interest.
- Store deuterium oxide in a desiccator, as it is hygroscopic.
- Store used demineralization solution in a plastic bottle and give to Tanya for disposal.
- Allow temperature controller about 1 hour to heat up to the setpoint before collecting data.
- Check laser power before each instance of Raman measurements because the laser power has been fluctuating greatly.

References

[1] Y. N. Yeni, M. B. Schaffler, G. Gibson, and D. P. Fyhrie, “Prestress due to dimensional changes caused by demineralization: A potential mechanism for microcracking in bone,” *Annals of Biomedical Engineering*, vol. 30, no. 2, pp. 217–225, 2002, doi: 10.1114/1.1451078.

[2] D. Berry *et al.*, “Tracking heavy water (D2O) incorporation for identifying and sorting active microbial cells,” *Proceedings of the National Academy of Sciences of the United States of America*, vol. 112, no. 2, pp. E194–E203, Jan. 2015, doi: 10.1073/pnas.1420406112.

[3] G. R. Masson *et al.*, “Recommendations for performing, interpreting and reporting hydrogen deuterium exchange mass spectrometry (HDX-MS) experiments,” *Nature Methods*, vol. 16, no. 7, pp. 595–602, Jul. 2019, doi: 10.1038/s41592-019-0459-y.

[4] M. Jastrzebska, R. Wrzalik, A. Kocot, J. Zalewska-Rejdak, and B. Cwalina, “Hydration of glutaraldehyde-fixed pericardium tissue: Raman spectroscopic study,” *Journal of Raman Spectroscopy*, vol. 34, no. 6, pp. 424–431, Jun. 2003, doi: 10.1002/jrs.1016.

[5] M. R. Hardisty, T. C. Garcia, S. Choy, J. Dahmubed, S. M. Stover, and D. P. Fyhrie, “Stress-whitening occurs in demineralized bone,” *Bone*, vol. 57, no. 2, pp. 367–374, Dec. 2013, doi: 10.1016/j.bone.2013.08.029.